

DISSERTATION

Connecting Endothelial Behavior and Hemodynamics –
Method Development for Preclinical Optical Imaging of the
Vasculature
Verknüpfung von Endothelverhalten und Hämodynamik –
Methodenentwicklung für die präklinische optische
Bildgebung des Blutgefäßsystems

zur Erlangung des akademischen Grades
Doctor of Philosophy (PhD)

vorgelegt der Medizinischen Fakultät
Charité – Universitätsmedizin Berlin

von
Elisabeth Baumann

Erstbetreuung: Prof. Dr. Holger Gerhardt

Datum der Promotion: 29. November 2024

Vorwort

Teilergebnisse der vorliegenden Arbeit wurden veröffentlicht in:

Elisabeth Baumann, Ulrike Pohle, Edward Zhang, Thomas Allen, Claus Villringer, Silvio Pulwer, Holger Gerhardt and Jan Laufer. A backward-mode optical-resolution photoacoustic microscope for 3D imaging using a planar Fabry-Pérot sensor. *Photoacoustics*, 24:100293, 2021.

Yi Jin, Yindi Ding, Mark Richards, Mika Kaakinen, Wolfgang Giese, **Elisabeth Baumann**, Anna Szymborska, André Rosa, Sofia Nordling, Lilian Schimmel, Emir Bora Akmeriç, Andreia Pena, Emmanuel Nwadozi, Maria Jamalpour, Katrin Holstein, Miguel Sáinz-Jaspeado, Miguel O. Bernabeu, Michael Welsh, Emma Gordon, Claudio A. Franco, Dietmar Vestweber, Lauri Eklund, Holger Gerhardt and Lena Claesson-Welsh. Tyrosine-protein kinase Yes controls endothelial junctional plasticity and barrier integrity by regulating VE-cadherin phosphorylation and endocytosis. *Nature Cardiovascular Research*, 1:1156–1173, 2022.

Abstract

To fulfill its function of supplying the body with oxygen and nutrients, the healthy vasculature adopts a highly hierarchical network structure. Endothelial cells (ECs), which line the inner walls of blood vessels, are the primary drivers of vascular network patterning. They seem to sense the forces of the blood, i.e. hemodynamics, and respond dynamically to blood flow or oxygenation. Although this dynamic behavior is disrupted in many vascular diseases, many questions remain about the pathways and sensing mechanisms involved. High-resolution microscopy is an excellent tool for deciphering these processes. However, novel imaging and image analysis methods are needed to extract valuable quantitative information about the connection between hemodynamics and endothelial dynamics.

In this thesis, I seek to fill this gap by developing quantitative methods to study two well-established *in vivo* model systems of vascular remodeling, the zebrafish and the developing mouse retina. In my first project, I established an optical-resolution photoacoustic microscopy (OR-PAM) system based on a planar Fabry-Pérot ultrasound sensor for quantitative imaging of hemodynamics in zebrafish. OR-PAM is particularly well suited for imaging the vasculature due to its intrinsic hemoglobin contrast. I show that the developed OR-PAM system meets the requirements for functional imaging of blood flow and oxygenation in the zebrafish trunk vasculature. It features high spatial resolution below 10 μm , backward-mode operation, high acoustic sensitivity, broadband ultrasound detection, a fast image acquisition mode to resolve blood flow, and dual-wavelength excitation to enable spectroscopic imaging of blood oxygenation. Importantly, the OR-PAM system developed in this work can be integrated with other microscopy techniques for simultaneous observation of hemodynamics and endothelial dynamics. I demonstrate its imaging capabilities in leaf skeleton and blood vessel phantoms as well as *in vivo* in zebrafish.

In a second project, I developed a computational image analysis method to extract

information about endothelial dynamics from static images of the developing mouse retina based on a lineage tracing approach. By labeling a subset of ECs at a given time point and analyzing the spatial distribution of ECs with respect to a vascular reference system at several later time points, I was able to infer endothelial dynamics. The method shows a shift of ECs from veins to arteries and towards the retinal periphery over time, suggesting directed EC migration. I was also able to quantify migration defects caused by knockout of *Cdc42* and *Rac1*, and showed that *Cdc42* is essential for EC migration against flow.

Taken together, my transdisciplinary work comprises a significant contribution to the toolbox of methods to study the mechanisms of endothelial dynamics with the goal of identifying the pathomechanisms of vascular disease and developing targeted treatment strategies.

Zusammenfassung

Ein gesundes Gefäßsystem weist eine hochgradig hierarchische Struktur auf, um den Körper mit Sauerstoff und Nährstoffen zu versorgen. Endothelzellen (ECs), die die Innenwände von Blutgefäßen auskleiden, sind die treibende Kraft hinter dieser Strukturierung. Sie scheinen die Kräfte des Blutes, d.h. die Hämodynamik, wahrzunehmen und reagieren dynamisch auf z.B. den Blutfluss und den Sauerstoffgehalt. Obwohl dieses dynamische Verhalten bei vielen Gefäßerkrankungen gestört ist, sind noch viele Fragen über die beteiligten Signalwege und Mechanismen offen. Hochauflösende Mikroskopie ist ein hervorragendes Instrument, um diese Prozesse zu entschlüsseln. Es sind jedoch neue Bildgebungs- und Bildanalysemethoden erforderlich, um quantitative Informationen über die Verbindung zwischen Hämodynamik und Endotheldynamik zu erhalten. In dieser Arbeit habe ich quantitative Methoden entwickelt, um dies in zwei *in vivo* Modellsystemen für das vaskuläre Remodelling zu erreichen. In meinem ersten Projekt habe ich ein optisch-auflösendes photoakustisches Mikroskop (OR-PAM) basierend auf einem planaren Fabry-Pérot-Ultraschallsensor entwickelt, um die Hämodynamik in Zebrafischen darzustellen. Ich zeige, dass das OR-PAM-System die Anforderungen der funktionellen Bildgebung des Blutflusses und der Sauerstoffsättigung im Rumpfgefäßsystem des Zebrafisches erfüllt. Es bietet eine hohe räumliche Auflösung von weniger als 10 μm , hohe akustische Empfindlichkeit, Breitband-Ultraschalldetektion, einen schnellen Bildaufnahmemodus zur Auflösung des Blutflusses und eine Zwei-Wellenlängen-Anregung für die spektroskopische Darstellung der Blutsauerstoffsättigung. Darüber hinaus kann das entwickelte OR-PAM-System mit anderen Mikroskopietechniken kombiniert werden, um gleichzeitig die Hämodynamik und die Endotheldynamik zu beobachten. Ich demonstriere die Bildgebung in Blattskelett- und Blutgefäßphantomen sowie *in vivo* im Zebrafisch.

In einem zweiten Projekt habe ich eine computergestützte Bildanalysemethode entwickelt, um Informationen über die Endotheldynamik aus statischen Bildern der Mausretina zu extrahieren. Durch die Markierung einer Subpopulation von ECs zu einem

bestimmten Zeitpunkt und die Analyse der räumlichen Verteilung der ECs relativ zu einem vaskulären Referenzsystem zu späteren Zeitpunkten konnte ich Rückschlüsse auf die Endotheldynamik ziehen. Die Methode zeigt, dass sich die ECs im Laufe der Zeit von Venen zu Arterien und in die retinale Peripherie bewegen, was auf eine gerichtete Migration der ECs hindeutet. Ich war auch in der Lage, Migrationsdefekte zu quantifizieren, die durch das Ausschalten von Cdc42 und Rac1 verursacht wurden, und konnte zeigen, dass Cdc42 für die EC-Migration gegen den Blutfluss essentiell ist.

Insgesamt stellt meine Arbeit einen wichtigen Beitrag zum Methodenspektrum zur Untersuchung der Mechanismen der Endotheldynamik dar, mit dem Ziel Pathomechanismen von Gefäßerkrankungen zu identifizieren und gezielte Behandlungsstrategien zu entwickeln.

Contents

Vorwort	i
Abstract	iii
Zusammenfassung	v
List of Figures	xi
List of Tables	xiii
Abbreviations	xv
I Biological motivation and objectives	1
1 Fundamentals of vascular biology and endothelial dynamics	3
1.1 Structure and function of the vascular system	3
1.2 Development of the vascular system	6
1.2.1 Molecular and cellular mechanism of sprouting angiogenesis . . .	6
1.2.2 Cellular mechanism of anastomosis	8
1.2.3 Role of endothelial cells and flow for vascular remodeling	9
1.3 Role of endothelial cells in vascular disease	10
1.4 Concluding remarks	11
2 Model systems for preclinical optical imaging of endothelial dynamics	13
2.1 The zebrafish as model system for live <i>in vivo</i> imaging of vascular devel- opment and disease	13
2.2 The developing mouse retina as model system for static <i>ex vivo</i> imaging of vascular development and disease	15

3	Objectives and structure of thesis	19
II	Photoacoustic microscopy for <i>in vivo</i> functional imaging of the zebrafish trunk vasculature	23
4	Introduction and Theory	27
4.1	Fundamentals of photoacoustic imaging	27
4.2	Modalities of photoacoustic imaging	30
4.3	Comparison of OR-PAM and other biomedical imaging techniques	32
4.3.1	OR-PAM in comparison to optical microscopy techniques	32
4.3.2	Imaging of blood oxygen saturation	33
4.3.3	Imaging of blood flow	34
4.4	OR-PAM of the vasculature	35
4.4.1	Quantitative imaging of blood oxygen saturation using OR-PAM	37
4.4.2	Quantitative imaging of blood flow using OR-PAM	40
4.5	Ultrasound detection in OR-PAM	42
4.5.1	Important characteristics of ultrasound transducers for OR-PAM	42
4.5.2	Different types of ultrasound transducers	43
4.5.3	The planar Fabry-Perót interferometer as ultrasound sensor for OR-PAM	45
4.6	System requirements	46
5	Methods	49
5.1	Optical and technical setup of the Optical-Resolution Photoacoustic Microscope	49
5.1.1	Laser systems for multi-wavelength excitation of photoacoustic signals	49
5.1.2	Planar Fabry-Pérot ultrasound sensors	51
5.1.3	Photoacoustic signal excitation and acquisition	52
5.2	Scanning modes	53
5.2.1	Principle of the raster-scanning mode	53
5.2.2	Principle of the continuous-scanning mode	54
5.3	Control and image reconstruction software	55
5.3.1	Software for raster-scanning mode	55
5.3.2	Software for continuous-scanning mode	55
5.4	Experimental work	57

5.4.1	Fabry-Pérot sensor characterization	57
5.4.2	Image acquisitions	58
6	Results and Discussion	61
6.1	System characterization	61
6.1.1	Characterization of the Fabry-Pérot sensor	62
6.1.2	Spatial resolution	64
6.2	<i>In vitro</i> raster-scanning OR-PAM of phantoms	67
6.2.1	Morphological OR-PAM	67
6.2.2	Multi-wavelength OR-PAM	67
6.2.3	Continuous-scanning OR-PAM	71
6.3	<i>In vivo</i> OR-PAM of zebrafish	74
7	Conclusions and Outlook	77
III	Computational image analysis method to study endothelial dy-	
	namics and its defects in the developing mouse retina	81
8	Introduction	85
9	Methods	89
9.1	Mouse work	89
9.2	Computational method to extract the spatial distribution of ECs from microscopy images of the developing mouse retina	91
9.3	Data preparation and software	96
10	Results and Discussion	97
10.1	2D distribution analysis shows EC distribution shift from veins to ar- teries in the developing mouse retina	97
10.2	2D Distribution analysis reveals roles of Cdc42 and Rac1 for endothelial migration	102
10.2.1	Cdc42 plays an essential role for endothelial migration under flow	102
10.2.2	Rac1-depleted cells show minor migration defects	104
11	Conclusions and Outlook	107

CONTENTS

IV Summary	109
A Additional data for part II	113
A.1 OR-PAM with an FP sensor with a 5 μm spacer	113
A.2 Development of a Raman laser for OR-PAM	114
B Additional data for part III	115
B.1 Radial distribution shift of ECs is barely affected by knockout of Cdc42 and Rac1	115
References	117
Eidesstattliche Versicherung	145
Anteilerklärung an erfolgten Publikationen	147
List of Publications	149
Acknowledgements	151
Curriculum Vitae	155
Statistics Certificate	159

List of Figures

1.1	Structure of the vascular system of vertebrates.	4
1.2	Structure and function of different blood vessel types.	5
1.3	Schematic of sprouting angiogenesis and vascular remodeling.	7
2.1	Overview of the zebrafish vasculature.	14
2.2	Primary plexus vasculature of the developing mouse retina.	16
4.1	Schematic overview of photoacoustic imaging of the vasculature	28
4.2	Different modalities of photoacoustic imaging.	30
4.3	Optical absorption of hemoglobin.	38
4.4	Example Interferometer Transfer Function	46
5.1	Experimental setup of the backward-mode OR-PAM system using a planar Fabry-Pérot (FP) ultrasound sensor.	50
5.2	Alternative excitation laser system based on a fiber-based Raman laser.	51
5.3	Working principle of the FP sensor.	52
5.4	Data acquisition and processing workflows of the continuous-scanning mode	56
6.1	Characterization of the planar Fabry-Pérot ultrasound sensor.	62
6.2	Measurements of the lateral resolution of the system.	65
6.3	OR-PAM image of a leaf skeleton phantom acquired in raster-scanning mode.	67
6.4	Comparison of OR-PAM images of a leaf skeleton phantom obtained at different excitation wavelengths in raster-scanning mode.	68
6.5	OR-PAM images of ink phantoms simulating blood acquired at five different excitation wavelengths in raster-scanning mode.	69

LIST OF FIGURES

6.6	OR-PAM image of a leaf skeleton phantom obtained in continuous-scanning mode.	71
6.7	<i>In vivo</i> OR-PAM image of a zebrafish embryo (4 dpf) acquired in raster-scanning mode.	74
9.1	Mouse work for the EC distribution analysis.	90
9.2	Distance maps of the retina based on manual annotations of the vessel anatomy.	93
9.3	Distance maps of the retina that were created to normalize for retina size.	94
9.4	Visualization of the EC distributions.	95
10.1	2D distribution analysis of stochastically labeled ECs shows a population shift from veins to arteries over time.	98
10.2	2D distribution analysis of Cdc42-depleted ECs unravels major migration defects.	103
10.3	2D distribution analysis of Rac1-depleted ECs unravels minor migration defects.	105
10.4	Boxplots of the mean V-A distribution of individual retinas.	106
A.1	OR-PAM image of a leaf skeleton phantom obtained with an FP sensor with a 5 μm spacer.	113
A.2	Spectrum of a Raman laser for OR-PAM excitation.	114
B.1	Radial distribution shift of ECs is unaffected by knockout of Cdc42 and slightly affected by knockout of Rac1.	115

List of Tables

5.1	Input parameters for modeling of the acoustic frequency response of the FP sensor.	57
-----	--	----

Abbreviations

aISV	Arterial intersegmental vessel
Ang-1	Angiopoietin 1
Ang-2	Angiopoietin 2
AOM	Acousto-optic modulator
AOTF	Acousto-optic tunable filter
AR-PAM	Acoustic-resolution photoacoustic microscopy
AVM	Arteriovenous malformation
bFGF	Basic fibroblast growth factor
BOLD	Blood oxygen level dependent
Cdc42	Cell division control protein 42 homolog
COP	Cyclo olefin polymer
CT	Computed tomography
cw	Continuous wave
DA	Dorsal aorta
DCS	Diffuse correlation spectroscopy
DLAV	Dorsal longitudinal anastomotic vessel
Dll4	Delta-like ligand 4
DNA	Deoxyribonucleic acid
DOI	Diffuse optical imaging
dpf	Days post fertilization
EC	Endothelial cell
ERG	ETS-related gene
ESF	Edge-spread function
ETS	Erythroblast transformation-specific
fps	Frames per second
FTL	Focus tunable lens
GTP	Guanosine triphosphate

0. ABBREVIATIONS

Hb	Hemoglobin
HbCO	Carboxyhemoglobin
HbCO ₂	Carbaminohemoglobin
HbMet	Methemoglobin
HbO ₂	Oxygenated hemoglobin
HbR	Deoxygenated hemoglobin
HbSulf	Sulfhemoglobin
HHT	Hereditary haemorrhagic telangiectasia
HIF	Hypoxia-induced factor
HIF α	α -subunit of HIF
HIF β	β -subunit of HIF
IB4	Isolectin B4
iECKO	inducible, endothelial cell specific knockout
ISV	Intersegmental vessel
ITF	Interferometer transfer function
fMRI	Functional magnetic resonance imaging
FOV	Field of view
FP	Fabry-Pérot
FSR	Free spectral range
FWHM	Full-width at half-maximum
GFP	Green fluorescent protein
KO	Knockout
LDF	Laser Doppler flowmetry
LSCI	Laser speckle contrast imaging
LSF	Line-spread function
MIP	Maximum intensity projection
MFD	Mode field diameter
MP	Multi-photon
MPM	Multi-photon microscopy
MRI	Magnetic resonance imaging
NEP	Noise-equivalent pressure
NI	National Instruments
NIR	Near-infrared
OCT	Optical coherence tomography
OIR	Oxygen-induced retinopathy
OR-PAM	Optical-resolution photoacoustic microscopy

P7 Postnatal day 7
PA Photoacoustic
PAI Photoacoustic imaging
PAM Photoacoustic microscopy
PAT Photoacoustic tomography
PBS Polarizing beamsplitter
PCV Posterior cardinal vein
PDGF Platelet-derived growth factor
PPN Peak-to-peak noise
PRR Pulse repetition rate
PSF Point spread function
PTU 1-phenyl 2-thiourea
Rac1 Ras-related C3 botulinum toxin substrate 1
RBC Red blood cell
Rho GTPase Ras homologue GTPase
RNA Ribonucleic acid
ROI Region of interest
ROP Retinopathy of prematurity
SNR Signal-to-noise ratio
TDMS Technical data management streaming
THV Tetrafluoroethylene hexafluoropropylene and vinylidene fluoride
US Ultrasound
USAF United States Air Force
UV Ultraviolet
V-A Vein-to-artery
VEGFR Vascular endothelial growth factor receptor
VEGFR3 Vascular endothelial growth factor receptor 3
vISV Venous intersegmental vessel
vSMC Vascular smooth muscle cell
WSS Wall shear stress

PART I

Biological motivation and
objectives

Fundamentals of vascular biology and endothelial dynamics

1.1 Structure and function of the vascular system

The vascular system of vertebrates is a fascinating structure that assumes a number of vital functions. These include supplying every organ and tissue with oxygen and nutrients (i.e. with the necessary energy for metabolic processes), circulating immune factors and hormones, and regulating blood pressure and body temperature.

In order to achieve these tasks, a healthy vascular system adopts a highly hierarchical structure (figure 1.1) [1]. It consists of the heart (the blood pumping engine) and blood vessels (the network of blood-carrying tubes spanning the entire body). There are roughly five types of vessels that vary greatly in diameter: arteries, arterioles, capillaries, venules and veins. In mammals, oxygen-rich blood is circulated from the heart through arteries to arterioles (the distributing vessels) which feed into fine capillaries. In the capillary beds, which are connected in parallel circuits supplying all tissues, oxygen and nutrients are taken up from the blood by the surrounding cells while carbon dioxide and metabolic waste products are passed back to it. The capillaries feed into venules that in turn feed into veins (the collecting vessels) which transport the oxygen-depleted blood back to the heart. In a second, independent blood vessel loop, the oxygen-depleted blood is pumped from the heart through the pulmonary artery to the lungs, where gas exchange of carbon dioxide and oxygen occurs. The newly oxygen-enriched blood flows back through the pulmonary vein to the heart from where it can be redistributed through the body. By coordinated valve opening during the

blood pumping process, the heart ensures that the blood always circulates in the right direction.

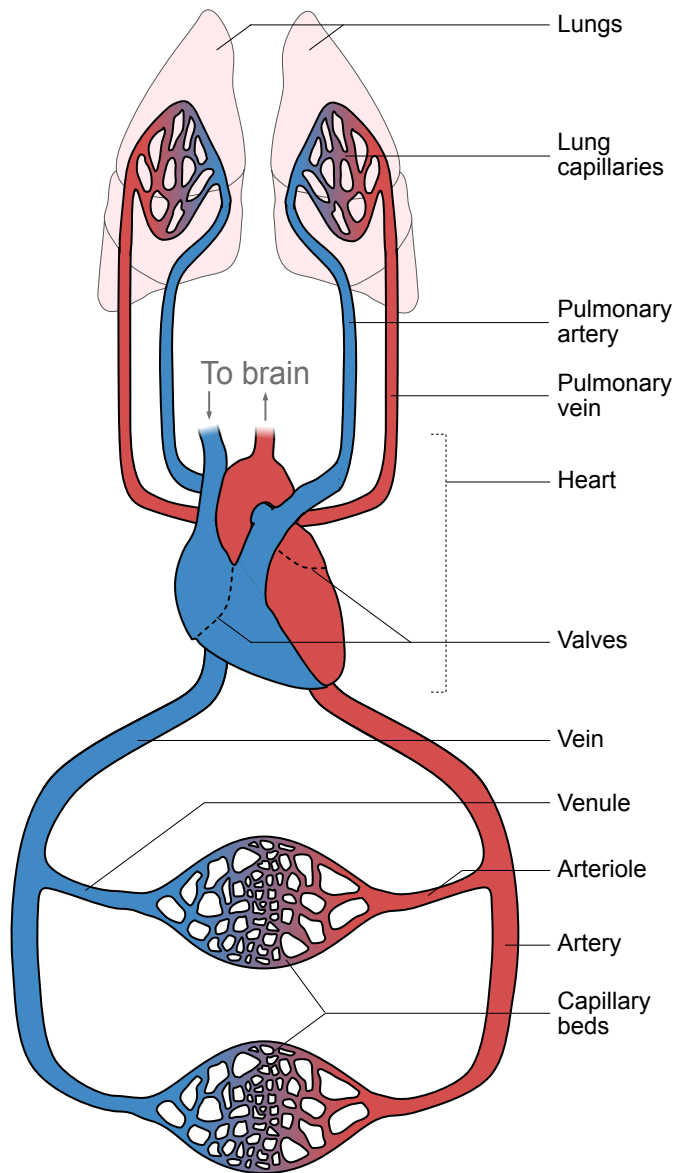


Figure 1.1: The vascular system of vertebrates. Oxygen-rich blood is pumped from the heart through arteries and arterioles to capillary beds in all organs and tissues, where oxygen and nutrients are taken up by surrounding cells. The oxygen-depleted blood is transported through venules and veins back to the heart and from there through the pulmonary artery to the lungs. In the lungs, gas exchange of carbon dioxide and oxygen occurs. The oxygen-enriched blood flows from the lungs through the pulmonary vein to the heart and can be redistributed through the body. Coordinated valve opening of the heart ensures that the blood always flows in the right direction.

While all vessel types consist of the same cell types, they exhibit different structures to accommodate for their respective function (figure 1.2). All vessel types feature an innermost layer called the endothelium that is in direct contact with the blood. These endothelial cells (ECs) are surrounded by a basement membrane. Arteries and veins are in addition covered by a stabilizing layer of vascular smooth muscle cells (vSMC) and connective tissue [2]. The ability of the vSMCs to contract and expand allows both arteries and veins to change their diameter to regulate the blood flow between tissues. However, as arteries are exposed to high blood pressures, they have a much thicker layer of vSMCs than veins, which exhibit a lower hemodynamic load. Capillaries lack the layers of connective tissue and vSMCs altogether as they need to maintain permeability for exchange of oxygen and metabolites with the surrounding tissue as well as adaptability for expansion of the vascular network following environmental cues. Therefore, they only consist of a single layer of ECs that is supported by a basement membrane and a sparse layer of pericytes.

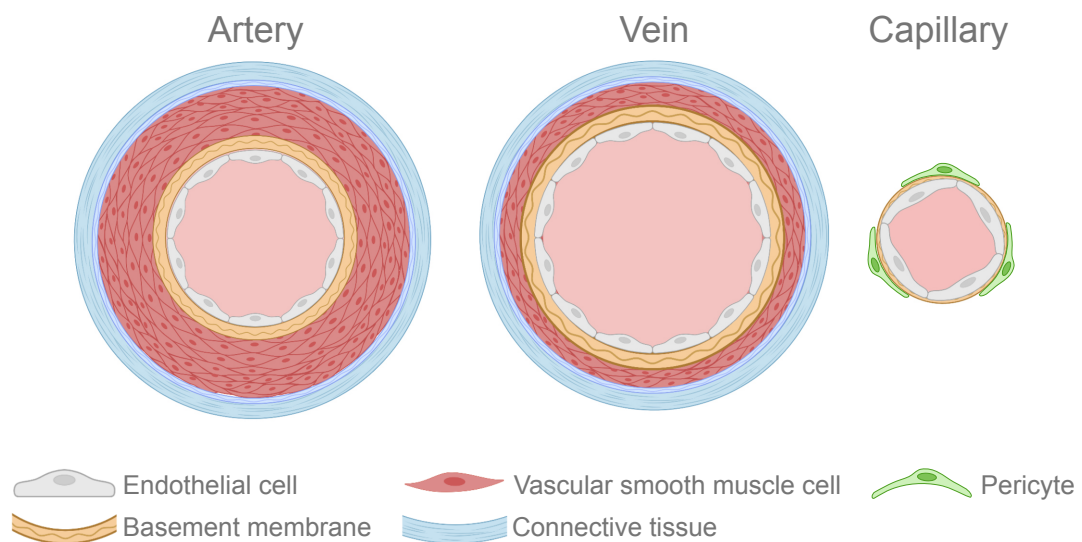


Figure 1.2: Structure and function of different blood vessel types. All blood vessels feature an innermost layer of endothelial cells that is surrounded by a basement membrane. Arteries are in addition covered by a thick layer of vascular smooth muscle cells (vSMCs) and connective tissue to cope with the high hemodynamic load. Veins are covered by thinner layers of vSMCs and connective tissue. In contrast, capillaries are only stabilized by a sparse layer of pericytes to maintain permeability and adaptability of the vasculature. Created with [BioRender.com](https://www.biorender.com).

This functional and morphological heterogeneity cannot only be observed on the

blood vessel level but also on the cellular level. ECs, in particular, can assume different shapes and functions depending on the vessel part, organ, or developmental state of the vasculature they are part of [3]. Being the primary driver of the adaptability of the vasculature, they are also the cells that facilitate vascular growth and remodeling. During adulthood, ECs remain mostly quiescent but they are quickly activated in response to signaling factors calling for adjustment of the blood vessel network, for example, following physical exercise, injury or during the menstrual cycle.

1.2 Development of the vascular system

Because of its crucial function for organism survival, the vasculature is one of the first organs to form during embryonic development [4]. Initially, *de novo* vessel formation is facilitated by the assembly of endothelial progenitors called angioblasts into tubes. This process is called vasculogenesis [5]. Once a primitive vessel network has been established, new vessels form from existing vessels in a process called angiogenesis. Angiogenesis can occur in two different ways. Less commonly, vessels split along their longitudinal axis such that two separate vessels form (intussusceptive angiogenesis) [6, 7]. The majority of vessel growth, however, occurs via the sprouting of new vessel branches from a parent vessel (sprouting angiogenesis) [5]. As many vascular diseases are characterized by disrupted sprouting angiogenesis, understanding this process in detail has gained much research interest in recent years [3, 5, 8].

1.2.1 Molecular and cellular mechanism of sprouting angiogenesis

Sprouting angiogenesis is a highly stereotypical and orchestrated process that requires coordinated actions of a variety of cells, of which ECs are arguably the most important [5]. In a first step, new vessel growth is initiated by signaling cues from poorly oxygenated tissue. This hypoxic state can arise either due to a higher demand of oxygen (e.g. following physical exercise) or a too low oxygen supply [9]. The molecular response of cells in hypoxic tissues is mediated by intracellular hypoxia-inducible factors (HIFs). HIFs are highly conserved transcription factors that are involved in the regulation of many cellular processes [9, 10]. They exist in the form of an α - and a β -subunit (HIF α and HIF β , respectively). HIF α is ubiquitously expressed at low levels but rapidly degraded in an oxygen-dependent process. The absence of oxygen during hypoxia allows HIF α to accumulate and translocate to the nucleus. In the nucleus, it binds to the ubiquitously-expressed HIF β and together the HIF α/β complex drives

the transcription of a variety of genes, including important pro-angiogenic factors such as vascular endothelial growth factor (VEGF), angiopoietin 1 (Ang-1), angiopoietin 2 (Ang-2), basic fibroblast growth factor (bFGF) and platelet-derived growth factor (PDGF) [9]. As these factors are secreted, they diffuse through the extracellular matrix such that a concentration gradient of growth signals, first and foremost VEGF, is achieved from a high concentration in close proximity to the hypoxic tissue to lower concentrations further away from it (figure 1.3) [11]. As the signaling cues reach the surface of a capillary, endothelial cells respond by initiating sprouting angiogenesis. Following the binding of VEGF and Ang-2, pericytes detach and the endothelial basement membrane disintegrates [12]. This process allows for the growth of vascular sprouts following the gradient of pro-angiogenic factors, ultimately leading to the vascularization of the hypoxic tissue.

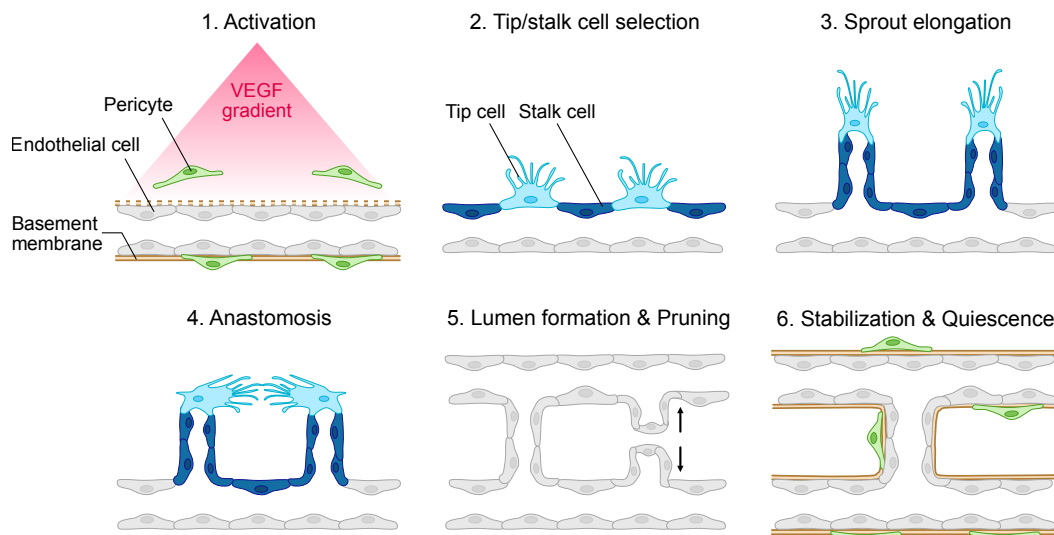


Figure 1.3: Overview of sprouting angiogenesis and vascular remodeling. Upon activation of a blood vessel following binding of pro-angiogenic factors, pericytes detach and the basement membrane disintegrates. Tip and stalk cells are selected through VEGF and Notch signaling. Coordinated elongation of several sprouts is achieved through tip cell migration and stalk cell proliferation. Two tip cells fuse to form a new vascular connection in a process called anastomosis. The new vascular connection is perfused. Vessel branch maturation and pruning are mediated by blood flow. After remodeling, endothelial cells enter quiescence, pericytes are recruited and the basement membrane is reestablished. Adapted from [5] and [11].

The growth of the vascular sprout requires a collective effort of numerous endothelial cells. Phenotypically, they can be distinguished into tip cells and stalk cells. Tip

cells with their numerous filopodia exhibit an exploratory and migratory behavior. In contrast, stalk cells have fewer membrane protrusions and are highly prolific [5]. The division of ECs into tip cells and stalk cells led to the hypothesis that a single tip cell guides the growth of the sprout while the stalk cells follow and stabilize it [13]. However, later research showed that, in fact, ECs compete for the tip cell position and frequently change their phenotype during sprouting [14, 15].

Along the growth-signal activated blood vessel, most ECs will adopt a stalk cell identity and only some ECs a tip cell identity. Tip cell selection is a complex process that is mainly determined by Notch and VEGF signaling [16]. Binding of VEGF promotes a tip cell phenotype by activating several tip-cell-specific signaling pathways regulating cell proliferation and migration [17]. In addition, VEGF also activates the expression of Delta-like ligand 4 (Dll4). Dll4 activates Notch signaling in neighboring cells by binding to their extracellular Notch1 domain. Besides promoting a stalk cell phenotype, Notch suppresses the expression of VEGF receptors (VEGFR) and Dll4 [18, 19]. Hence, these cells are less likely to bind VEGF and also less likely to inhibit the tip cell phenotype in their neighbors. Through this negative feedback loop, initially small differences in VEGF signaling between individual ECs are converted to big differences in Notch signaling such that only scattered ECs adopt a tip cell phenotype. This phenomenon is known as lateral inhibition and ensures the regulated growth of several vascular sprouts, by means of collective EC migration and proliferation, from the activated vessel towards the signaling cues originating from hypoxic tissue [5, 19].

1.2.2 Cellular mechanism of anastomosis

When two vascular sprouts meet or a vascular sprout meets an existing vessel, they can fuse to build a new vascular connection in a process called anastomosis [20]. Anastomosis is initiated by the contact of the filopodia of two tip cells (figure 1.3). Initially, they touch in one spot only but the contact region quickly elongates and expands forming a new cell-cell junction. A lumen forms between the cells of the new junction which is eventually fused with the lumen expanding from either original vascular sprout. As a result, a vascular tube forms that is connected to the main vessel network.

This immature vascular tube rapidly matures to become a perfused blood vessel. As a balance of pro- and anti-angiogenic factors is reached, ECs in the tube enter a state of quiescence. In order to cope with the mechanical forces that come with blood circulation, a basement membrane is reestablished and mural cells like pericytes and vSMCs are recruited for vessel stabilization [21]. Which mural cells are recruited

depends on the vessel identity. While pericytes cover the surface of capillaries and immature vessels, vSMCs support arteries and veins (as described in more detail in section 1.1 and figure 1.2). The ultimate fate of a vessel, i.e. if it becomes a capillary, artery or vein, seems to be determined by a combination of distinct gene expression patterns and differences in hemodynamic load [5].

1.2.3 Role of endothelial cells and flow for vascular remodeling

To reach its hierarchical structure, the vasculature constantly undergoes remodeling processes where some vessels grow in diameter while others regress. For the regression (also called pruning) of vessels, two mechanisms have been described. Less commonly, for example in certain transient vascular networks in the eye, apoptosis of ECs in a vascular segment leads to its regression [22]. The overwhelming amount of pruning events, however, are facilitated by collective and directed EC migration away from the pruning region into neighboring vessel branches (figure 1.3) [23, 24]. This process involves the same steps as anastomosis but in reverse order: lumen collapse, junction rearrangement, cell-cell contact loss and EC migration away from the contact site. It has been shown that pruning can be triggered either by low concentrations of VEGF [25] or the loss of perfusion [23]. The former can be understood as ECs following a biochemical signaling cue (low VEGF means sufficient irrigation of the surrounding tissue making the vessel redundant), the latter as ECs following a mechanical signaling cue (low flow rate makes the vessel redundant). This duality is particularly interesting. In recent years, the question of how ECs sense hemodynamics has gained more and more research interest. It seems clear that ECs sense the forces exerted on the vessel wall. These two hemodynamic forces are (1) the circumferential strain, i.e. the stretching force that acts perpendicular to the endothelium and arises from the blood pressure, and (2) shear stress, i.e. the frictional drag that acts parallel to the endothelium and arises from the blood flow [11, 26]. While circumferential strain was shown to play a role for EC morphology and homeostasis *in vitro* [27], it is challenging to observe the same phenomena *in vivo*. On the other hand, work in the mouse and chicken embryo yolk sac elucidated the importance of shear stress for vascular remodeling *in vivo* [28–30]. In fact, a variety of effects of blood flow on ECs have been reported [3]. Under flow, ECs reorganize their focal adhesions and their actin skeleton which influences both their apical-basal and front-rear polarity. As a result, ECs align against the flow (in case of laminar shear stress) or perpendicular to the flow (in case of high shear stress). ECs were also shown to change their expression pattern in regions of turbulent

flow like vessel branches. It is therefore evident that they sense the prevailing flow in the blood vessel and react accordingly to maintain vascular homeostasis. However, the signaling pathways that regulate these processes remain mostly obscured. So far, the most broadly studied and understood mechanism is the reorganization of endothelial junctions under flow which involves a junctional complex of PECAM-1, VE-cadherin and VEGFR2/3 receptors [11]. Several studies also identified the Wnt signaling pathway as a key component [31]. Still, how exactly endothelial mechanosensing works, and which flow conditions induce which EC behaviors, needs further investigation. This question is not only of relevance for developmental vascular biology but also has clinical implications as will become evident in the following section.

1.3 Role of endothelial cells in vascular disease

Numerous pathologies are characterized by defects in the above described processes of vessel growth and vascular remodeling [5, 8].

A number of vascular diseases are characterized by disrupted sprouting angiogenesis. Conditions that have been associated with ischemia resulting from insufficient angiogenesis are, for example, inflammatory diseases such as diabetes, myocardial infarction, certain neurodegenerative disorders or stroke. Conditions that have been associated with enhanced angiogenesis are, for example, age-related macular degeneration and most widely studied- cancer [5]. The tumor vasculature is abnormal in almost any imaginable regard [32, 33]. It is not hierarchically structured but instead features a network of vessels of varying diameters that do not follow a clear function. The vessels are only irregularly perfused and leak into the surrounding tissue. Hence, vascularized tumors are not only subject to excessive angiogenesis but also show massive defects in vascular network patterning and vessel stabilization.

Vascular malformations, characterized by abnormal vascular structure and function, can occur in a variety of tissues. These pathologies have been associated with a number of mutations leading to abnormal EC behavior [3]. One particular example is Hereditary Haemorrhagic Telangiectasia (HHT). HHT patients suffer from arteriovenous malformations (AVMs), which are direct shunts between veins and arteries circumventing blood flow through capillaries. AVMs are prone to rupture and usually occur in several organs such as the brain, liver or lungs. While the exact mechanisms of AVM formation are currently subject to extensive research, it has been shown that both impaired flow-induced inhibition of EC proliferation as well as impaired EC migration against flow can cause AVMs.

On a different note, clinical outcome in stroke patients correlates with the ability of the vasculature to remodel efficiently yielding fast re-irrigation of the affected brain areas [34].

Over the past decade, several pro- and anti-angiogenic drugs have been approved, in particular to treat cancer. However, their impact has not been as effective as hoped. It has become evident that it is not sufficient to solely consider vessel density as an indicator for effective treatment [5, 8]. Instead, other factors such as vessel function also need to be taken into consideration. Therefore, there is a need to further understand the underlying processes that govern vascular growth and network patterning. In particular, unraveling the molecular mechanisms of endothelial dynamics - their response to flow and other stimuli in the blood - has the potential for discovery of new treatment strategies for a broad spectrum of vascular diseases.

1.4 Concluding remarks

This chapter summarized the fundamentals of vascular biology and endothelial dynamics that constitute the foundation and the motivation for the presented work. ECs play an important role for vascular network patterning both in vascular development and disease. Importantly, they seem to sense the hemodynamic conditions like exerted shear stress in the blood vessel and react with active migration from low flow to high flow regions. This behavior leads to the maturation of certain vessels and the regression of others. It is therefore the driver for the hierarchical structure formation of the vasculature. But exactly how EC mechanosensing works remains incompletely understood. Unraveling the molecular mechanisms that regulate sprouting angiogenesis and vascular remodeling will ultimately open up pathways for translational research to identify novel therapeutic targets.

In vivo optical microscopy has emerged as one essential tool to study EC behavior in general, and EC migration in particular, in preclinical vascular research. It allows for high-resolution imaging and hence the observation of single ECs as well as both individual and collective migration *in vivo*. In the following chapter, I will highlight two working models, the zebrafish and the developing mouse retina, that are frequently used for this purpose. I will also elaborate on current limitations of existing imaging setups that I aimed to overcome in the projects presented in this thesis.

Model systems for preclinical optical imaging of endothelial dynamics

2.1 The zebrafish as model system for live *in vivo* imaging of vascular development and disease

In the past decades, the zebrafish (*Danio rerio*), a small fresh water fish native in South Asia, has advanced to one of the most widely used *in vivo* model systems in the field of vascular biology. The transparency of its embryos allows for the live imaging of internal organs, such as the vasculature, with high spatial and temporal resolution with conventional microscopy setups. Since embryonic development occurs within a few days and follows a highly stereotypical series of events, dynamic processes such as vascular sprouting and remodeling can be directly and non-invasively observed simultaneously in a large number of fish. Conclusions with preclinical relevance can be drawn from these observations, as the development of the vasculature follows conserved pathways and is similar to that found in humans. Moreover, an extensive genetic toolbox is available. Many genetically modified lines, for example, transgenic reporters or mutant lines, already exist. New lines are comparatively easy to generate due to the zebrafish's high fertility, large clutch size, short reproduction cycle, and low maintenance cost. It is therefore an excellent alternative to other, more sentient animal models like mice [35].

A schematic overview of the zebrafish anatomy with a focus on the zebrafish vas-

culature is shown in figure 2.1. Major parts of the vascular system are the heart, the brain vasculature and the trunk vasculature. The latter is comprised of the dorsal longitudinal anastomotic vessel (DLAV) along the dorsal side of the trunk, the dorsal aorta (DA) and posterior cardinal vein (PCV) along the ventral side of the trunk, and arranged like the struts of a ladder connecting DA to the DLAV- the arterial and venous intersegmental vessels (aISVs and vISVs, respectively) [36].

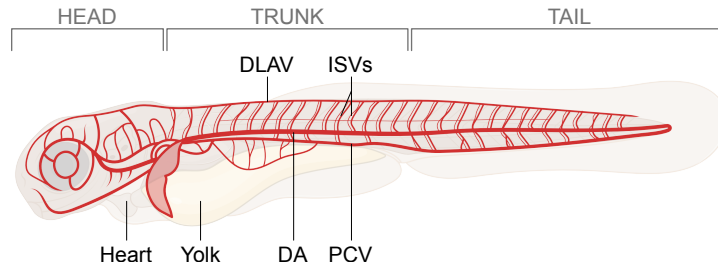


Figure 2.1: Schematic overview of the vascular anatomy of a zebrafish embryo (approximately 3 days post fertilization (dpf)). Main parts of the stereotypical trunk vasculature are labeled: DLAV, dorsal longitudinal anastomotic vessel; DA, dorsal aorta; PCV, posterior cardinal vein; ISVs, intersegmental vessels. A complete atlas of the zebrafish vasculature at different developmental stages can be found in [36]. Created with BioRender.com.

The trunk vasculature with its many ISVs and stereotypical pattern is ideal to study the mechanisms of vascular development. Almost any step of the process can be and has been studied using zebrafish to gain new insights into endothelial dynamics (reviewed in detail in [35] and [37]): from vasculogenesis to sprouting angiogenesis, anastomosis, lumen formation and vascular remodeling. For the latter, the role of blood flow and shear stress on vascular network patterning in general, and EC morphology in particular, have been investigated.

Besides being a useful model organism to study vascular development, research on the zebrafish has also been widely applied to better understand vascular disease and regeneration, showcasing its translational potential [37]. The conducted studies addressed cardiac diseases like cardiomyopathy and conduction defects but also endothelial dysfunction in pathologies like atherosclerosis and stroke. Due to the potential for high throughput experiments, the zebrafish is also being established as a drug screening tool.

In summary, these aspects demonstrate the great potential of the zebrafish model to study vascular development and disease. To observe endothelial morphology and dynamics, many imaging setups like fluorescence confocal microscopy, multi-photon

microscopy (MPM) and lightsheet microscopy have been exploited. However, to better understand the role of shear stress and other parameters, such as blood oxygenation, on endothelial dynamics, novel imaging techniques are required. These techniques should enable the functional imaging of blood to observe flow and oxygenation dynamically and with high spatial resolution. Combining such a technique with conventional optical imaging techniques would permit the direct observation of the reaction of ECs to changing environmental conditions, and establish thresholds of blood flow at which a certain behavior is induced. Therefore, one aim of my work was to establish a photoacoustic microscopy setup which has the potential to fill this gap, as is described in detail in part II of this thesis.

2.2 The developing mouse retina as model system for static *ex vivo* imaging of vascular development and disease

Being one of the few vascular beds that develop after birth, the mouse retina is one of the most widely used model systems to study angiogenesis [38]. *In utero*, the growing tissues of the eye are nourished by a primitive transient vessel network called the hyaloid vasculature, which permeates the vitreous body of the eye. Upon birth, the hyaloids regress and are replaced by the permanent eye vasculature. In the retina, vessels start to sprout centrally around the optic nerve and expand radially towards the periphery in a layer close to the retina's inner surface. At around postnatal day 7 (P7), this layer is entirely covered by the newly established vascular network called the primary plexus. Afterwards, vessels start to sprout into the deeper layers of the retina forming the deeper plexus. While in humans all of these processes happen *in utero*, the overall development of the retinal vasculature is comparable to that in mice, making the mouse retina a suitable model system for clinically relevant studies.

The primary plexus provides the best prerequisites for *ex vivo* imaging. After dissection and fixation (for which well-established protocols have existed for decades), the vasculature presents itself in one flat plane (figure 2.2). Research on the retina also benefits from the many genetic tools (like fluorescent reporters and gene knock-out techniques) and antibodies available for mice. Excitingly, if harvested at the right time (around P6), the vasculature of the retina can be studied simultaneously in all its remodeling stages. At the periphery, ECs are still actively undergoing sprouting angiogenesis to form new vessels. This region is termed the sprouting front. In contrast, the vasculature is actively remodeling or has already remodeled to form mature arteries

and veins closer to the optic nerve. This region is termed the remodeling plexus. Taken together, this means that in the sprouting front, ECs (primarily) follow the biochemical growth signals sent by VEGF, but in the remodeling plexus they follow the mechanical migration signals induced by flow. Hence, the reaction of ECs following the different signaling cues can be observed in the same sample.

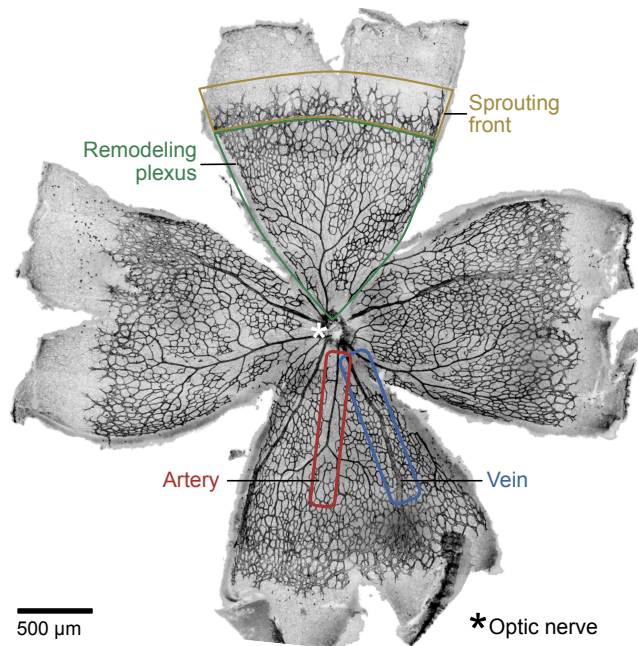


Figure 2.2: Whole-mount developing mouse retina stained for blood vessels. If harvested at P6, the primary plexus contains vasculature of all remodeling stages. At the periphery, endothelial cells are still actively undergoing sprouting angiogenesis (in a region termed sprouting front). Closer to the optic nerve, the vasculature is actively remodeling or has already remodeled to form mature arteries and veins (remodeling plexus).

Experimental work using the mouse retina (reviewed in detail in [39–41]) has made significant contributions to the understanding of vascular development and disease. For example, it was essential for studies uncovering the roles of VEGF [13, 42] and Notch signaling pathways [18, 43] in vascular development. Moreover, it is a well-established tool for the study of human ocular diseases like oxygen-induced retinopathy (OIR) or retinopathy of prematurity (ROP) [40]. Since angiogenic events follow the same pattern anywhere in the body, the mouse retina has also been used to study the aberrant angiogenesis associated with tumor vascularization [44, 45]. However, despite the widespread use of the mouse retina as model system to study angiogenesis, using

2.2. The developing mouse retina as model system for static *ex vivo* imaging of vascular development and disease

it to look at the role of blood flow in endothelial dynamics during vascular remodeling is difficult. Due to its spherical shape, high-resolution live imaging of the endothelium and blood flow is not possible with most conventional microscopy setups. I aimed to overcome this limitation by establishing a new image analysis technique that allows for the extraction of dynamic information from static images of the retina. The details of this project are presented in part III of this thesis.

Objectives and structure of thesis

Despite numerous research efforts and the clinical relevance of the work, many aspects of the role of endothelial dynamics for vascular growth and network patterning still remain obscured. This raises a number of pertinent questions. How is vascular network patterning achieved while maintaining vascular homeostasis? How do endothelial cells facilitate vascular network patterning? What signaling pathways govern endothelial cell migration? How do endothelial cells sense environmental cues like blood flow and blood oxygenation? Which environmental conditions induce which endothelial behaviors? How are endothelial dynamics disrupted in certain vascular diseases?

High-resolution microscopy is an excellent tool to answer these questions, and the zebrafish and developing mouse retina are particularly well-suited model systems to study vascular remodeling *in vivo*. However, novel imaging and image analysis methods are required to extract invaluable quantitative information about the connection of hemodynamics (i.e. the study of blood flow in light of the total arising forces in a vessel) and endothelial dynamics. In my doctoral studies, I contributed to this field in two separate projects. The first project was aimed at developing microscopy methods for functional imaging of blood flow and blood oxygenation in the zebrafish trunk. The second project was aimed at developing a quantitative image analysis method to extract information about endothelial dynamics from static microscopy images of the developing mouse retina.

The following objectives arose for my work:

1. Development and assembly of an optical-resolution photoacoustic microscope for functional imaging of blood vessel networks *in vivo*. To meet the requirements of live *in vivo* imaging in the zebrafish trunk, the photoacoustic microscope had to

fulfill the following criteria:

- 1.1 High spatial resolution in the order of 10 μm to resolve intersegmental vessels (ISVs).
 - 1.2 A fast image acquisition mode to resolve blood flow.
 - 1.3 Spectroscopic imaging capabilities and at least dual-wavelength excitation to allow imaging of blood oxygenation.
 - 1.4 To enable combined live functional imaging of the blood with structural imaging of endothelial cells in the future, it needed to be integrable with other imaging modalities like multi-photon microscopy.
2. Development of a computational image analysis method to extract collective migration principles of endothelial cell populations from static images of the developing mouse retina. The method was based on a lineage-tracing approach and had to provide quantitative information regarding two aspects:
- 2.1 To unravel principles of endothelial cell migration for vascular network patterning, it had to be able to quantitatively assess the distribution of a labeled subpopulation of endothelial cells with respect to the vasculature. By comparing the distributions of endothelial cells that were labeled at the same time point, but observed at different later time points, conclusions could be drawn about endothelial cell migration.
 - 2.2 To be able to unravel molecular pathways controlling endothelial cell migration in the future, the method had to be capable of picking up possible migration defects of endothelial cells that were depleted of certain genes. To demonstrate these capabilities, the depletion of the Rho GTPases Cdc42 and Rac1 was chosen as they are known to affect endothelial cell migration.

In part II of this thesis, I describe the development and application of a photoacoustic microscope (objective 1). In chapter 4, I explain in detail how photoacoustic microscopy works and why it is an excellent imaging modality for functional imaging of the vasculature. I summarize the state of the art, discuss current ultrasound sensing technologies and their limitations in photoacoustic microscopy of vascular networks in general and capillaries in particular. In chapter 5, I describe the optical and technical setup of the all-optical photoacoustic microscope I developed during this project, as well as the details of the image acquisitions that were used to generate the results presented in chapter 6. In chapter 6, I also discuss the results and put them into

context compared to existing work before summarizing them and giving an outlook for future research in chapter 7.

In part III of this thesis, I describe a computational method to extract endothelial migration principles from static images of the developing mouse retina (objective 2). In chapter 8, I describe the motivation as well as existing retina image analysis approaches and their shortcomings. In chapter 9, I explain the method in detail. In chapter 10, I present the results of this project, point out limitations, and compare both the method and the biological results to previous work. In chapter 11, I draw conclusions and show possibilities for future research.

Finally, I summarize the significance of the two projects in part IV.

PART II

Photoacoustic microscopy for *in vivo* functional imaging of the zebrafish trunk vasculature

Abstract and contribution

Optical-resolution photoacoustic microscopy (OR-PAM) is an imaging modality that combines the high spatial resolution of optical microscopy with specificity to endogenous contrast agents like hemoglobin. As it allows for functional quantitative imaging of, for example, blood flow and blood oxygenation, it is a valuable discovery tool for vascular biology. In this work, a novel OR-PAM system with a planar Fabry-Pérot (FP) ultrasound sensor for functional imaging of the zebrafish trunk vasculature was developed. The system features backward-mode operation, broadband detection and high acoustic sensitivity due to minimized source-detector distances. The 3D imaging capabilities of the system were demonstrated in a leaf skeleton phantom and a live zebrafish embryo. To enable spectroscopic imaging of blood oxygenation, the setup includes multi-wavelength excitation tested in ink phantoms. To enable quantitative imaging of blood flow speeds, I developed a fast image acquisition mode, achieving a scan rate of 100,000 A-lines/s. The transparency of the FP sensor for wavelengths in the visible and near-infrared spectrum allows for the integration of the OR-PAM system with other optical imaging modalities like multi-photon microscopy, potentially for simultaneous morphological imaging of the endothelium and functional imaging of blood.

The work presented in this part as well as similar figures are included in the following open access publication:

- **Elisabeth Baumann**, Ulrike Pohle, Edward Zhang, Thomas Allen, Claus Villringer, Silvio Pulwer, Holger Gerhardt and Jan Laufer. A backward-mode optical-resolution photoacoustic microscope for 3D imaging using a planar Fabry-Pérot sensor. *Photoacoustics*, 24:100293, 2021.

This project was realized in close collaboration and under the supervision of Prof. Jan Laufer heading the Medical Physics research group at the University of Halle (MLU Halle). Especially in the first year of the project, I also worked closely together with

Ulrike Pohle, a PhD student from the Medical Physics group. We jointly set up an OR-PAM system in Halle and shared responsibility for setup design, acquisition of components, and setup assembly. In addition, I was responsible for adapting existing image acquisition and image reconstruction software from our collaborators at University College London (UCL) to work with our system. Ulrike Pohle and I also performed initial morphological PA imaging experiments together. After finishing the initial work in Halle, I replicated the system at the MDC in Berlin where I focused on improving the system to meet the requirements set by the intended applications and performing further imaging experiments. In particular, I wrote image acquisition (based on work from our collaborator Thomas Allen at UCL) and image reconstruction software to establish a new scanning mode that is fast enough to resolve blood flow. As first author of the paper, I also took over the majority of manuscript writing, figure compilation and revision work. Besides the co-authors listed above, other people involved in the realization of the project were Master student Albrecht Weiß and research assistant Werner Lebek (MLU Halle) who set up and characterized the Raman laser.

Introduction and Theory

In this chapter, I lay out why photoacoustic imaging in general, and optical-resolution photoacoustic microscopy (OR-PAM) in particular, is the ideal method for completing objective 1 of this work (see chapter 3). First, I briefly cover the fundamental physics of photoacoustics. Second, I explain different photoacoustic imaging modalities and reason why OR-PAM is the only one that fulfills the requirements for the desired imaging applications in the zebrafish trunk. Third, I compare OR-PAM to other biomedical imaging techniques and summarize existing studies of functional OR-PAM, including a review of OR-PAM for imaging blood flow and blood oxygenation. As the ultrasound detection method is another major factor for the realisation of the desired applications, I also explain different detection methods and illustrate why a planar optical Fabry-Pérot (FP) ultrasound sensor is the ideal choice for the OR-PAM system I designed in this project.

4.1 Fundamentals of photoacoustic imaging

In 1880, Alexander Graham Bell discovered that upon irradiation with intensity modulated light, many solid materials emit sound waves [46]. This conversion of optical energy to acoustic energy, which he utilized to develop a "photophone" (a precursor for modern optical communication), was later termed photoacoustic (PA) effect. 100 years after Bell's original research, advancements in laser and ultrasound sensor technology led to the establishment of the research field of photoacoustic imaging (PAI) [47–49].

The PA effect, also called optoacoustic effect, is the underlying principle of all PAI techniques. It comprises the following processes: (1) absorption of photons during a short laser pulse (usually on the order of a nanosecond), (2) conversion of the optical

energy to heat, (3) induction of a local pressure increase, and (4) propagation of that pressure as an acoustic wave (figure 4.1). These processes are described in more detail in the following paragraph.

Upon irradiation with light of the appropriate wavelength, valence electrons of atoms in a target material can absorb the photon energy and get excited to a higher energy state (*step 1 as listed above*). If the relaxation back to the ground state occurs exclusively as non-radiative decay, i.e. in terms of vibrations and collisions but without the emission of e.g. fluorescence, the entire optical energy of the absorbed photon is converted to thermal energy (*2*). As a result, the local temperature increases. Instead of reacting with thermal relaxation to the temperature rise, a local pressure increase occurs in the tissue, if the conditions for thermal and stress confinement are met (*3*). This means that the rate of heating needs to be faster than the thermal response time of the material (which depends on its linear dimensions and its thermal diffusivity) as well

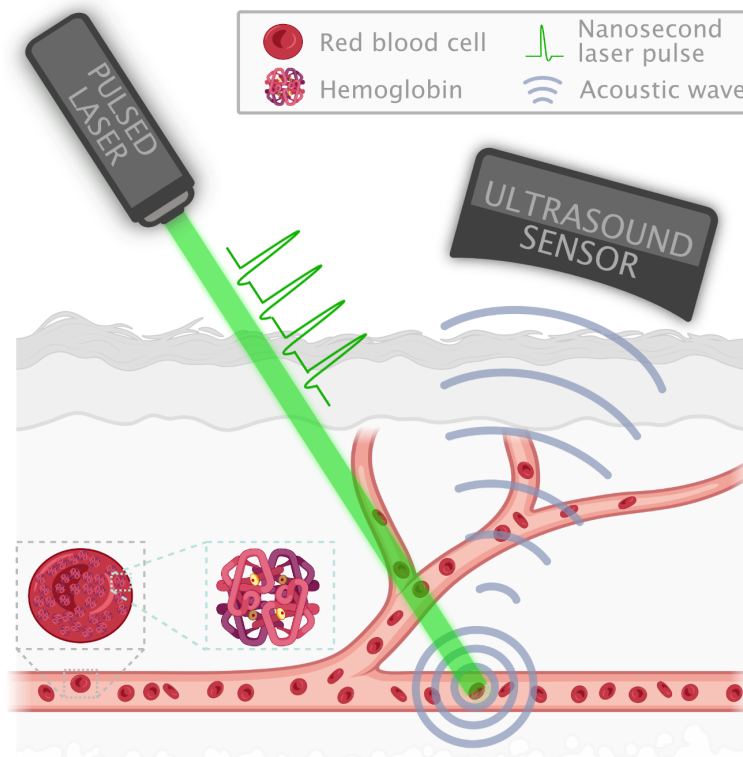


Figure 4.1: Schematic overview of photoacoustic imaging of the vasculature. Hemoglobin sitting on red blood cells (RBCs) absorbs photons during nanosecond laser pulses. Due to the photoacoustic effect, an acoustic wave is generated that can be detected with an ultrasound transducer. Created with [BioRender.com](https://www.biorender.com).

as the time it takes an acoustic wave to travel through the heated region (which also depends on the linear dimensions as well as the speed of sound in the target material) [50, 51]. The local pressure increase propagates as an acoustic wave through the target material and can be detected with an ultrasound sensor (also called transducer) adjacent to the organism (4). This signal is called the PA signal. In the case of biological tissue, it travels with a speed of sound of approximately 1.5 mm/ μ s [50].

For PAI, a sample is irradiated with intensity-modulated excitation light over a desired field of view (FOV). The excitation pulses generate PA waves within the illuminated volume which are measured as PA signals to obtain an image. While PA waves can be excited with low-frequency light intensity modulations (e.g. in gas phase PA spectroscopy [52]), a sufficiently short excitation laser pulse is critical for PAI. In that case, the PA wave in fact encodes the local distribution of the initial pressure. For too long excitation pulses, however, that localization is smeared.

The image intensity and contrast directly reflect how much light was absorbed by the irradiated sample at each voxel. The amplitude of the PA signal is proportional to the initial pressure p_0 . p_0 at position $\vec{r} = [x, y, z]$ can be described with the following equation [47, 50, 53]:

$$p_0(\vec{r}) = \Gamma \mu_a(\vec{r}) \Phi(\vec{r}), \quad (4.1)$$

where Γ is the Grüneisen coefficient, $\mu_a(\vec{r})$ the absorption coefficient and $\Phi(\vec{r})$ the local fluence.

The Grüneisen coefficient Γ is a material-dependent dimensionless quantity that describes the conversion of thermal energy to stress in the target material [54]. It is defined as $\Gamma = \beta c_s^2 / C_p$ with the thermal coefficient of volume expansion β , the speed of sound c_s and the specific heat capacity at constant pressure C_p .

The term $\mu_a(\vec{r}) \Phi(\vec{r})$ describes the absorbed energy density at position \vec{r} . The absorption coefficient $\mu_a(\vec{r})$ is a measure of the probability with which a photon is absorbed per unit path length. It is therefore expressed in mm^{-1} . $\mu_a(\vec{r})$ depends on the wavelength of the light as well as the number density of absorbers and their absorption cross section. The fluence $\Phi(\vec{r})$ is a measure of the number of photons per unit area at position \vec{r} . How the fluence changes with increasing depth, and therefore how light is attenuated as it travels through an ideal non-scattering absorber, is described by the Beer-Lambert law [55, 56]. According to the Beer-Lambert law, the proportion of light that is absorbed per unit path length dz remains constant:

$$\frac{d\Phi}{dz} = -\mu_a \Phi. \quad (4.2)$$

Solving differential equation 4.2 yields an exponential decay with increasing depth for the fluence Φ [57]:

$$\Phi(z) = \Phi_0 e^{-\mu_a z}. \quad (4.3)$$

4.2 Modalities of photoacoustic imaging

One of the advantages of PAI is its scalability in terms of spatial resolution and imaging depth. Depending on the desired application, a different implementation of PAI can be used to either achieve imaging depths up to several centimeters or lateral resolutions down to several microns. Overall, PAI setups can be split into three categories (figure 4.2): Photoacoustic tomography (PAT), acoustic-resolution photoacoustic microscopy (AR-PAM), and optical-resolution photoacoustic microscopy (OR-PAM).

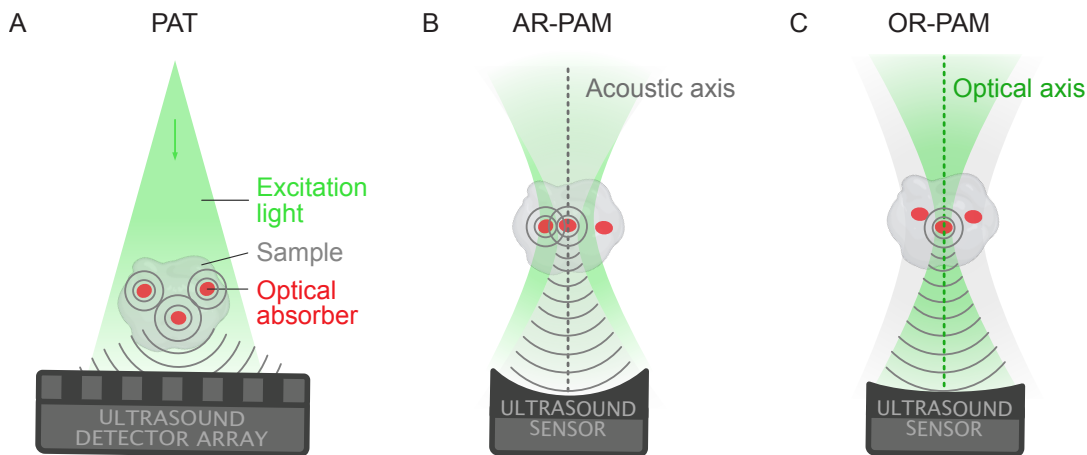


Figure 4.2: Different modalities of photoacoustic imaging. For reasons of clarity, all implementations are presented in transmission mode (PA wave excitation and detection on different sides of the sample). **A** Photoacoustic Tomography (PAT). The excitation light is diffusely distributed over a large volume, generating PA waves in all optical absorbers present in that volume. PA signals are detected by a transducer array. Images need to be reconstructed computationally. **B** Acoustic-resolution photoacoustic microscopy (AR-PAM). A weak optical focus coincides with a tight acoustic focus of the ultrasound transducer. Only PA waves generated within the acoustic focus are detected. **C** Optical-resolution photoacoustic microscopy (OR-PAM). Excitation light is tightly focused into the sample. PA waves are only generated in absorbers within the optical focal volume.

PAT allows for large imaging depths but at the cost of spatial resolution. In contrast, OR-PAM allows for high spatial resolution but only low imaging depth. In terms

of resolution and depth, AR-PAM ranks between PAT and OR-PAM, meaning it provides lower imaging depth and higher resolution than PAT but higher imaging depth and lower resolution than OR-PAM [58]. The principle and use cases of the different modalities are presented in the following sections.

For macroscopic imaging, PAT allows imaging over a FOV of several cm^2 with a lateral resolution of around $500\ \mu\text{m}$ and an imaging depth of several centimeters [59]. In PAT, a non-focused pulsed excitation laser illuminates an imaging sample over the required FOV (figure 4.2A). PA waves are generated within the entire illuminated tissue volume. These waves are usually detected with an ultrasound transducer array and PA images are reconstructed for which an additional computational step is necessary. A number of different reconstruction algorithms, for example, back-projection or time-reversal algorithms, have been reported [60–63]. Due to reconstruction artefacts, unknown local fluences and other uncertainties, quantitative PAT is currently challenging such that it is mostly used for morphological imaging of the vasculature requiring rather large FOV. Examples are imaging of the brain vasculature through the intact skull, imaging of the vasculature in breast tumors and imaging vasculature in extremities below the skin surface [64–67].

For applications requiring higher spatial resolution, PAI can be implemented in the form of photoacoustic microscopy (PAM), which is divided into AR-PAM (higher imaging depth) and OR-PAM (higher lateral resolution). In AR-PAM, a typical lateral resolution is approximately $80\text{--}100\ \mu\text{m}$ for imaging depths up to around $5\ \text{mm}$ [68]. PA waves are excited using a weakly focused excitation laser and detected using a tightly focused ultrasound detector (figure 4.2B). The transducer and the excitation beam are typically mechanically scanned across the FOV. In contrast to PAT, only PA waves generated within the acoustic detection cone are detected at each scanning location. Therefore, 3D information of the sample is directly obtained without any image reconstruction. Due to the much weaker acoustic attenuation, as compared to optical attenuation, in tissue, the imaging depth for AR-PAM lies still far beyond the optical diffusion limit. The vertical resolution (i.e. the depth resolution) is limited by the frequency response of the ultrasound sensor (see section 4.5 for a definition). The lateral resolution (i.e. the resolution in the x-y-plane) is limited by the point spread function (PSF) of the focused ultrasound transducer.

In OR-PAM, lateral resolutions below the diffraction limit have been achieved but at the cost of imaging depth [69]. Here, PA waves are excited by a tightly focused excitation laser and detected with a weakly focused ultrasound sensor (figure 4.2C). Therefore, the lateral resolution depends on the PSF of the optical focus like for other

optical microscopy modalities. As in the case of AR-PAM, the excitation beam is scanned across the FOV. PA waves are only generated along the optical axis of the excitation beam such that additional image reconstruction is not needed. In contrast to optical backward-mode microscopy techniques, light has to travel only half the distance through scattering media (as it does not have to travel back to the detector) such that the imaging depth limit of OR-PAM is still about twice the optical diffusion limit. However, it needs to be noted that the spatial resolution of optical microscopy modalities like multi-photon microscopy (MPM) is still much higher than the spatial resolution of OR-PAM.

Of the three PAI modalities, only OR-PAM provides the desired spatial resolution for imaging the zebrafish trunk vasculature. Therefore, it was selected for this project. In the following section, I will compare OR-PAM to other high-resolution and functional imaging techniques and explain why it is best suited for the desired application.

4.3 Comparison of OR-PAM and other biomedical imaging techniques

For many decades, the development of imaging modalities has made great impact on the biomedical sciences both in the clinical setting and in preclinical research. In this work, the envisaged application comprised preclinical functional imaging of the zebrafish vasculature. Therefore, the imaging system had to fulfill these three requirements: (1) high spatial resolution to resolve vessels in the zebrafish trunk, (2) ability of spectroscopic imaging of hemoglobin to quantify oxygen saturation, and (3) ability to quantify blood flow. In the following, I explain why OR-PAM is ideally suited and preferred over other imaging modalities for this project.

4.3.1 OR-PAM in comparison to optical microscopy techniques

In terms of spatial resolution, OR-PAM is typically at a disadvantage compared to optical microscopy techniques like MPM (even though super-resolution approaches have been reported [69–72]). However, for shallow imaging depth, spatial resolutions of around 10 μm can be readily achieved, which is sufficient to resolve the zebrafish trunk vasculature [54, 73]. In addition, the contrast in PAI is completely based on light absorption. This means that PA images do not suffer from background noise like autofluorescence. Furthermore, OR-PAM does not require depth stack scanning as the PA signal travel time directly provides information about the signal source depth. More-

over, in contrast to MPM, OR-PAM can be used for functional imaging of hemoglobin to quantify oxygen saturation and blood flow without the need of a fluorescent label (as described in more detail in section 4.4.1). This comes with several advantages. First, it allows for the live *in vivo* morphological imaging of these molecules in an unperturbed state. Second, the molecules are inherently non-toxic for the organism. Third, OR-PAM does not succumb to the pitfalls that come with photobleaching [73]. Compared to other biomedical imaging techniques, OR-PAM is advantageous for functional imaging of the zebrafish trunk vasculature as will become evident in the following paragraphs.

4.3.2 Imaging of blood oxygen saturation

The blood oxygenation, sO_2 , is an important indicator for tissue viability but also for active vascular growth. The level of tissue oxygenation can be distinguished into normoxia (normal level of oxygenation), hyperoxia (elevated oxygenation) and hypoxia (diminished oxygenation). In development, hypoxia induces the secretion of vascular growth factors like VEGF which activates sprouting angiogenesis and vessel growth (see chapter 1) [5]. In cancer, both hyperoxia and hypoxia are important quantities for ranking malignant tumors. Therefore, noninvasive imaging of the differences of deoxygenated and oxygenated hemoglobin (HbR and HbO₂, respectively) to quantify blood oxygenation has been deployed in clinical and research settings for many decades [74].

Already in the early nineties, blood oxygen level dependent (BOLD) magnetic resonance imaging (MRI) made use of the different magnetic properties of HbR and HbO₂ and formed the foundation of the field of functional MRI (fMRI) [75, 76]. However, besides the high maintenance cost of MRI scanners, BOLD comes with other disadvantages such as the sole relative observation of hemodynamic differences, low temporal resolution and therefore no live imaging capabilities as well as typical spatial resolutions in the mm-range [76].

Other imaging techniques rely on the absorption or scattering of light by hemoglobin. For example, pulse oximetry is based on light absorption of hemoglobin at different wavelengths. Due to its easy setup, it is the most-widely used technique to assess blood oxygen saturation in the clinic [77]. However, it only offers point-measurements without spatial resolution. Therefore, it can only provide information about how much oxygen is bound to hemoglobin on average but not if that oxygen was in fact passed on to the tissue. OR-PAM, however, has the potential to follow single red blood cells (RBCs) as they release oxygen [78]. Moreover, pulse oximetry only measures blood oxy-

generation in arteries as it relies on the blood pumping frequency and does not provide reliable measurements for oxygen saturation values below 70% [74].

Reflectance imaging also relies on hemoglobin absorption. Depending on the number of used excitation wavelengths, it can be implemented as multispectral or hyperspectral imaging. Its capabilities for *in vivo* applications over large FOVs of several cm^2 [79] and even a clinical study for measuring the oxygenation in neonates [80] have been reported. On the downside, it is limited to imaging vasculature just below the sample surface up to around 200 μm . Furthermore, it is relatively costly, comes with uncertain reliability and does not provide depth resolution [74].

A method that does provide depth resolution is diffuse optical imaging (DOI), which exploits the scattering in tissue [81]. It has been combined with ultrasound (US) for deep imaging of the placenta [82]. DOI can resolve additional biomarkers besides hemoglobin and, in combination with diffuse correlation spectroscopy (DCS), can even resolve blood flow but suffers from low spatial resolution of several mm [74].

On the other hand, spectroscopic optical coherence tomography (OCT) is a technique that also provides depth resolved imaging of blood oxygenation but at high spatial resolution [83, 84]. However, the spectroscopic OCT setup is more complex than an OR-PAM setup as it requires a supercontinuum light source and a quantitative image analysis that is very susceptible to offsets in the used wavelengths.

In contrast to all other mentioned techniques, OR-PAM unites all necessary and advantageous features for quantitative imaging of blood oxygenation: high spatial resolution, depth-resolved information and comparatively easy and low-cost optical setup.

4.3.3 Imaging of blood flow

Another important hemodynamic parameter of the vasculature is blood flow [3]. It determines the exerted wall shear stress (WSS) on the blood vessel wall which plays a key role for endothelial dynamics in vascular development and disease as outlined in chapter 1 of this thesis. Because of its importance, a variety of biomedical imaging techniques have been used to quantify blood flow. In the following, I will illustrate why OR-PAM is the most suitable technique for my project.

MRI can be used to quantify blood flow with relatively high sensitivity and spatial resolution [85, 86]. However, MRI scanner purchase and maintenance are costly and long pulsing schemes result in slow image acquisition. Computed tomography (CT) can also quantify flow but at lower spatial resolution. In addition, it requires ionizing radiation and usually also injection of a contrast agent [87].

Quantitative imaging of blood flow can also be facilitated with optical methods such as DCS, laser speckle contrast imaging (LSCI) or laser Doppler flowmetry (LDF). However, these techniques are either confined to single-point measurements or provide only low spatial resolution [74]. Other optical microscopy techniques like MPM do provide high spatial resolution but are limited to vessels in the focal plane (as they do not provide depth information without z-stacking) and require fluorescent markers for labeling RBCs [87].

Doppler US and blood flow velocity using OCT are other techniques for depth-resolved imaging of blood flow. However, their low contrast to RBCs and their susceptibility to clutter artefacts make it difficult to use them to image flow in small vessels or near vessel walls [88, 89].

PAM does not suffer from any of the pitfalls mentioned above. It is relatively low-cost, offers high spatial and temporal resolution as well as depth-resolved information. Due to its specific absorption-based contrast of endogenous hemoglobin, blood vessels are clearly distinguished from the surrounding tissue [90], even in capillaries, with higher signal-to-noise ratio (SNR) than Doppler US or OCT [91, 92]. Different methods for imaging flow with PAM have been developed, which I review in section 4.4.2.

In summary, OR-PAM has a lot of potential for the envisaged *in vivo* applications in a zebrafish model. In the following sections, I shortly summarize current state-of-the-art preclinical OR-PAM applications relevant for vascular biology. Furthermore, I provide the context for my work and outline my contribution to the scientific knowledge.

4.4 OR-PAM of the vasculature

Due to the qualities of PAI outlined in the previous sections, the PA research community has recorded strong growth in recent years. Many exciting studies have been performed to advance the field. One aspect of these studies was the technological development of, for example, faster and more compact scanners [93–99], better optical focusing [100–103] and different ultrasound detectors [104] to enable clinically and preclinically relevant applications. The number and variety of these applications is enormous. As outlined in several reviews, they span preclinical studies in mouse and zebrafish animal models to clinical studies in humans, pathologies from atherosclerosis to diabetes to skin cancer, excitation wavelengths from ultraviolet (UV) to near-infrared (NIR) light, and spatial resolutions from several tens of microns down to sub-diffraction [51, 54, 73, 105–109].

In the field of vascular biology, especially OR-PAM with its high spatial resolution has the potential to be both a tool for preclinical and basic research of the vasculature as well as a clinical diagnostics tool for vascular diseases. For example, it has been applied to study angiogenesis and disrupted microvasculature in animal models of human diseases such as the tumor microenvironment [110, 111] or diabetes [112] as well as to monitor the success of anti-angiogenic therapy [113]. For the intended applications of the OR-PAM system developed in this project, two features of OR-PAM are of particular interest: (1) label-free imaging of endogenous molecules like hemoglobin, and (2) functional imaging of spatially resolved parameters like blood flow and blood oxygenation.

While exogenous contrast agents like gold nanoparticles [114] or microrobots [115] have been validated as suitable targets for OR-PAM, imaging of endogenous molecules holds several advantages as they are inherently non-perturbing to the studied system, avoid issues such as toxicity and also do not require genetic modifications [54]. In principle, any light-absorbing molecule can be imaged with OR-PAM. Besides hemoglobin, OR-PAM studies for the imaging of deoxyribonucleic acid (DNA)/ribonucleic acid (RNA) [116, 117], melanin [118, 119], lipids [120], glucose [121] and water [122] have been reported. Still, these are outnumbered by the studies targeting hemoglobin. Reasons for this are, e.g., the clinical relevance of imaging hemoglobin and its high absorption in the visible wavelength range (for which excitation laser systems are readily available). Unlike, for example, DNA and RNA, hemoglobin molecules also remain stable after light absorption.

As mentioned above, OR-PAM provides another relevant feature for the motivation of this project: it can be used to obtain spatially resolved information about blood oxygenation and blood flow. Since these are the OR-PAM features that have the potential to complement high-resolution structural imaging of the endothelium to gain insights into endothelial dynamics during vascular remodeling, they are reviewed in detail in the following sections.

4.4.1 Quantitative imaging of blood oxygen saturation using OR-PAM

The blood oxygenation, sO_2 , is defined as the ratio of the concentration of oxygenated hemoglobin [HbO_2] with respect to the total hemoglobin concentration [Hb] [74, 105]:

$$sO_2 = \frac{[HbO_2]}{[Hb]} = \frac{[HbO_2]}{[HbO_2] + [HbR] + [HbCO_2] + [HbCO] + [HbMet] + [HbSulf]}. \quad (4.4)$$

[Hb] is the sum of individual concentrations of different hemoglobin states: [HbO_2], deoxygenated hemoglobin [HbR], carbaminohemoglobin [$HbCO_2$], carboxyhemoglobin [$HbCO$], methemoglobin [$HbMet$] and sulfhemoglobin [$HbSulf$] [74]. In healthy organisms, [$HbCO_2$], [$HbCO$], [$HbMet$] and [$HbSulf$] are not present in physiologically relevant concentrations [74], such that equation 4.4 simplifies to:

$$sO_2 = \frac{[HbO_2]}{[HbO_2] + [HbR]}. \quad (4.5)$$

Imaging of blood oxygenation with OR-PAM has been widely demonstrated [54, 73, 123–128]. It makes use of the fact that the absorption spectra of HbO_2 and HbR differ slightly (see figure 4.3) and that OR-PAM can be used to distinguish two or more chromophores with different absorption spectra by spectroscopic imaging. Besides the application in the vasculature, this has, for example, been demonstrated to separate the PA signals of cell nuclei and cytoplasm in fibroblasts [105].

To perform spectroscopic OR-PAM, the sample is typically irradiated sequentially with two or more different excitation wavelengths. If these are chosen such that one wavelength is highly absorbed by one chromophore but poorly absorbed by the other, and another wavelength induces the opposite absorption behavior, each image encodes information for one chromophore. However, the absorption spectra of HbO_2 and HbR overlap significantly such that spectral unmixing needs to be performed. The easiest and most readily implemented way to quantify sO_2 using OR-PAM is a linear model based on least-squares fitting [105, 123, 124, 130]. The linear model assumes a constant fluence $\Phi(\lambda_i) = \Phi$ for different excitation wavelengths λ_i and therefore a direct proportionality of the measured PA signal amplitude $A(\lambda_i)$ to the absorption coefficient μ_a :

$$A(\lambda_i) \propto \mu_a(r)\Phi. \quad (4.6)$$

While this is not strictly true for light traveling through tissue, it is a reasonable assumption for imaging depths of less than 1 mm as scattering is negligible [123]. μ_a can be expressed as the sum of the products of concentration c_k and molar extinction

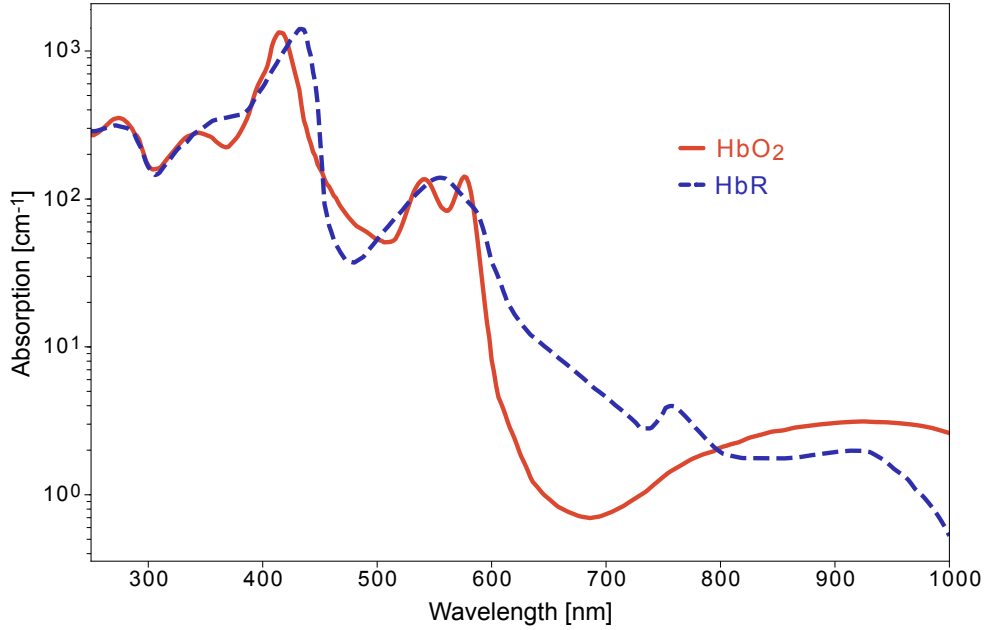


Figure 4.3: Optical absorption spectra of oxygenated (HbO_2) and deoxygenated (HbR) hemoglobin. Data taken from [129].

ϵ_k of each chromophore k present in the sample:

$$\mu_a(r) = \sum c_k \epsilon_k(\lambda). \quad (4.7)$$

Combining equations 4.6 and 4.7 and assuming only HbO_2 and HbR to be present absorbers in the sample results in the following expression for $A(\lambda_i)$ [105]:

$$A(\lambda_i) \propto [[\text{HbR}]\epsilon_{\text{HbR}}(\lambda_i) + [\text{HbO}_2]\epsilon_{\text{HbO}_2}(\lambda_i)]\Phi. \quad (4.8)$$

Using the theory of least-squares fitting, $[\text{HbR}]$ and $[\text{HbO}_2]$ can be expressed in dependence on $A(\lambda_i)$ obtained at two distinct excitation wavelengths λ_1 and λ_2 as follows [105]:

$$[\text{HbR}] = K \frac{A(\lambda_1)\epsilon_{\text{HbR}}(\lambda_2) - A(\lambda_2)\epsilon_{\text{HbR}}(\lambda_1)}{\epsilon_{\text{HbR}}(\lambda_1)\epsilon_{\text{HbO}_2}(\lambda_2) - \epsilon_{\text{HbR}}(\lambda_2)\epsilon_{\text{HbO}_2}(\lambda_1)} \quad (4.9)$$

and

$$[\text{HbO}_2] = K \frac{A(\lambda_1)\epsilon_{\text{HbO}_2}(\lambda_2) - A(\lambda_2)\epsilon_{\text{HbO}_2}(\lambda_1)}{\epsilon_{\text{HbO}_2}(\lambda_1)\epsilon_{\text{HbR}}(\lambda_2) - \epsilon_{\text{HbO}_2}(\lambda_2)\epsilon_{\text{HbR}}(\lambda_1)} \quad (4.10)$$

with a constant factor K . Combining equations 4.5, 4.9 and 4.10 yields an expression

for the blood oxygen saturation, sO_2 :

$$sO_2 = \frac{A(\lambda_1)\epsilon_{HbR}(\lambda_2) - A(\lambda_2)\epsilon_{HbR}(\lambda_1)}{A(\lambda_1)[\epsilon_{HbR}(\lambda_2) - \epsilon_{HbO_2}(\lambda_2)] - A(\lambda_2)[\epsilon_{HbR}(\lambda_1) - \epsilon_{HbO_2}(\lambda_1)]}. \quad (4.11)$$

Since sO_2 is a relative quantity, $[HbO_2]$ and $[HbR]$ do not need to be quantified in absolute units as K cancels out. All other variables are known: $\epsilon_{HbO_2}(\lambda_i)$ and $\epsilon_{HbR}(\lambda_i)$ can be obtained from published absorption spectra (as shown in figure 4.3), and $A(\lambda_i)$ are the measured PA signal amplitudes.

To minimize the error in least-squares fitting resulting from uncertainties in the experimental setup (e.g. deviating λ_i), more than two excitation wavelengths can be used [124].

While for OR-PAM setups a wavelength-independent fluence is a reasonable assumption, the described approach cannot be readily translated to other PAI modalities aiming at deeper imaging depths as light of different wavelengths is scattered and absorbed to different degrees. Hence, the assumption $\Phi(\lambda_i) = \Phi$ does not hold. Optimally, the different fluences would be measured but this is unfeasible in tissue. To overcome this limitation and improve sO_2 measurements with PAI at greater imaging depths, several alternative methods have been demonstrated [126, 130–137]. For example, Danielli et al. as well as Yao et al. used two single-wavelength excitation pulses of different widths to exploit the absorption saturation differences between HbR and HbO₂ [126, 131], Guo et al. used the acoustic spectra of PA signals to obtain μ_a [132, 133], Kirchner et al. proposed a machine learning model to extract information about the optical absorption [134] and Tzoumas et al. used modeling of eigenspectra assuming unknown fluence values for improved sO_2 imaging in deep tissues [135]. Since OR-PAM applications like the one envisioned for the imaging system presented in this thesis require only shallow tissue imaging within the optical diffusion limit (< 1 mm), the sO_2 can be determined with sufficient accuracy from PA signals obtained at different wavelengths according to equation 4.11 [123, 130].

In summary, methods for obtaining sO_2 using OR-PAM have been demonstrated in a large number of studies. To use them for potential discoveries of the role of oxygen level dynamics for endothelial dynamics, they need to be implemented in an OR-PAM system that is combined with an optical microscope for high-resolution imaging of the endothelium. This will enable the direct observation of the EC response to changing oxygenation conditions.

4.4.2 Quantitative imaging of blood flow using OR-PAM

Similar to the amount of studies showing the potential of OR-PAM to quantify blood oxygenation, measuring blood flow using AR-PAM and OR-PAM has also been widely demonstrated [87]. Some of these studies target the flow in only a single blood vessels. For example, Yao et al. determined the blood flow speed in a single vessel by fast-scanning repeatedly along its vertical axis. They used this information to follow the fractional change of cerebral blood flow *in vivo* in the mouse brain [126]. Kim et al. developed a super-resolution OR-PAM system with which they could follow individual RBCs in the mouse ear and estimate their flow speed in a capillary [72].

Using PAM to obtain maps of the vasculature with spatially resolved blood flow is not as straight-forward but desirable for many applications like the one envisaged for this project. Several approaches for this have been reported in the literature [87]. Overall, they can be distinguished into these categories: (1) making use of the Doppler shift of moving RBCs, (2) measuring the transit time it takes an RBC (or a cluster of RBCs) to flow through a defined excitation spot size, (3) modulating the PA amplitude and observing its return to normal due to flow, (4) using spatial or temporal cross-correlation of PA signals acquired of moving RBCs, and (5) direct observation of flow by high-speed image acquisition.

The Doppler effect of flowing RBCs (category 1 in the list above) can be used by either temporally (for example, with a cw laser [138]) or spatially (for example, by creating illumination fringes [139, 140]) modulating the excitation light. In both cases, the PA response of the flowing RBCs is Doppler shifted which can be used to obtain their flow speed. However, so far Doppler shift PAM has only been demonstrated with acoustic lateral resolution [87].

Measuring the time it takes single RBCs or RBC clusters to transit through the optical focus is another way to estimate blood flow using OR-PAM (category 2) [141, 142]. It has been demonstrated *in vivo* in chicken embryos [143, 144]. Ning and colleagues applied this approach to wide-field imaging [127]. They demonstrated the capabilities of their system to image $[Hb]$, sO_2 and blood flow speeds *in vivo* in backward-mode in the mouse ear. However, the transit time method requires precise knowledge of the particle sizes and the size of the optical focus for accurate measurements. Especially the latter is difficult due to optical scattering in tissue. To overcome this, wavefront shaping has been used but it could not fully redeem the issue [87, 145].

A third method to quantify flow with PAM is amplitude encoding (category 3). For example, this can be achieved by photoconverting the shape of nanorods which induces

a change in PA amplitude. How fast the PA amplitude recovers gives information about the flow speed of the nanorods [146, 147]. This technique relies on the use of photoconvertible exogenous contrast agents and is therefore not easily feasible *in vivo*. However, the PA amplitude can also be modulated by temporarily introducing heat to the system [148, 149]. This has been implemented to quantify blood flow *in vivo* in backward-mode in the mouse ear. Liu et al. developed what they termed single-shot multi-parametric PAM [150]. They proposed a method for measuring blood flow by quantifying the PA signal decay of two excitation pulses shot within ≈ 300 ns at the same location and making use of the Grüneisen relaxation effect. Since the tissue heats up due to the energy deposition of the first excitation pulse, the Grüneisen coefficient of the pressure wave generated from the second pulse increases. By how much depends on the flow of the absorbers (i.e. hemoglobin) which they could therefore infer from the two signal amplitudes. In addition, they measured $[Hb]$ (after calibration) and sO_2 from the three different excitation wavelengths in a single scan. They further evolved the system to include a Raman laser with five excitation wavelengths to increase accuracy [151]. While amplitude heat encoding is a promising method for *in vivo* flow imaging, it is difficult to integrate into my system due to the temperature sensitivity of the Fabry-Pérot ultrasound sensor.

Cross-correlation (category 4) is most easily embedded into raster-scanning OR-PAM setups that can also be used to quantify the sO_2 . Such a setup that can be used to image both sO_2 and flow (as envisaged for this project) is termed multi-parametric OR-PAM. In the cross-correlation approach, the goal is to correlate signals originating from the same RBC or RBC cluster. To quantify flow in the axial axis, this can, for example, be achieved by exciting PA signals with two short time-delayed laser pulses (temporal cross-correlation) [152]. To quantify flow in the lateral axis, this can be achieved by exciting PA signals at two different locations that are a certain distance apart (spatial cross-correlation) [78]. However, dense sampling is necessary to obtain enough information to couple PA signals to quantify blood flow. This has a negative impact on image acquisition speed. Therefore, most applications cannot provide video-rate frame rates or are limited to relatively small FOVs. Due to slow image acquisition, this approach is also prone to motion artefacts. In recent years, efforts have been made to overcome this limitation. Zhong, Wang and colleagues developed high-speed multi-parametric OR-PAM. Initially, the system could only be operated in transmission-mode and was applied to the mouse ear [153]. Afterwards, they changed the setup to operate in backward-mode to study fast microvascular responses in the mouse brain [154]. Finally, they also developed a novel ultrasound sensing setup based on a focused

piezoelectric transducer to achieve frame rates of 0.3 Hz over a FOV of $4.5 \times 3 \text{ mm}^2$ with a spatial resolution of $7 \text{ }\mu\text{m}$.

Flow can also be imaged directly by following individual RBCs over time (category 5). This approach requires a high acquisition speed and a frame rate of at least 20 Hz in the zebrafish trunk [78]. Since it provides the most accurate quantification of flow (direct observation at high spatial resolution, no estimation of optical focus needed, no heat deposition in the sample or ultrasound sensor, insusceptible to motion artefacts), this method was chosen for this project.

The last sections clearly showcase the potential of OR-PAM for preclinical imaging of the vasculature and to fulfill the aims of the first project of my doctoral studies, i.e. high-resolution functional imaging of blood oxygenation and blood flow in the zebrafish trunk (see chapter 3). The success of the last aim, integrability with other optical microscopy techniques for simultaneous structural imaging of the endothelium and functional imaging of the blood, largely depends on the used ultrasound transducer. In the following section, I give a brief introduction into ultrasound sensing for OR-PAM and explain why a planar Fabry-Pérot (FP) sensor was used in this project.

4.5 Ultrasound detection in OR-PAM

4.5.1 Important characteristics of ultrasound transducers for OR-PAM

The suitability of transducers for ultrasound detection of the OR-PAM system developed in this project can be assessed using the following characteristics [104]:

- *Sensitivity.* The sensitivity of an ultrasound sensor specifies the minimal pressure amplitude that can be detected. Usually, it is declared in relation to the noise level of the detector as noise-equivalent pressure (NEP). It should be noted that NEP values are only meaningful if the bandwidth they were measured over is stated [155]. Depending on the source depth, PA signal pressures range from sub-Pa to kPa.
- *Bandwidth.* The bandwidth, or frequency response, indicates what range of signal frequencies can be detected by a sensor. It is a critical characteristic for the spatial resolution of the system, as it determines which range of structure size can be resolved. Generally, for superficial imaging as in OR-PAM, PA signals are expected to exhibit high frequencies of $> 100 \text{ MHz}$ spanning a wider range

compared to deep-tissue imaging where acoustic attenuation becomes a concern. For example, PA signals generated by RBCs are expected to have frequencies > 150 MHz [156]. In principle, bandwidth is also coupled to sensitivity. If most of the frequency components of the wanted signal are filtered out, the SNR will be negatively affected.

- *Active element size.* The spatial resolution of the system depends inversely on the active element size of the detector. Hence, small element sizes are preferred for OR-PAM applications. However, for conventional piezoelectric ultrasound sensors, a decrease in active element size results in a decrease in sensitivity. For optical ultrasound sensors this is not the case (as discussed in section 4.5.2). The size and geometry of the active element also determines the sensor directionality.
- *Directionality.* The directionality of a detector describes which range of angles of incoming acoustic waves can be detected. As a higher acceptance angle means higher spatial resolution, omni-directionality is preferred. However, this characteristic is more of a concern for PAT applications and less important for OR-PAM.

4.5.2 Different types of ultrasound transducers

Several different types of ultrasound sensors have been developed for OR-PAM. Piezoelectric transducers are the most commonly used type. The piezoelectric effect is observed in certain ferroelectric materials, and results in an electric charge upon the exposure to mechanical forces like compression. While these sensors are readily available and have been applied in the majority of OR-PAM studies, they come with several disadvantages [104]. First, due to their active element size, they typically only have a limited range of acceptance angles. Second, their typical frequency response is resonant around a center frequency. This is disadvantageous because PA signals of small structures, as targeted in OR-PAM applications, exhibit a broad frequency range up to several hundred MHz [156]. Third, for imaging setups operated in backward-mode (i.e. signal generation and detection on the same side of the sample), they cannot be placed immediately adjacent to the signal source due to their opacity. Since small structures can be considered point sources of spherical PA waves, the further away the detector the higher the loss of PA pressure, as p_0 scales inversely with radius r ($p_0 \propto 1/r$). Also, guiding the excitation light to the sample while still maintaining acoustic coupling to the sensor (to avoid impedance mismatches) increases setup complexity. Nevertheless, backward-mode detection is especially important for *in vivo* applications as samples are

usually non-transparent and of thickness greater than the OR-PAM imaging depth. To overcome this issue, transparent piezoelectric sensors have been developed. However, they showed strongly resonant frequency responses [157–161].

Optical ultrasound sensors offer an alternative to conventional piezoelectric transducers. In general, they can be distinguished into sensors whose principle of operation relies on refractometric methods or on interferometric methods. Sensors relying on refractive methods make use of, for example, beam deflection [162] or polarization-dependent changes in optical reflection [163]. Sensors relying on interferometric methods are, for example, based on π -shifted Fiber-Bragg gratings [164], micro-ring resonators [165, 166] or Fabry-Pérot (FP) interferometers [97, 155, 167–173]. Advantages of optical ultrasound sensors are their high acoustic sensitivity [174], a broadband frequency response and the possibility to be integrated with other imaging modalities like OCT or fluorescence microscopes [175–179].

FP ultrasound sensors were used in this work. They can have different geometries. Plano-concave FP sensors can be put on fiber tips or planar substrates and have been shown to exhibit high finesse and acoustic sensitivity [97, 155]. However, they cannot be fabricated small enough to detect high-frequency signals. Moreover, a plano-concave FP sensor typically needs to be placed at a fixed location which is disadvantageous for 3D PA image reconstruction because the signal travel time cannot be directly correlated with the signal source depth. Both of these obstacles make them less suitable for OR-PAM applications.

In this project, a planar FP was used instead. Even though planar FP sensors have been primarily used for PAT [175, 176, 180–185], they also offer great potential for OR-PAM applications. Their transparency for excitation light allows them to be placed almost immediately adjacent to the PA signal source and therefore ensures a minimal source-detector distance and high acoustic sensitivity. Due to their small active element size (tens of microns), they feature broadband detection and an omnidirectional response [170, 180, 186, 187]. For depth-resolved imaging, the detection beam can be scanned across the sensor. Importantly, by custom-designing the mirror reflectivities, they have the potential be integrated with other microscopy modalities like MPM. Such a combined OR-PAM and MPM system may enable combined functional imaging of the blood and structural imaging of the endothelium. Therefore, an FP sensor that is transparent for excitation wavelengths commonly used in MPM was developed for this project. The working principle of a planar FP sensor is presented in the next section.

4.5.3 The planar Fabry-Perót interferometer as ultrasound sensor for OR-PAM

In principle, the planar FP sensor is an interferometer that consists of two parallel and highly reflective mirrors separated by a polymer spacer (see figure 5.4 in methods section 5.1.2).

Light traversing the sensor will be confined to some degree between the two mirrors. If the light reflected at each mirror surface is in phase (i.e. the condition of resonance is met), the beams constructively interfere with each other and maximum transmission through the sensor occurs. Importantly, the condition of resonance is only met, if the optical path length of the spacer (which depends on the spacer thickness, the refractive index of the spacer material and the angle of the incident light) is an integer multiple of the wavelength of the incident light. If the light reflected at each mirror surface is out of phase, the beams destructively interfere with each other and maximum reflectivity occurs. The reflectance spectrum of a sensor as a function of the incident light wavelength is called the interferometer transfer function (ITF). An example is shown in figure 4.4. It shows sharp peaks of high transmission (called fringes) and almost no transmission in between. The wavelength range between two fringes is called the free spectral range (FSR). The optical phase sensitivity of the sensor has its maximum at the peaks of the first derivative of the ITF (see figure 4.4) which indicate the peak ITF gradient. The steeper the gradient, the higher the sensitivity of the sensor. A measure for this is the finesse, the ratio of the FSR and the FWHM of a fringe. It indicates how sharp the interference rings of the beams reflected at each mirror surface are and can be tuned by, for example, the mirror reflectivity. By increasing the mirror reflectivity, the finesse and therefore the optical phase sensitivity of the sensor can be optimized. However, at very high mirror reflectivities, the beam gets laterally displaced along the cavity away from the point of interrogation (the so-called beam walk-off) which in turn compromises sensitivity [188, 189]. The higher the divergence of the interrogation beam, the graver this effect.

To operate the FP interferometer as an ultrasound sensor, the acoustic signal is converted to a change in the reflected optical power according to the following transduction mechanism. An acoustic wave traversing through the FP sensor changes the optical path length of the spacer both by physically compressing it and by modifying its refractive index [190–192]. As the optical path length of the spacer changes, the spectral position of the ITF fringes also changes slightly. At the optimum bias wavelengths of the (original) ITF, the reflected optical power in- or decreases significantly. By tuning the interrogation laser to the optimum bias, this alteration can be measured

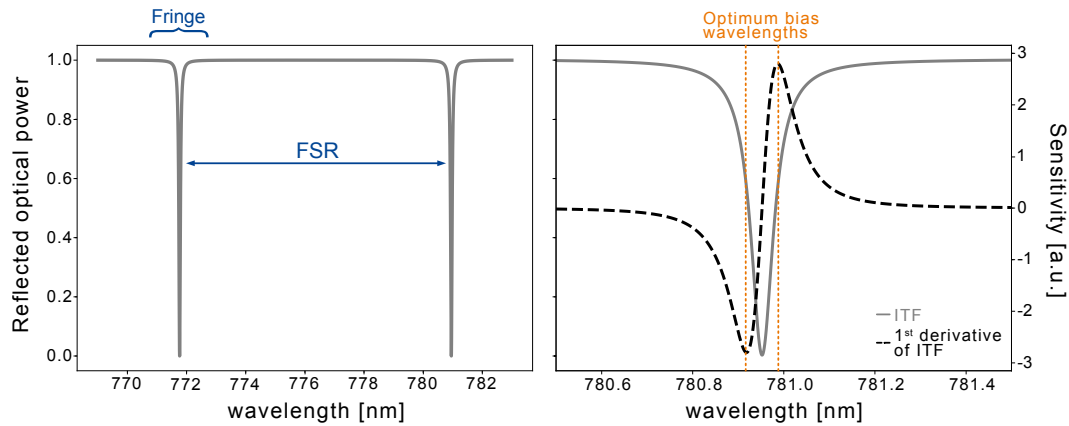


Figure 4.4: Example Interferometer Transfer Function (*Left*) and its first derivative (*Right*). FSR, Free Spectral range; ITF, Interferometer Transfer Function.

as even small changes in the optical path length of the sensor will lead to big changes in the reflected optical power.

On a final note, the active element size of a planar FP sensor is typically diffraction-limited, as the interrogation laser is usually focused into the spacer.

4.6 System requirements

As outlined in this chapter, OR-PAM with a planar FP sensor has the potential to fulfill the aims of objective 1 of my doctoral studies. While previous work often focused on proof-of-principle of the technique, the aim of this project was to construct an OR-PAM system that is tailored to biological applications in the zebrafish trunk vasculature (see part I and in particular the objectives in chapter 3). Therefore, the following requirements for my OR-PAM system based on a planar FP ultrasound sensor emerged:

1. Backward-mode operation which allows for the generation and detection of PA waves on the same side of the sample. With this setup, the distance between PA signal source and detection is minimized which in turn means maximized acoustic sensitivity. Backward-mode is also necessary for most *in vivo* applications where samples are non-transparent and would therefore allow imaging of other model organisms in the future.
2. A lateral resolution of around $10\ \mu\text{m}$ such that single capillaries in the zebrafish trunk vasculature could be resolved.

3. Multiwavelength excitation to enable spectroscopic OR-PAM imaging and the spatially resolved imaging of blood oxygen saturation.
4. High frame-rate scanning to resolve blood flow and allow for the spatially resolved quantification of blood flow.
5. Ultrasound sensing with high acoustic sensitivity to allow for OR-PAM imaging with low fluences. This is especially important for *in vivo* studies because they succumb to maximum permissible exposures for reasons of animal welfare.
6. Broad bandwidth ultrasound detection as small structures generate PA signals with high frequency components which need to be picked up by the detector [156].
7. Integrability with other optical microscopy techniques like multi-photon microscopy (MPM) to enable combined functional imaging of the blood and high-resolution structural imaging of the endothelium.

In the following chapters, I demonstrate that my OR-PAM scanner in fact fulfills the above stated criteria. In chapter 5, I present the setup of the OR-PAM system as it was designed in this work. In chapter 6, I summarize my results and place my work in the context of existing studies. Finally, I draw conclusions from my results and present an outlook in chapter 7.

Methods

5.1 Optical and technical setup of the Optical-Resolution Photoacoustic Microscope

The OR-PAM system developed for this project was based on a multi-wavelength excitation laser system for PA signal generation and a planar optical Fabry-Pérot (FP) sensor for ultrasound detection (Figure 5.1), which are each explained in more detail in the following sections.

5.1.1 Laser systems for multi-wavelength excitation of photoacoustic signals

For conducting spectroscopic PA imaging like measuring the blood oxygenation, at least dual-wavelength excitation is needed (see section 4.4.1). Initially, this was facilitated by using a laser system consisting of two ns-pulsed lasers: a fiber-laser acting as pump laser (532 nm, VGEN-G, Spectra-Physics) and a wavelength-tunable dye laser (570-600 nm, Credo Dye, Sirah). The wavelengths were chosen because of the high absorption of haemoglobin in these ranges (see figure 4.3 in section 4.4.1). The system could be operated at repetition rates ranging from single-shot to 600 kHz. The pulse width could be varied from 3 ns to 20 ns. The excitation beams were coaligned using a dichroic mirror (Thorlabs). For triggering and monitoring the pulse energy, a glass window acting as beam splitter was used to guide part of the pump laser light towards a photodiode (Hamamatsu). To improve the beam quality of the dye laser, it was guided through a spatial filter, i.e. it was focused through a pinhole (30 μm , Thorlabs) with a convex lens ($f = 125$ mm, Thorlabs) and collimated behind the pinhole with a second convex lens ($f = 75$ mm, Thorlabs). Even after spatial filtering, however,

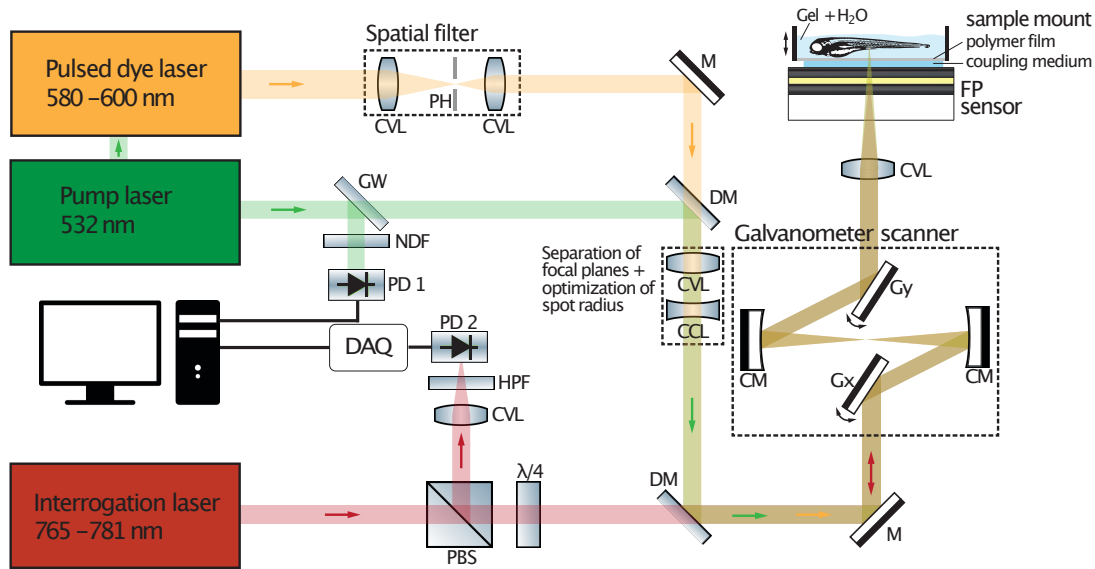


Figure 5.1: Experimental setup of the backward-mode OR-PAM system using a planar Fabry-Pérot (FP) ultrasound sensor.

CCL, Concave Lens; CM, Concave Mirror; CVL, Convex Lens; DAQ, Data Acquisition; DM, Dichroic Mirror; FP, Fabry-Pérot; GW, Glass Window; Gx, X-Galvanometer mirror; Gy, Y-Galvanometer mirror; HPF, High-Pass Filter; M, Mirror; NDF, Neutral Density Filter; PBS, Polarizing Beamsplitter; PD, Photodiode; PH, Pinhole; $\lambda/4$, Quarter-Wave Plate. Created with [193]. Figure adapted from [194].

the dye laser did not exhibit a Gaussian beam profile and the beam quality was not sufficient for spectroscopic imaging. Therefore, the dye laser was replaced by a Raman laser for future work based on this project (Figure 5.2). For this setup, the light of a second fiber laser (532 nm, VGEN-G, Spectra-Physics) was focused into a single-mode polarization-maintaining silicon dioxide (SiO_2) optical fiber (3.3 μm mode field diameter (MFD), 30 m length, Thorlabs). Due to the Raman effect, the emission spectrum at the distal end of the fiber contained so-called Raman lines approximately 14 nm apart. The resulting multi-wavelength output of the fiber is inherently co-aligned and exhibits a Gaussian spatial intensity profile. Since the input polarization determines the intensity of the individual Raman lines, it could be manipulated with a half-wave plate (Thorlabs) before the beam entered the fiber. By rotating the half-wave plate, a wavelength could be preselected to some extent. The better the matching of the polarization of the incoming light and the fiber, the higher the coupling efficiency and the more lines appear. In contrast, if the coupling efficiency is low, less energy will go to higher modes and the first lines have higher intensity. In addition, a bandpass filter

5.1. Optical and technical setup of the Optical-Resolution Photoacoustic Microscope

(Semrock) ensured that only the desired wavelength was used for PA excitation. The light could be collimated using a convex lens, co-aligned with the original pump laser and guided towards the sample just as in the dye laser setup.

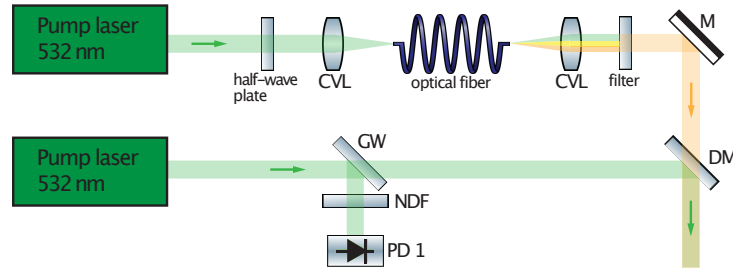


Figure 5.2: Alternative laser system for exciting photoacoustic (PA) signals using a fiber-based Raman laser instead of the pulsed dye laser system.

CVL, Convex Lens; DM, Dichroic Mirror; GW, Glass Window; M, Mirror; NDF, Neutral Density Filter; PD, Photodiode. Created with [193].

5.1.2 Planar Fabry-Pérot ultrasound sensors

The envisioned applications of the OR-PAM system determined the requirements for the used ultrasound sensor (as described in more detail in section 4.5):

- To allow PA signal generation with low excitation pulse energies (which is necessary especially for *in vivo* applications), the sensor needed to have high acoustic sensitivity.
- For high axial resolution, the detector needed to have a broadband bandwidth.
- To allow for an integration of the OR-PAM system with optical microscopy methods such as MPM, the sensor should be transparent for typical MP excitation wavelength ranges.

Conventional piezoelectric ultrasound sensors are readily available but do not fulfill these requirements. Instead of being broadband, they have a resonant frequency response around a center frequency. In addition, they are opaque and therefore need to be placed far away from the PA signal source which compromises acoustic sensitivity. With their broadband frequency response and transparency, optical FP ultrasound sensors can overcome these limitations. For this project, a planar FP interferometer sensor, which is interrogated by a tunable continuous wave (cw) laser in the near-infrared (NIR) regime, was developed. Its design is depicted in figure 5.3. The sensor consists

of a thin polymer (Parylene C) spacer sandwiched by two dielectric mirrors (ZnS and Na_3AlF_6) deposited onto a backing substrate of 10 mm cyclo olefin polymer (COP, figure 5.3A). The dielectric mirrors are designed to be transparent for the excitation light but to reflect the so-called interrogation light. Following the transduction mechanism described in section 4.5.3, the generated acoustic PA signal is translated into an optical signal. Acoustic waves generated by point sources are spherical waves and the encoded information is lost even over short travel distances. They are also susceptible to material boundaries such that a coupling medium like water or ultrasound gel is necessary to avoid impedance mismatches. Optical signals, on the other hand, can travel great distances through air without any information loss.

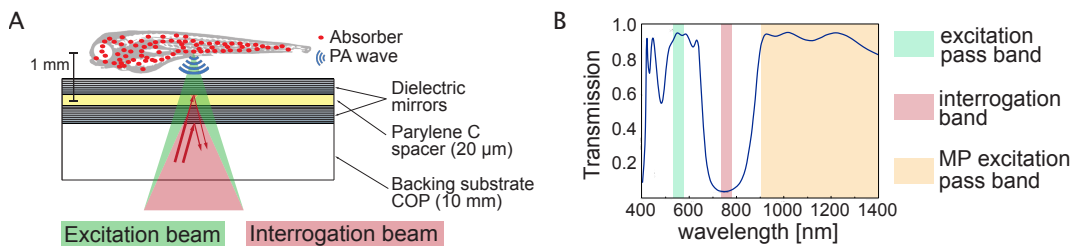


Figure 5.3: Working principle of the FP sensor. **A** Schematic buildup of the FP sensor (adapted from [194]). **B** Reflectance spectrum of the dielectric mirrors of the FP sensor. COP, Cycloolefin polymer; MP, Multi-photon.

Due to its transparency in the PA excitation wavelength range, the FP sensor can be immediately placed adjacent to the signal source and information loss is minimized. This is a great advantage compared to conventional opaque piezoelectric ultrasound sensors. In addition, the mirrors are transparent for wavelengths commonly used to excite hemoglobin with OR-PAM as well as fluorophores with multi-photon microscopy and therefore allow for use in a system combining the two imaging modalities (figure 5.3B).

5.1.3 Photoacoustic signal excitation and acquisition

The excitation and interrogation beams were co-aligned using a dichroic mirror (Thorlabs) to ensure minimal source-detector distance at all times. They were scanned across a predefined field of view (FOV) with a scanner based on two galvanometer mirrors (Nutfield technology) driven by a multifunction I/O device (PXI-6229, National Instruments). To limit aberrations, two concave mirrors were used to relay the beam from the first Galvanometer mirror to the second (figure 5.1). The mirrors ensured

that the beams pivoted around a fixed point on the optical axis (to minimize spherical aberration) and that the focal spot size stayed constant across the entire FOV.

After traveling through the scanner, the laser beams were focused with a convex lens ($f = 50$ mm, Edmund Optics). To ensure an optimal spot radius for signal excitation, a lens combination (a concave lens with $f = 50$ mm and a convex lens with $f = 25$ mm, Edmund Optics) could be placed in the excitation beam path. In addition, the lens combination changed the divergence of the excitation beam such that the focal planes of the excitation and interrogation beams were spatially separated by approximately 1 mm (figure 5.3A). This ensured that the excitation light was focused into the sample but the interrogation light was focused into the FP sensor.

The interrogation light reflected at the sensor was guided towards a detection photodiode (Hamamatsu S5973, 1 GHz). To separate the incident from the reflected interrogation light, a free-space optical circulator consisting of a polarizing beamsplitter (PBS, Thorlabs) and a quarter-wave plate (Thorlabs) was used (figure 5.1). It works as follows: the PBS transmits s-polarized light but reflects p-polarized light. Therefore, only s-polarized light coming from the interrogation source passes through the PBS. Upon passing through the quarter-waveplate, its polarization is rotated by 45° . After being reflected from the FP sensor, the light passes through the quarter-waveplate again such that its polarization is rotated by another 45° . Hence, the initially s-polarized light is now p-polarized. The light beam reflected at the sensor is therefore reflected at the PBS and guided towards the detection photodiode.

The output of both the PA signal detection diode and the trigger pulse diode were recorded using a digital oscilloscope (PXIe-5160, National Instruments).

5.2 Scanning modes

The OR-PAM system can be operated in two different scanning modes: a slow raster-scanning and a fast continuous-scanning mode.

5.2.1 Principle of the raster-scanning mode

In raster-scanning mode, the galvanometer mirrors translated the interrogation and excitation beams across the FOV in a step-like manner as follows: (1) The galvanometer mirrors pointed the co-aligned interrogation and excitation beams to the desired position. (2) The interrogation wavelength was adjusted to the optimum bias at this position to compensate for variations in the FP sensor spacer thickness across the FOV.

(3) A trigger pulse from the excitation laser generated a PA wave in the sample and also initiated (4) the recording of the optical PA signal (i.e. the output of the detection diode). These steps were repeated for all pixels across the predetermined FOV. The time axis of the recorded signals was converted to distance using the known speed of sound in water ($c_s = 1481$ m/s). The advantages of the raster-scanning mode are that (a) several signals measured at the same sensor position can be averaged and (b) the interrogation wavelength can be adjusted to the highest detection sensitivity for each sensor position. However, both the adjustment process of the interrogation wavelength as well as the mechanical stepping of the mirrors (due to their toggling time before reaching a stable position) are time-consuming. As a result, the frame rates achieved in raster-scanning mode were too low to resolve the movement of RBCs to quantify blood flow. It took approximately 40 seconds to scan a FOV of (1×1) mm² with a step size of 4 μ m and a signal averaging of 5 which translates to a frame rate of 0.025 Hz. However, around 20 Hz are necessary to resolve the flow of single RBCs [78].

5.2.2 Principle of the continuous-scanning mode

To overcome this limitation, I implemented a faster continuous-scanning mode based on a method established by my collaborator Thomas Allen [97]. Here, the galvanometer mirrors translated the excitation and interrogation beams continuously across the FOV. Simultaneously, the time traces of the excitation pulses (as recorded by PD 1 in figure 5.1) and the PA signals (as recorded by PD 2 in figure 5.1) were captured continuously. How this is facilitated and how the time stamps of the excitation pulses were matched with the corresponding PA signals to obtain an image is described in more detail in section 5.3. Data streaming was necessary to achieve the required data transfer rates. The used hard- and software limited the maximum sample rate to 50 MS/s per channel. The advantage of the continuous-scanning mode is that the frame rate of the image acquisition is in theory only limited by the pulse repetition rate of the excitation laser. In practice, however, it is also limited by the speed and accuracy of the galvanometer stepping motors. It took approximately 0.6 seconds to scan a FOV of (1×1) mm² and an effective step size of 4 μ m ((250×250) pixels²) using a PRR of 100 kHz. Compared to the raster-scanning mode, the acquisition speed was hence more than 65 times faster. However, at these high pulse repetition rates, the interrogation wavelength could not be tuned to the optimum bias at each sensor position. Instead, it needed to be set to a constant value prior to image acquisition. Therefore, a region of the FP sensor with high spacer thickness homogeneity needed to be selected.

5.3 Control and image reconstruction software

5.3.1 Software for raster-scanning mode

For operating the system in raster-scanning mode, the control software was adapted from an existing package written by my collaborator Edward Zhang in LabVIEW (version 32-bit, 2016, National Instruments (NI)) to be compatible with the designated hardware parts of this setup. The PA signals as output from the image acquisition LabVIEW VI were reconstructed to 2D images using the Matlab toolboxes `pat` (version 2.7, slightly modified) and `k-wave` (version 1.1.1 [63]). 3D volume-rendered images of the same data sets were obtained using the software `Amira` (Thermo Scientific).

5.3.2 Software for continuous-scanning mode

For operating the system in continuous-scanning mode, I needed to establish a different data acquisition software in LabVIEW (version 32-bit, 2016, NI) based on code provided by Thomas Allen. Additionally, I developed a new data processing script to obtain an image from the raw data in Python [195]. An overview of the workflow of both scripts is presented in figure 5.4.

For data acquisition, the software comprised the following three steps. First, the voltages to drive the galvanometer mirrors in the desired scanning pattern were configured (step 1 in figure 5.4A). For the galvanometer mirror in the fast scanning axis, the applied voltage was a triangular function such that the beams were translated along a line. For the galvanometer mirror in the slow-scanning axis, the applied voltage was a step function. The FOV and the number of pixels in x and y determined the effective step size of the scan. For example, for a desired FOV of (1×1) mm² and a number of pixels of 250 in each x and y , the effective step size in each direction amounted to $1 \text{ mm}/250 = 4 \text{ }\mu\text{m}$. The acquisition speed was determined by the PRR of the excitation laser. The higher the PRR, the faster the image acquisition. The speed of the mirror movement was configured such that during a one-line scan, one excitation pulse was shot for each predetermined pixel. For example, for a desired number of pixels of 250 per line and a PRR of 100 kHz (i.e. 10 μs between two pulses), the scan time per line amounted to 2.5 ms.

Second, an excitation pulse was used as trigger to simultaneously start the movement of the galvanometer mirrors and the oscilloscope recording of the two photodiodes, one recording the time trace of the excitation pulses and the other recording the PA signals (step 2 in figure 5.4A). To be able to later reconstruct the image, it was impor-

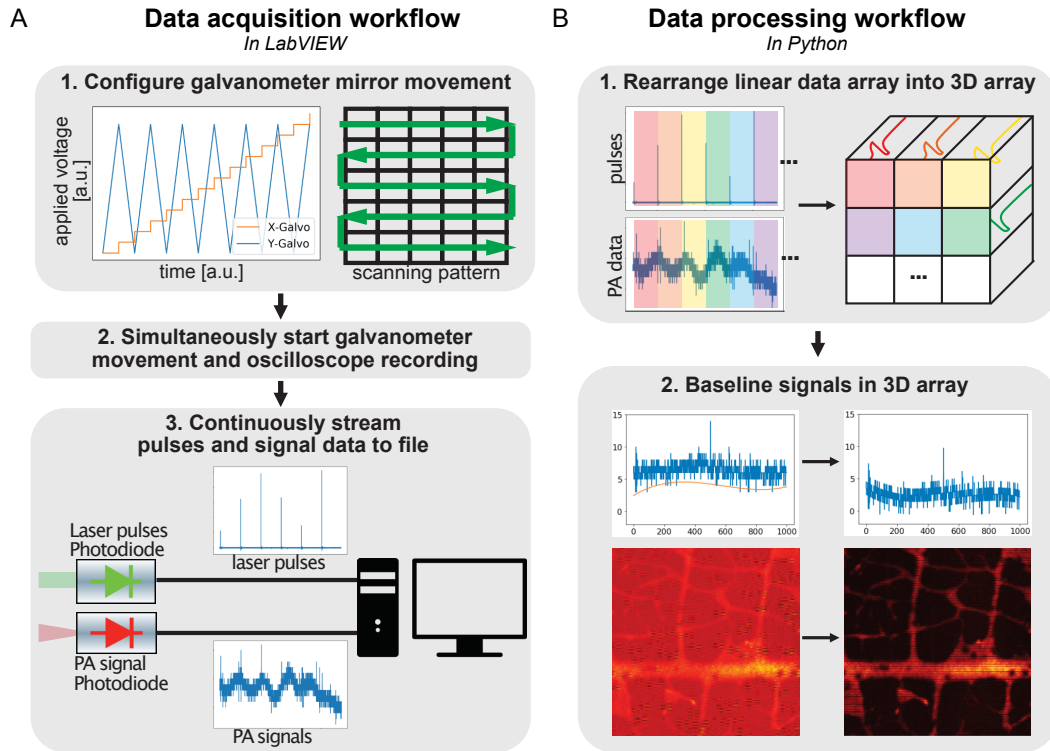


Figure 5.4: Software workflows for the continuous-scanning mode. **A** Data acquisition workflow. **B** Data processing workflow.

tant to synchronize the start of the scanning and the recording. This way the mirror position could later be matched to the corresponding excitation pulse and PA signal.

Third, data streaming was used to continuously write the data detected from the two photodiodes to file (step 3 in figure 5.4A). For performance reasons, the NI file format “Technical Data Management Streaming” (TDMS) was used. Besides the speed advantage compared to other file formats, the TDMS format automatically saves descriptive additional information of the recording (like e.g. the sample rate). However, due to the hardware and software architecture, the data streaming was limited to 50 MS/s. The result of the recording was a TDMS file with two linear arrays: one containing the time trace of the excitation pulses and the other the time trace of the PA signals.

In order to reconstruct the data sets into an image, I wrote a data processing script in Python (figure 5.4B). First, I initialized an empty 3D matrix as a proxy for an x - y - t image data set. The x - and y -dimensions were defined by the number of pixels (typically 250 or 500) for the predefined FOV. The t -dimension depended on the expected

number of sample points between two excitation pulses and was therefore determined by the PRR of the excitation laser and the data streaming rate. For example, at the maximum data streaming rate of 50 MS/s, the t -dimension was 1000 sample points for a PRR of 50 kHz and 500 sample points for a PRR of 100 kHz. Then, I used the time traces of the excitation pulses to chunk up the PA signal data and match the signals with the corresponding pixel and index in the 3D matrix (step 1 in figure 5.4B). Finally, I baselined the signals and, in order to extract the positive part of the signal amplitude, applied a Hilbert transform to them (step 2 in figure 5.4B). As a result, the matrix contained the 3D image data set. For 2D representation, a maximum intensity projection (MIP) was created.

5.4 Experimental work

5.4.1 Fabry-Pérot sensor characterization

To assess the quality of the FP sensor, three characteristics were determined: the bandwidth, the ITF and the spacer homogeneity (see section 4.5 for more theoretical details). The bandwidth was obtained by modeling the acoustic frequency response as described in [196]. In the model, the appropriate densities and speeds of sound were used to account for the backing substrate (COP), spacer material (Parylene C) and coupling medium (water) of the FP sensor (table 5.1, data from [197, 198]). The materials of the mirrors are not considered as they are very thin and assumed to have similar acoustic impedance compared to the surrounding materials.

Table 5.1: Input parameters for modeling of the acoustic frequency response of the FP sensor.

Material	Density [g/cm ³]	Speed of sound [m/s]
COP	1.010	2520
Parylene C	1.289	2200
Water	1.000	1500

The sensor ITF was obtained by measuring the reflected optical power at several different sensor locations over the entire interrogation band (765 nm - 781 nm, step size of 0.05 nm, power of interrogation laser 100 mW). A Voigt function was fitted to the fringe region of each ITF. The FWHMs of the fits were averaged to estimate the fringe width of the sensor.

The spacer homogeneity was qualitatively assessed by checking the optical power

reflected by the sensor over a FOV of (6×6) mm² at a certain interrogation wavelength. Spacer inhomogeneities appeared as regions of low intensity.

5.4.2 Image acquisitions

Unless otherwise specified, all imaging samples were placed on top of the FP sensor with decalcified water functioning as acoustic coupling medium.

Determining the lateral resolution of the system

The lateral resolution of the system was determined in both the raster- and the continuous-scanning modes. In raster-scanning mode, an approach as described in [199] was used. A sharp edge of a piece of gold foil served as resolution target. The gold foil was highly absorbent of the excitation light such that it could be assessed how well the edge was resolved in the image. The edge was imaged at 532 nm across a FOV of (1×1) mm² with a step size of 2 μ m. To obtain the edge-spread function (ESF), a Boltzmann function was fitted to line profiles taken across the edge. The line-spread function (LSF) was obtained by taking the first derivative of the ESF fit. A Gaussian function was fitted to the LSF of which the full-width at half-maximum (FWHM) was determined. The FWHMs of several fits from different line profiles were averaged to get the estimation of the lateral resolution.

To determine the resolution in continuous-scanning mode, a negative United States Air Force (USAF) resolution target was used. A section of the target of (1×1) mm² was imaged at 532 nm and a PRR of 50 kHz with an effective step size of 2 μ m. Line profiles were taken across the edges of the target lines. The ESFs and LSFs were then obtained as described above for the raster-scanning mode.

OR-PAM of leaf skeleton phantoms

To test the morphological and structural imaging capabilities of the system, a black leaf skeleton phantom was used. PA signals were excited either at 532 nm (using the pump laser) or at 590 nm (using the dye laser) at a PRR of 10 or 20 kHz.

For images taken in raster-scanning mode, a pretuning of the FP was obtained prior to the acquisition in order to obtain a map of the optimum interrogation wavelength across the desired FOV. During acquisition, this map was used to tune the interrogation wavelength to optimum bias at each sensor position. Mirror step sizes were typically 5 μ m or 10 μ m and PA signals were averaged 5 times. For a FOV of (3×3) mm², the image acquisition time amounted to approximately 15 minutes.

For images taken in continuous-scanning mode, a sensor location with high spacer homogeneity across the desired FOV was chosen prior to acquisition. PA images were obtained at 532 nm, with a PRR of 50 kHz or 100 kHz and without signal averaging. The effective step size was typically 4 μm (e.g. for a FOV of $(2 \times 2) \text{ mm}^2$ with 500×500 pixels²). For a FOV of $(2 \times 2) \text{ mm}^2$, the image acquisition time was 2.5 s per frame at a PRR of 50 kHz.

The signal-to-noise ratio (SNR) in the images was determined using

$$SNR = \frac{A_{signal}}{\sigma_{noise}}, \quad (5.1)$$

with the signal amplitude A_{signal} and the standard deviation of the noise σ_{noise} . A_{signal} was averaged over several signals. σ_{noise} was determined from the peak-to-peak noise (PPN) with $PPN = 6 \cdot \sigma_{noise}$ [155].

OR-PAM of ink phantoms

Ink phantoms were imaged to demonstrate the multi-wavelength excitation capabilities of the system. Red ink ("Rohrers Antiktusche Krapprot", Rohrer & Klingner Leipzig-Co) was used to imitate oxygenated blood and blue ink ("Rohrers Antiktusche Blauviolett", Rohrer & Klingner Leipzig-Co) was used to imitate deoxygenated blood. Three tetrafluoroethylene hexafluoropropylene and vinylidene fluoride (THV) polymer tubes (inner diameter 333 μm , outer diameter 400 μm) were filled with red ink, blue ink and a 1:1 mixture, respectively, and imaged together at 532 nm, 570 nm, 580 nm, 590 nm, and 600 nm over a FOV of 500 $\mu\text{m} \times 1.5 \text{ mm}$. Image intensities were corrected by subtracting the respective background intensity (as measured in regions of the image with no signal). To quantify how light absorption of the inks changes for different excitation wavelengths, PA signal amplitudes were averaged across regions of interest (ROIs) of the parts of the image containing each ink sample. Across images obtained at different excitation wavelength, the same ROIs were used. For comparison, the absorption spectra of ink dilutions were also obtained using a photospectrometer (NanoDrop 2000, Thermo Scientific).

***In vivo* OR-PAM of zebrafish embryos**

Zebrafish growing, breeding and handling were performed according to the animal welfare regulations by the MDC as approved by the local authorities (LaGeSo). All procedures adhered with FELASA guidelines [200]. No additional animal licence was required as all fish were younger than 5 days post fertilization (dpf). Zebrafish embryos of the wildtype strain AB/TL (4 dpf) were imaged. They were anesthetized with 0.014% tricaine (Tricaine-Pharmaq, 1000 mg/g, PHARMAQ Limited). For mounting, they were embedded into low melting point agarose gel (Invitrogen) containing 0.014% tricaine, which was placed onto clear plastic foil held by a round mechanical mount (Thorlabs). For imaging, the mount was placed approximately 1 mm above the FP sensor using a combination of mechanical translation stages. Images were acquired in raster-scanning mode. PA signals were excited with 532 nm at a PRR of 20 kHz across a FOV of (1.2×3.8) mm² and with a step-size of 8 μ m. PA signals were averaged up to 20 times. Total acquisition time amounted to 17 minutes per image.

Results and Discussion

A novel OR-PAM system based on a planar Fabry-Pérot (FP) ultrasound sensor was designed for this project. In the following paragraphs, I present the results obtained with the system, highlight advantages, set out limitations, compare to other systems and show evidence that it in fact fulfills the requirements set by the envisaged imaging applications as described in section 4.6.

6.1 System characterization

In this paragraph, I describe the advantages of the optical design and assess the performance of my OR-PAM system.

The optical design (shown in figure 5.1 and described in section 5.1) comprises several advantages. First, aligning the signal excitation and sensor interrogation laser beams guaranteed minimized source-detector distances, and therefore maximized acoustic sensitivity, across the entire FOV. Second, the focal planes of the interrogation and excitation lasers were separated, such that the interrogation light was focused into the sensor spacer but the excitation light was focused into the sample. Since the focal spot size of the excitation laser was the limiting factor for spatial resolution, the focal plane separation ensured maximum spatial resolution. The specifications of the lens combination facilitating the separation were obtained using optical ray tracing simulations (performed by my collaborators). Finally, to limit spherical aberrations, the galvanometer mirrors were paired with two concave mirrors such that the scanned beam pivoted around one point on the second galvanometer mirror. This resulted in FOVs of up to 30 mm^2 which is more than 10 times larger than in a previously reported system [201].

The performance of the system was characterized by (1) assessing the bandwidth and interferometer transfer function (ITF) of the FP ultrasound sensor and (2) by determining the spatial resolution.

6.1.1 Characterization of the Fabry-Pérot sensor

Planar FP ultrasound sensors with an interrogation band in the NIR regime were fabricated for this work (see section 4.5.3 for the working principle of the FP sensor and section 5.1.2 for the design). Their characterization is presented in figure 6.1.

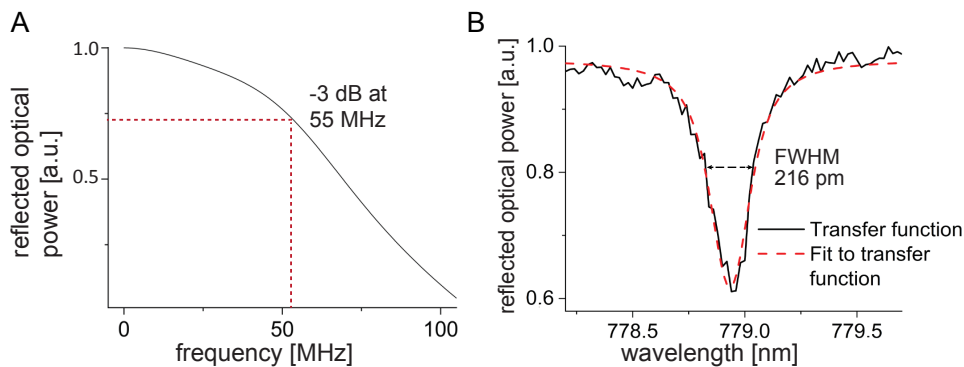


Figure 6.1: Characterization of the planar Fabry-Pérot (FP) ultrasound sensor [194]. **A** Simulated frequency response of the sensor shows a broad bandwidth with the -3 dB at 55 MHz. **B** Resonance of a typical interferometer transfer function (ITF) of an FP sensor with a full-width at half-maximum (FWHM) of 216 pm.

In contrast to conventional piezoelectric sensors (which exhibit a resonant bell-shape frequency response around a center frequency), using a forward analytical model to obtain the frequency response of the FP sensor [180, 196] found it to be uniform up to the -3 dB value of 55 MHz (figure 6.1A, the input parameters of the model are summarized in table 5.1 in section 5.4.1). A spacer thickness of 20 μm was assumed for modeling, as this was the thickness of FP sensors used to obtain the images presented in this thesis. For smaller spacer thicknesses, however, the bandwidth could be broadened further. For example, FP sensors with a spacer thickness of 5 μm are expected to have a uniform frequency response up to 200 MHz. This is desirable because RBCs have been reported to generate PA signals with high frequency components beyond 150 MHz [156]. It should be noted, however, that the broadened bandwidth comes at the expense of acoustic sensitivity. Nevertheless, sensors with 5 μm were tested for this project and found to be sensitive enough for imaging (see figure A.1 in the appendix). Further

development of these sensors holds great potential for future research with applications in vascular biology.

A typical ITF of the FP sensors with 20 μm spacers is shown in figure 6.1B. The average FWHM was found to be (336 ± 120) pm (\pm standard error, $n = 7$). The free spectral range (FSR) was approximately 8 nm. Taken together, these values result in a finesse $F = FSR/FWHM$ of around 25 (with a maximum value of 40 for fringes with a FWHM down to 200 pm).

The results for the FP sensor compare well with previous studies. The system that is most similar to mine was reported by Hajireza et al. [201] who also used a planar FP sensor for OR-PAM. However, in my work, the design exhibits several distinct advancements. First, with the interrogation band in the NIR range, the mirrors of the FP sensors I used are transparent for wavelengths longer than 900 nm, which are commonly used for two-photon excitation (see figure 5.3B in section 5.1). This allows for their integration in a combined OR-PAM and multi-photon microscopy system, an important feature to reach the goal of simultaneous functional imaging of the blood and morphological imaging of the endothelium. Moreover, it will make OR-PAM accessible to other applications in the field of vascular biology. Second, the sensors reported in this work had a higher mirror reflectivity which positively impacts acoustic sensitivity, yielding a maximum finesse of 40. Hajireza et al. do not report the finesse of their sensor but estimating the FWHM of the fringes from their ITF to be around 10 nm yields a finesse of 4. It is reasonable to assume that a 10-fold increase in finesse results in higher optical phase sensitivity and therefore also higher acoustic sensitivity. Third, the frequency response of the sensor I used shows a broadband detection bandwidth of up to 55 MHz (with the clear potential to increase it even further for smaller spacer thicknesses), compared to 18 MHz reported by Hajireza et al. Finally, the optical thickness of the sensor I used is homogenous over a FOV of several mm^2 (figure 6.6) compared to FOVs of (600×400) μm^2 reported by Hajireza et al.

In conclusion, the FP sensor developed for this work is an improvement compared to previously reported designs and meets a number of criteria (1, 5, 6, and 7) of the OR-PAM system requirements as described in section 4.6. Because of its transparency to excitation light, it allows backward-mode OR-PAM (criterion 1) with maximized acoustic sensitivity (criterion 5). As becomes evident from figure 6.1A, it also offers broad bandwidth detection (criterion 6) which is important for resolving small structures like RBCs. Due to its mirror design, the FP sensor is suitable for an imaging platform combining OR-PAM with MPM (criterion 7).

6.1.2 Spatial resolution

The spatial resolution of an imaging modality is divided into the lateral resolution (in the x - y -plane) and the axial or vertical resolution (along the z -axis). I also consider these two separately here.

The desired lateral resolution of the OR-PAM system for vascular biology is dictated by the width of ISVs in the zebrafish trunk which is around 10 μm , and the size of a single RBC which is around 7-8 μm [202]. To assess smearing or other artefacts that could be the result of high scanning speeds, the lateral resolution of the system was determined separately for the raster- and continuous-scanning modes according to the methods described in section 5.4.2. The results are presented in figure 6.2. In raster-scanning mode, the lateral resolution was found to be (8.1 ± 1.4) μm (\pm standard error, $n = 3$, figure 6.2A). The maximum resolution was 6.5 μm . This result is in good agreement with the theoretical diffraction-limited spot size of 6.6 μm of the achromatic doublet that was used for focusing the excitation light into the sample. Since the edge of the gold foil target was curved, it was only possible to obtain the ESF along a thin line across the edge (green line in the left inset in figure 6.2A). This resulted in an uneven intensity profile, which is disadvantageous for fitting the Boltzmann function. To overcome this limitation, the lateral resolution in the continuous-scanning mode was determined using a standardized USAF resolution target. Here, the intensity profile could be integrated across a bigger area along an edge such that the intensity profile was smooth (green area in figure 6.2B). The lateral resolution was found to be (11.8 ± 1.7) μm ($n = 8$, figure 6.2B) with a maximum resolution of 9.4 μm .

There are several possibilities that could explain the decrease in lateral resolution in the continuous-scanning mode compared to the raster-scanning mode. First, since the galvanometer mirrors continue to move for the duration of the excitation pulse, smearing of the excitation focal spot could be expected at high frame rates. However, at a fast optical scanning axis of 1 kHz (like e.g. for a frame rate of 20 frames per second (fps), a FOV of (250×250) μm^2 and 100 scan lines), the focal spot moved only by 5 nm during a 10 ns excitation pulse. Hence, smearing does not seem likely to be the cause of the decreased resolution. Another explanation could be a stretching effect that may originate from the galvanometer mirrors not following the theoretically predetermined voltages in the continuous-scanning mode, especially at the reversal points, i.e. the end of each line scan, where the applied triangular voltages require a sharp change in direction. Such a sharp direction change is not trivially facilitated by a mechanical step motor. However, using the USAF resolution target with its well defined target element

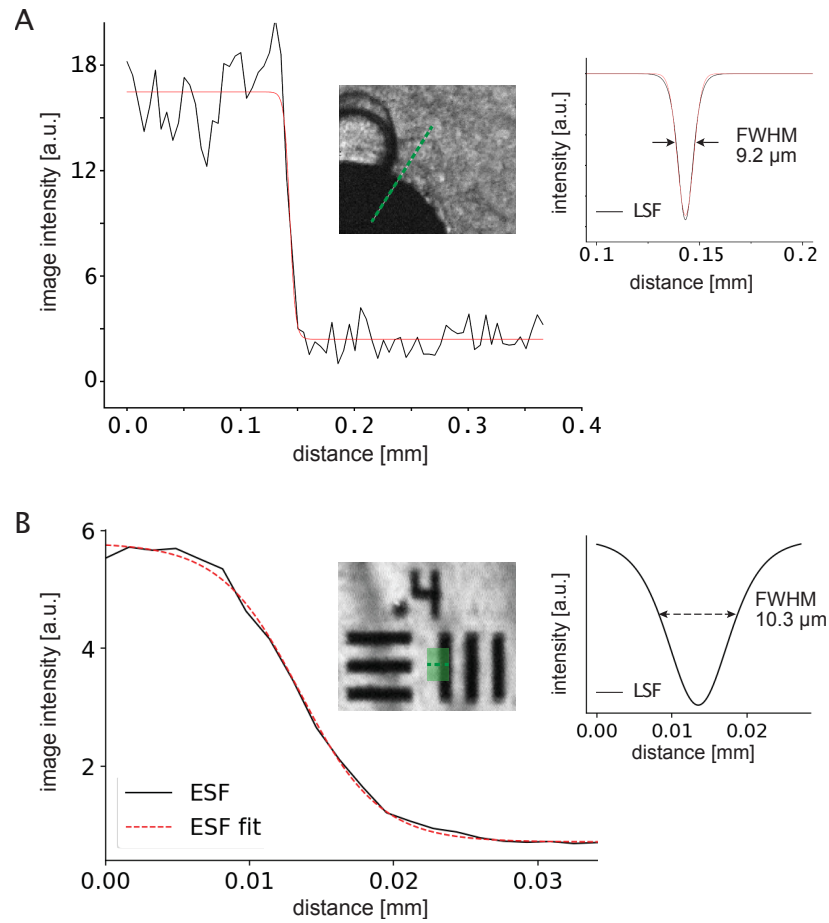


Figure 6.2: Measurements of the lateral resolution of the system. **A** Lateral resolution of the system as determined in the raster-scanning mode. An image intensity profile was taken across a 2D image of a sharp edge of gold foil (edge-spread function (ESF)). To estimate the resolution, the full-width at half-maximum (FWHM) of the first derivative of the ESF, i.e. the line-spread function (LSF), was determined. **B** Spatial resolution of the system as determined in the continuous-scanning mode [194]. The same protocol as for the raster-scanning mode was followed but using an USAF resolution target instead of gold foil.

sizes, I verified that no stretching occurred at the margins of an image. Edge blurring of the elements is also unlikely to be the cause of the discrepancy as the resolution target is fabricated using photolithography and the edge sharpness is specified as around 1 μm by the manufacturer. Finally, the two lateral resolutions were in fact obtained with two different setups, in two different labs and with different targets resulting in limited comparability of the values. While the value for the raster-scanning mode was

measured with the setup at MLU Halle, the value for the continuous-scanning mode was measured with the setup at the MDC in Berlin. Importantly, for the MDC setup, the focal planes of the interrogation laser and excitation laser were not yet separated when the resolution was determined. Since the Rayleigh length of the excitation beam is expected to be around 150 μm , it was likely focused below the target such that the resolution was in fact not determined using the minimum focal spot size.

In general, the focal spot size is limiting the lateral resolution. Numerical simulations using ray tracing techniques conducted by my collaborators (TH Wildau) suggest that the spot size can be readily reduced further by changing the divergence of the excitation laser. The simulations determined that by adding a combination of a concave and a convex lens to the excitation path beam (see dashed box "optimization of spot radius" in figure 5.1 in chapter 5), a focal spot size of as low as 1 μm is possible across the entire FOV. Optimal optical alignment of these additional lenses would be difficult in practice, but even a geometrical focal spot size of 3 μm would represent a significant improvement in spatial resolution.

The vertical resolution (i.e. the resolution along the z-axis) of the system also differed for the two scanning modes. In raster-scanning mode, it was limited by the excitation pulse width and the bandwidth of the detector. For an excitation pulse width of 10 ns, the vertical resolution amounted to 15 μm (as the speed of sound in water is approximately 1500 m/s). Since the pulse width of the used excitation laser can be set to as low as 3 ns, much higher vertical resolutions are possible. However, an increase in bandwidth of the FP sensor would be required. For a spacer thickness of 10 μm , the bandwidth would increase from the current approximately 50 MHz (for a spacer thickness of 20 μm) to 100 MHz resulting in a vertical resolution limit of 8 μm . In continuous-scanning mode, the vertical resolution was limited by the maximum data sampling frequency of 50 MS/s of the streaming hardware, and hence a vertical resolution of 30 μm . However, as hardware systems with better streaming performance are readily available, this value does not constitute a fundamental limitation.

In conclusion, the spatial resolution in both scanning modes is already sufficient for the envisioned applications such that criterion 2 of the system requirements as described in section 4.6 is fulfilled. Especially the lateral resolution can, however, be readily improved even further by optimizing the divergence of the excitation lasers. To allow a meaningful comparison of the resolutions in raster- and continuous-scanning mode, the measurements need to be performed again in the same OR-PAM system after finalization of the optical setup (i.e. after inclusion of the Raman laser, see below).

6.2 *In vitro* raster-scanning OR-PAM of phantoms

6.2.1 Morphological OR-PAM

The morphological imaging capabilities of the OR-PAM system were demonstrated by imaging a black leaf skeleton at an excitation wavelength of 532 nm in raster-scanning mode (figure 6.3). Due to the coaxial alignment of the interrogation and excitation beams and the high vertical resolution of the system, depth information was retrieved (see xz - and yz -image planes in figure 6.3A). This is also evident from the resolved curvature and contours of the leaf in a volume-rendered 3D representation of the data set shown in figure 6.3B. Additionally, the co-alignment of the beams also ensures optimal acoustic sensitivity at all times.

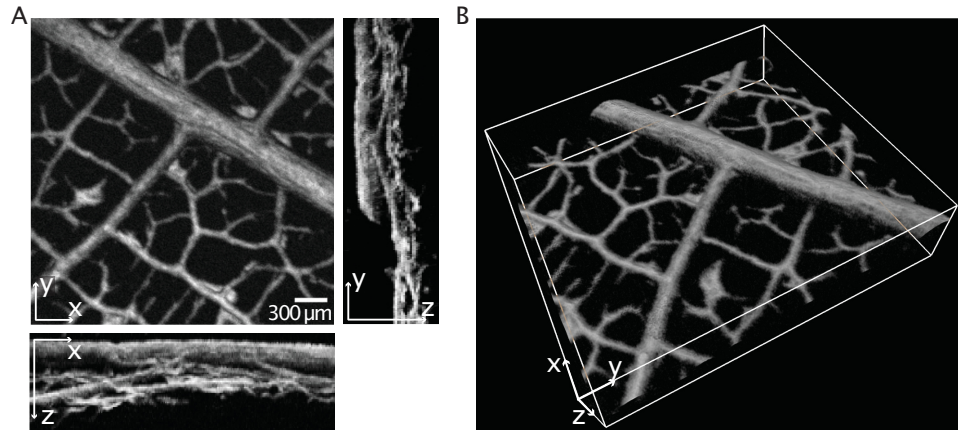


Figure 6.3: OR-PAM image of a leaf skeleton phantom acquired in raster-scanning mode at an excitation wavelength of 532 nm [194]. **A** Maximum intensity projections (MIP) of the image. For better visibility of depth-resolved structures, the image was stretched by a factor of two in the z -plane. **B** Volume-rendered image of the same data set.

For all reported image acquisitions including this one, the typical pulse energy amounted to 40 nJ which translated to an estimated fluence of 100 mJ/cm². This value is well below the exposure safety limit for *in vivo* imaging and also lower than the fluences reported for other *in vivo* PAM applications [97, 167, 179, 203].

6.2.2 Multi-wavelength OR-PAM

To obtain spatially resolved images of the blood oxygen saturation, the relative concentrations of deoxygenated and oxygenated hemoglobin need to be determined. This

requires spectroscopic OR-PAM imaging with at least dual-wavelength excitation (see section 4.4.1). To demonstrate that spectroscopic imaging is technically possible with the designed OR-PAM setup, several phantoms were imaged at different excitation wavelengths in raster-scanning mode: (1) a leaf skeleton phantom was imaged at 532 nm and 590 nm, and (2) ink phantoms resembling oxygenated and deoxygenated blood were imaged at five excitation wavelengths ranging from 532 nm to 600 nm.

The images of the leaf skeleton phantom are presented in figure 6.4. In both images, the same structures are resolved. However, the lateral resolution as well as the SNR were lower in the image obtained with the dye laser at 590 nm compared to the image obtained with the fiber laser at 532 nm. This was caused by the beam parameters of the multimodal dye laser. The quality of a laser beam is quantified using the parameter M^2 which denotes the deviation of the beam profile from an ideal Gaussian distribution. The closer M^2 is to 1 for a given beam, the smaller the deviation from an ideal Gaussian and the better its focusability. The green fiber laser had a close-to-ideal circular Gaussian beam profile ($M^2 = 1.1$). In contrast, M^2 of the dye laser was not provided by the manufacturer but found to be >20 even after spatial filtering when measuring the beam waist radius and divergence. The dye laser also had an elliptical rather than a circular, Gaussian-like beam profile. In general, the pinhole size of 30 μm of the spatial filter limited the focal spot size as for higher pinhole sizes, M^2 increases. However, for smaller pinholes (which would result in improved M^2 values), the laser power after filtering was insufficient for OR-PAM. Taking all these observations together, it could be concluded that the beam quality of the dye laser did not suffice for OR-PAM. To overcome these constraints, a Raman fiber laser was constructed to replace the dye laser for future applications that require multi-wavelength excitation (as outlined in

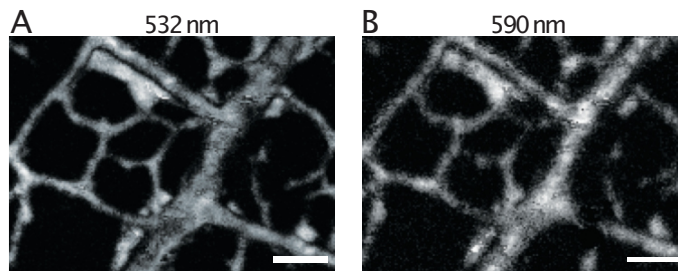


Figure 6.4: Comparison of OR-PAM images of a leaf skeleton phantom obtained at different excitation wavelengths in raster-scanning mode [194]. **A** OR-PAM image obtained at 532 nm. **B** OR-PAM image obtained at 590 nm which showed lower contrast than the image in A due to poorer beam quality of the dye laser. Scale bar: 300 μm .

methods section 5.1.1). The spectral lines were found to have sufficient pulse energy to perform OR-PAM (see figure A.2 in the appendix). Due to its design based on an optical fiber, all wavelengths exiting the Raman laser are intrinsically co-aligned and exhibit a Gaussian beam profile. It has also previously been shown that Raman lasers are suitable for OR-PAM imaging [201, 204].

OR-PAM images of an ink phantom resembling blood at different stages of oxygenation are presented in figure 6.5. Three different inks were used to simulate the optical properties of blood: red ink represented oxygenated blood, blue ink represented deoxygenated blood and a 1:1 mixture of the two represented mixed blood. Qualitatively, differences in the image intensity can be seen¹.

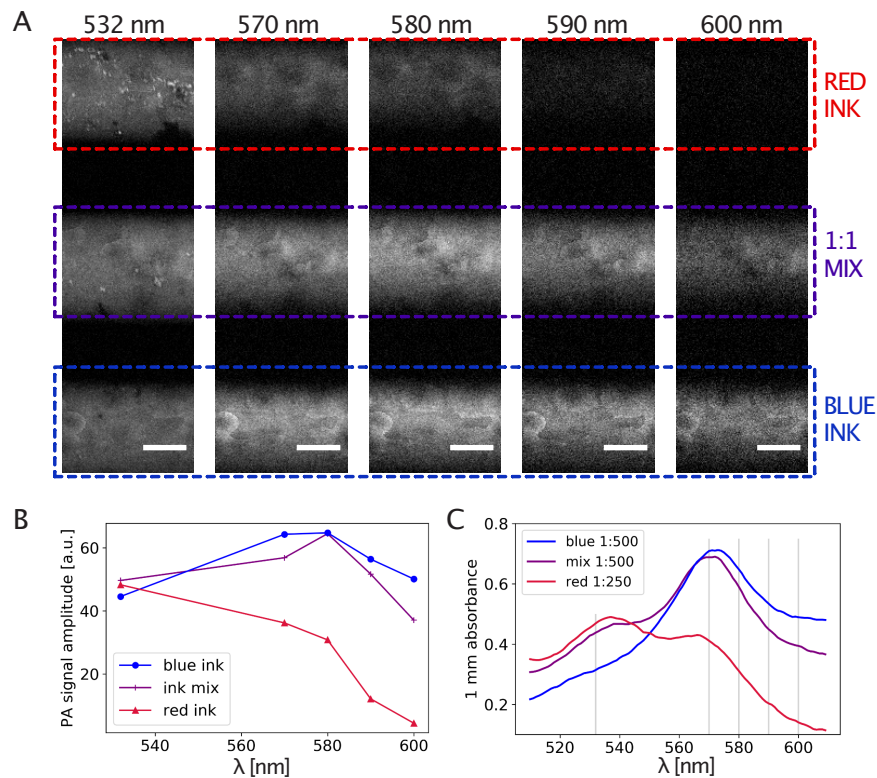


Figure 6.5: OR-PAM images of ink phantoms simulating blood acquired at five different excitation wavelengths in raster-scanning mode. **A** MIPs of OR-PAM images of red ink, mixed ink and blue ink phantoms. **B** Averaged PA amplitudes of the images presented in A. **C** Absorption spectra of ink dilutions obtained with a photospectrometer for comparison. Scale bar: 200 μm .

¹The uneven structures seen in the images were caused by defects in the FP sensor spacer.

A quantitative assessment of these differences was achieved by comparing the averaged PA signal amplitudes. For the red ink, the PA signal amplitude gradually decreased as the excitation wavelength increased (figure 6.5A and B). At 600 nm, almost no signal was detected. For the blue ink, the PA signal amplitudes increased from 532 nm to 570 nm. It then decreased for higher excitation wavelengths but much less than the signal of the red ink. The PA signal amplitudes of the ink mixture showed a similar pattern as the blue ink but with a more pronounced decrease for high excitation wavelengths. Overall, the PA signal amplitudes of all ink phantoms followed similar trends as seen in the absorption spectra of ink dilutions measured with a photospectrometer (figure 6.5C). It needs to be noted, however, that the blue ink was so absorbent that it needed to be diluted by a factor of two more compared to the red ink when measuring the absorption spectra (1:500 vs. 1:250). This difference was not reflected in the PA signal amplitudes. One reason for this could be that the highly-concentrated inks generate PA signals with predominantly high-frequency components which are not detected by the bandwidth-limited FP sensor. Moreover, the inks are likely non-linear absorbers which could also explain this behavior. For quantitative validations of the spectroscopic imaging capabilities of the system, established linear absorbers like India ink [205, 206] or copper/nickel sulfate [207] should be used in the future. In addition, the PA signals should be normalized for pulse energy for accurate spectroscopic measurements. This can be achieved by recording the pulses with an additional photodiode. Finally, chromatic aberrations (different refraction of different wavelengths in the lens material) could also explain the deviations but were limited by using an achromatic lens for focusing.

In conclusion, while multiwavelength excitation and backward-mode detection using the OR-PAM setup were shown to capture the absorption spectra of dye mixtures in a qualitative manner, its capabilities for functional imaging are currently limited by the poor beam quality of the dye laser. This obstacle can be readily overcome by exchanging the dye laser for a Raman laser. Raman laser integration into the OR-PAM setup will enable high-resolution spectroscopic imaging of the blood oxygenation such that the setup will meet criterion 3 of the system requirements as outlined in section 4.6. For quantitative validations, phantoms containing established linear absorbers should be used.

6.2.3 Continuous-scanning OR-PAM

The continuous-scanning performance of the OR-PAM system, which was implemented to resolve blood flow in future applications, was tested on a leaf skeleton phantom (figure 6.6). To facilitate quantitative imaging of blood flow in the zebrafish, imaging frame rates of at least 20 Hz are necessary [78]. For a FOV of $(2 \times 2) \text{ mm}^2$ ((500×500) pixels² which translates to an effective step size of $4 \mu\text{m}$) and a PRR of 100 kHz, a frame rate of 0.4 Hz was achieved. For the desired FOV of $(200 \times 300) \mu\text{m}^2$, which is typically used to image the zebrafish trunk, 20 Hz and more are therefore possible when operating the fast scanning galvanometer mirror at 1 kHz. While this scanning rate is non-trivial for mechanical galvanometers, similar and even higher rates using galvanometer scanners have been reported [97, 208]. However, many other OR-PAM setups quantifying spatially resolved blood flow do not, in fact, acquire images at video-

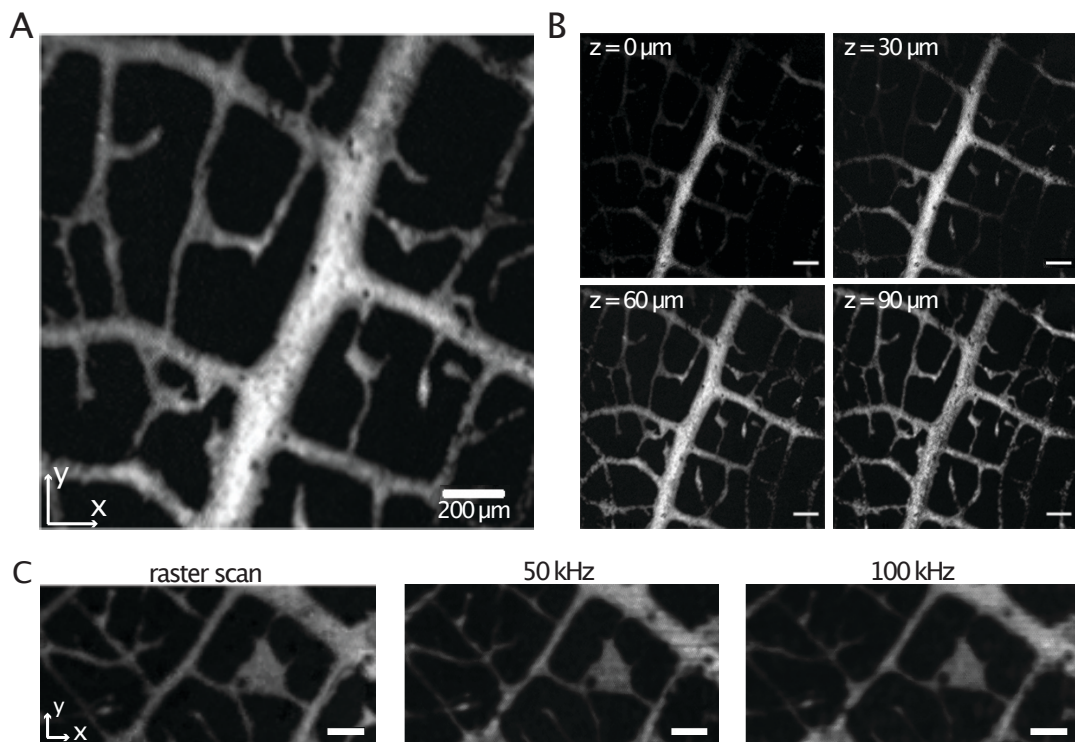


Figure 6.6: OR-PAM image of a leaf skeleton phantom obtained in continuous-scanning mode [194]. **A** MIP of the Hilbert transform of the PA signals **B** z-slices at different depths of the data set shown in **A**. **C** Comparison of images acquired in raster-scanning mode, at a PRR of 50 kHz, and at 100 kHz in continuous-scanning mode. Scale bars: 200 μm .

rate [127, 150, 151, 153, 154, 209]. They can still quantify the bulk blood flow but the imaging speeds are not high enough to resolve flow of single RBCs (for which, as mentioned above, frame rates of 20 Hz are necessary [78]). These approaches are also prone to movement artefacts, caused for example by respiration, and have limited functionality for high flow speeds. On the other hand, they cover much larger FOVs of up to 15 mm² and are therefore more suitable for applications for which this is necessary (e.g. imaging the microvasculature around a tumor or the brain in mammal animal models like the mouse).

Another advantage of the OR-PAM system operated in continuous-scanning mode is that, similar to the images obtained in raster-scanning mode, depth information was directly retrieved due to the co-alignment of the interrogation and excitation beams. This is evidenced by the slices obtained at different z -positions (figure 6.6B). However, the vertical resolution was limited to 30 μm by the maximum sampling rate of the used acquisition hardware (as discussed in more detail in the context of assessing the vertical resolution in section 6.1.2).

Images obtained in continuous-scanning mode at a PRR of 50 kHz and 100 kHz, respectively, showed similar image quality compared to images obtained in raster-scanning mode (figure 6.6C). The same structures were resolved in all three images. However, the SNR was reduced by a factor of two in continuous-scanning mode. For the raster-scan it was 128, for the 50 kHz image it was 58 and for the 100 kHz image it was 54. The reduced contrast in the continuous-scanning mode was expected as the interrogation wavelength needed to be fixed. Hence, it could not be tuned to the optimum bias for each position on the sensor. Furthermore, PA signals could not be averaged. Nevertheless, even the reduced SNR was sufficient for imaging.

The dark regions that can be seen in the images resulted from inhomogeneities of the spacer thickness, which reduce the acoustic sensitivity of the sensor. Since a change in spacer thickness requires a correction of the interrogation wavelength to achieve optimum bias, but a fixed wavelength can only interrogate a reduced number of points, no PA signal was detected in these areas. The inhomogeneities were likely caused by contaminations during the manufacturing process and limitations of the thin film deposition device. When a dust particle lands on the substrate before or during spacer deposition, dome-like layers are subsequently deposited over it leading to the variance in spacer thickness. By improving the fabrication process, the homogeneity of the optical thickness could be improved resulting in uniform sensitivity across the entire FOV. Nevertheless, the sensors already showed sufficient homogeneity for the FOVs required for the envisioned applications (around (200x300) μm^2 for the zebrafish trunk). The

acoustic sensitivity of the sensor could also be further increased by optimizing the mirror reflectivity and the spacer material.

In order to properly reconstruct images from the data sets obtained in continuous-scanning mode, one major obstacle became the process of matching the obtained PA signals with the correct galvanometer positions. To gain full knowledge of the galvanometer positions at all times, an additional time trace of the galvanometer voltages would need to be recorded for each image acquisition. However, this could not be facilitated in the current setup since the oscilloscope did not have additional free channels. Therefore, the theoretically applied voltages to generate the desired scan pattern were used as a proxy for the galvanometer positions. However, these introduced a systematic, reproducible offset in the image reconstruction that was distinct for each unique set of scanning parameters (combination of desired FOV and PRR). Most likely, there was a discrepancy between the predetermined and the actual galvanometer position. For smaller FOVs and higher PRR (i.e. for higher scanning speeds), the offset could not be easily rectified. Further development of the data acquisition and processing pipelines is necessary to overcome this issue. As a first step, the galvanometer mirror voltages should be recorded (independent of the image acquisition) and compared to the theoretical ones. In case the voltages are reproducible for different acquisitions with the same scanning parameters (which seems likely as the offset is also reproducible), they could be used for position matching. Another option would be to use software packages like ScanImage instead of in-house software that have built-in solutions for this issue [210]. Finally, a definite solution to the problem could be the use of an oscilloscope with two additional channels which would allow the recording of the galvanometer voltages for each image acquisition. The downside would be the size increase of the recorded data set by a factor of two. Instead of saving the complete time series, another option would be to only save the time stamps of the reversal points of the fast scanning galvanometer. This would produce a minor increase in additional data points but would be an effective way to match the PA signal data stream and the line scans.

In conclusion, the potential of the setup to reach image acquisition frame rates of more than 20 Hz to resolve flow of single RBCs, and therefore to fulfill criterion 4 in the list of system requirements presented in section 4.6, has been demonstrated. It was shown that future improvements of the image acquisition software and/or hardware can be readily implemented to fully exploit that potential for the intended imaging applications.

6.3 *In vivo* OR-PAM of zebrafish

To demonstrate the *in vivo* imaging capabilities of the system, an initial experiment using a live zebrafish embryo was conducted (figure 6.7). Anatomical features like the eyes, the yolk sac, the heart, trunk and tail were resolved in both the 2D and the 3D representation of the data set (figure 6.7A and B). A bright-field image is shown for comparison (figure 6.7C).

While hemoglobin likely contributed to the image contrast, the absorption of mela-

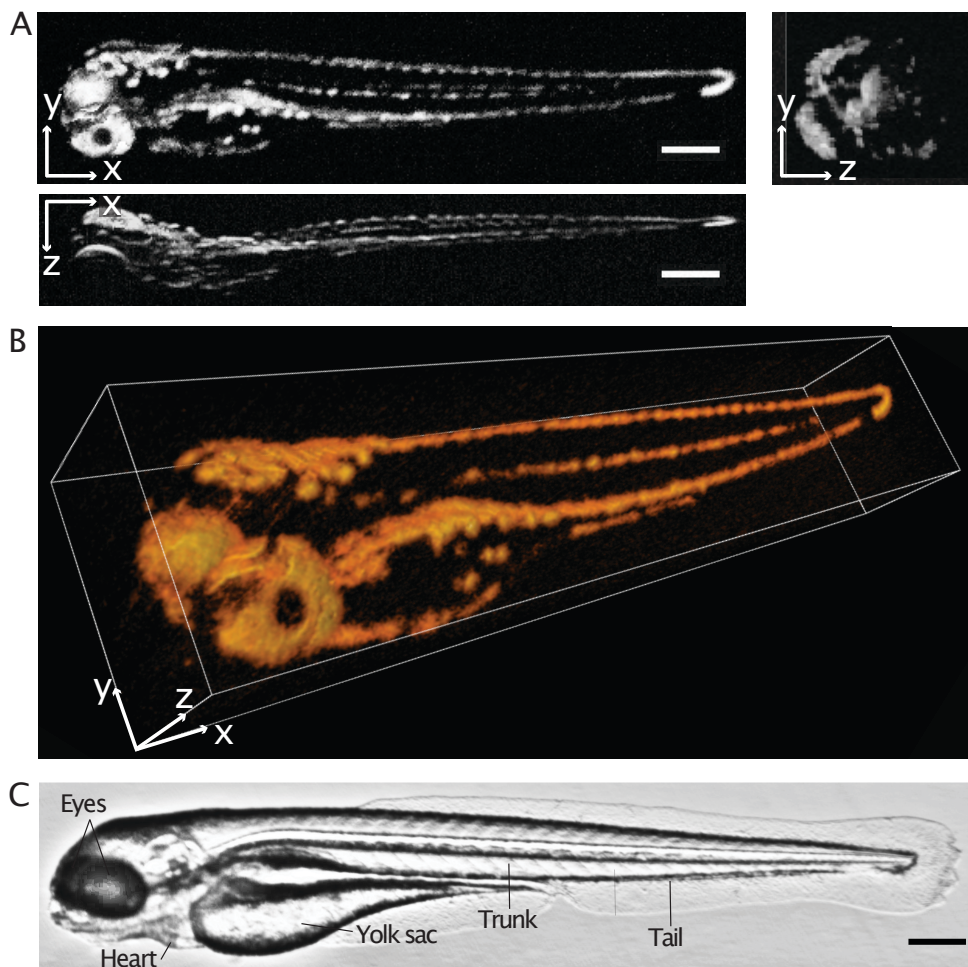


Figure 6.7: *In vivo* OR-PAM image of a zebrafish embryo (4 dpf) acquired in raster-scanning mode [194]. **A** MIPs of the image. **B** Volume-rendered image of the same data set shown in A. **C** Zebrafish anatomy in a bright-field microscopy image for reference. Scale bars: 300 μm .

nin is higher at 532 nm and also dominant in the image. To suppress melanin expression, the embryos can be treated with 1-phenyl 2-thiourea (PTU) prior to imaging in future experiments.

Since the ISVs in the zebrafish trunk are only several micrometer wide, correct positioning of the sample in the focal plane is crucial for resolving them. In contrast to other studies, that have successfully performed OR-PAM in the zebrafish trunk vasculature at approximately the same developmental stage as used here [177, 211], this could not be achieved with the necessary precision in this system. The difficulty is that there is no eyepiece to move the sample into the focus position as used in all-optical microscopes. To overcome this limitation, the focus would need to move through the sample such that an image can be taken at different depth positions, similar to a z-stack. A focus tunable lens (FTL) could not facilitate this, as optical simulations revealed that the minimal voltage increase of conventional FTLs is already bigger than the typical thickness of an ISV. Instead, using a mechanical translation stage to move the sample through the focal plane would be a suitable and cost-effective way to solve this issue. In that case, adjustment of the image acquisition software to include controlling of the translation stage would be necessary.

Conclusions and Outlook

In this work, a backward-mode OR-PAM system with a planar FP ultrasound sensor was developed. A set of technical capabilities were defined against which the new system was compared. It was found to meet the requirements for functional OR-PAM of the zebrafish trunk vasculature: high spatial resolution, high acoustic sensitivity, as well as capabilities to image blood oxygenation and blood flow. For high-resolution *in vivo* imaging, the FP sensor features highly advantageous attributes, such as a broadband frequency response, high finesse and high acoustic sensitivity due to minimal source-detector distances. In addition, the system provides multi-wavelength excitation for spectroscopic OR-PAM to enable quantitative imaging of blood oxygenation. To potentially resolve blood flow of single RBCs, a fast image acquisition mode (termed continuous-scanning mode) was established which exploits the high spacer thickness homogeneity of the FP sensor over several mm². The potential of the fast imaging mode to reach video-rate scanning speeds >20 Hz for FOVs typically used in the zebrafish trunk was demonstrated. In general, the depth-resolved imaging capabilities of the system were validated in phantoms and *in vivo* in zebrafish.

Compared to other systems, the reported OR-PAM scanner has a number of advantages. By pairing the galvanometer mirrors with two concave mirrors in the scanner, I could limit spherical aberrations and achieve high FOVs up to 30 mm². The planar FP sensor provides higher finesse and higher spacer homogeneity than previously reported ones [201]. Moreover, by co-aligning the PA excitation and sensor interrogation laser beams as well as separating their focal planes, I could minimize PA signal loss but maximize spatial resolution and acoustic sensitivity. As a result, low pulse energies of 40 nJ were sufficient to generate images without signal averaging. Finally, due to the FP sensor's mirror design, the system allows integration with other optical imaging

techniques like MPM. This feature makes it suitable for many applications in vascular biology that require simultaneous backward-mode imaging of hemodynamics and endothelial dynamics (examples of which are listed further below).

Some minor adjustments of the system will allow for its imaging potential to fully unfold. For high-resolution spectroscopic OR-PAM of RBCs (to quantify blood oxygenation), a Raman laser will replace the currently used dye laser for reasons of better beam quality. Additional lenses will provide an even tighter excitation focal spot. A reduced spacer thickness of the FP sensor will increase the bandwidth even further yielding optimized detection of high-frequency components of PA signals generated by RBCs. To improve the vertical resolution and enable direct 3D image acquisition in the continuous-scanning mode, the hardware should be equipped with data acquisition cards with higher data sampling rates. Moreover, the fast image acquisition software needs to be adjusted to properly match PA signals and scanner position for high scanning rates. Finally, to resolve the thin ISVs in the zebrafish trunk, the setup will benefit from z -focussing, i.e. an acquisition mode that takes several images while moving the excitation focus along the vertical axis of the sample.

Due to the FP sensor's transparency for wavelengths in the visible range of the optical spectrum and above 900 nm, the OR-PAM system allows integration with other optical imaging modalities relying on high excitation wavelengths like MPM. Such a combined system would offer perfect functionality for combined *in vivo* imaging of hemodynamics and endothelial dynamics in the zebrafish. With OR-PAM, the blood flow speeds and oxygenation could be quantified for the entire trunk vasculature. With MPM, the response of the endothelium to the prevailing conditions could be observed with single-cell resolution. The controlled change of flow and oxygenation (e.g. by the administration of certain drugs or by means of laser ablation) would allow the identification of thresholds of flow speeds or oxygenation that induce a certain EC behavior. Combined with the genetic deletion of certain genes, these studies would have the potential to unravel key pathways of EC flow and oxygenation sensing yielding not only significant insights into vascular development and remodeling but also paving the way for the identification of novel therapeutic targets treating a variety of diseases characterized by disrupted vessel growth.

This work also paves the way for other exciting future work, both in terms of technology and applications. In terms of technology, the galvanometer-based scanner could be replaced, for example, by acousto-optic modulators (AOM) for stable beam steering at even higher scanning rates. An AO tunable filter (AOTF) could also be used to quickly switch between different excitation wavelengths. In fact, spectroscopic

information (i.e. oxygenation) could be obtained in a single scan by quickly changing between excitation wavelengths of the same source or setting a certain delay between separate laser outputs. In this setup, it would be possible to observe how oxygen is released from a single flowing RBC. This is of great topical relevance as it has been speculated that in certain Long Covid conditions the blood is indeed sufficiently oxygenated but fails to properly release the oxygen for tissue supply which leads to symptoms like chronic fatigue.

The list of other possible applications for both vascular development and disease models is endless. Since the system operates in backward-mode, it is not restricted to the use of the transparent zebrafish but also allows the imaging of other animal models like mice. For example, hemodynamics and endothelial dynamics in the mouse brain could be simultaneously studied by adding a FP ultrasound sensor to a cranial window. This development would open up yet new ways to study healthy vascular development in the brain as well as vascular development associated with brain cancers like glioblastoma.

In summary, this transdisciplinary work comprises a significant contribution both to the technological development in the field of photoacoustic imaging and enabling new imaging applications in the field of vascular biology. It opens up the possibility for a microscopy modality that combines OR-PAM, for functional imaging of the blood, and MPM, for single-cell resolution imaging of the endothelium, to illuminate the role of blood flow and oxygenation in vascular remodeling.

PART III

Computational image analysis
method to study endothelial
dynamics and its defects in the
developing mouse retina

Abstract and contribution

The developing mouse retina is a well-established model system to study vascular network patterning. One of its big advantages is that different stages of vascular remodeling (active sprouting, pruning, quiescence) can be observed at the same time. However, live imaging of the retina with single-cell resolution is not possible with most conventional optical microscopy modalities due to its spherical geometry. Therefore, static imaging is usually used which means that inferring information about endothelial cell (EC) migration principles from retina images is difficult. The aim of this project was to overcome this limitation by using a lineage tracing approach and establishing a novel computational image analysis method to quantify the spatial-temporal distribution of ECs in the retina. By labeling a subset of ECs at a given time point and analyzing the spatial distribution of ECs with respect to the vasculature at several later time points, conclusions about EC dynamics from static images could be drawn. The capabilities of the method were demonstrated by showing differences between the dynamics of wild-type ECs and ECs that were homozygous knockouts of the Rho GTPases Cdc42 and Rac1. In particular, while the distribution of wild-type ECs shifted from veins to arteries over time, the population of Cdc42-depleted ECs failed to do so, identifying Cdc42 as an essential protein for EC migration against flow.

The work presented in this part as well as similar figures are included in the following preprint:

- Wolfgang Giese*, André Rosa*, **Elisabeth Baumann**, Olya Oppenheim, Emir Bora Akmeriç, Santiago Andrade, Irene Hollfinger, Silvanus Alt, and Holger Gerhardt. Reconstructing stochastic cell population trajectories reveals regulators and heterogeneity of endothelial flow-migration coupling driving vascular remodelling. *bioRxiv*, 2023.

For this project, I worked closely together with the postdocs André Rosa and Wolfgang

Giese, and the technician Irene Hollfanger from the iVBL, MDC, Berlin under the supervision of Prof. Holger Gerhardt. André Rosa was responsible for the conceptualization of the project and together with Irene Hollfanger performed all mouse experiments (breeding, injections, imaging). Together with André Rosa, I manually annotated the retina vasculature in each image. In addition, I implemented the computational image analysis method supported by Wolfgang Giese. We shared responsibility for scripting the analysis code which was based on work performed by Silvanus Alt, a former postdoc in the lab. In particular, I was responsible for developing the code for the 2D kernel density function and verification of the input data. For the manuscript, I created the figures presenting the results of the analysis, helped with manuscript writing and code clean-up.

For a collaboration with Dr. Yi Jin and Prof. Dr. Lena Claesson-Welsh from Uppsala University, Uppsala, Sweden, the 2D distribution analysis method as described in this thesis was used to analyze the population shift of ECs depleted of the tyrosine kinase Yes1 (data not shown). The analysis helped to unravel that Yes1 controls collective endothelial migration. *Yes1* inducible, EC specific knockout cells migrated faster from veins to arteries than control ECs and by P15, they were almost exclusively found in arteries. These findings were part of the publication:

- Yi Jin, Yindi Ding, Mark Richards, Mika Kaakinen, Wolfgang Giese, **Elisabeth Baumann**, Anna Szymborska, André Rosa, Sofia Nordling, Lilian Schimmel, Emir Bora Akmeriç, Andreia Pena, Emmanuel Nwadozi, Maria Jamalpour, Katrin Holstein, Miguel Sáinz-Jaspeado, Miguel O. Bernabeu, Michael Welsh, Emma Gordon, Claudio A. Franco, Dietmar Vestweber, Lauri Eklund, Holger Gerhardt and Lena Claesson-Welsh. Tyrosine-protein kinase Yes controls endothelial junctional plasticity and barrier integrity by regulating VE-cadherin phosphorylation and endocytosis. *Nature Cardiovascular Research*, 1:1156–1173, 2022.

I contributed to this work by performing the 2D distribution analysis on the images of control and *Yes1* KO retinas, creating figure panels, preparing the corresponding raw data for publishing and proof-reading the manuscript.

Introduction

The importance of EC migration for vascular growth and vascular network patterning is illustrated in detail in chapter 1 of this thesis. Briefly, ECs respond to VEGF signals emitted from cells in hypoxic environments through sprouting angiogenesis - a process involving orchestrated EC proliferation and migration that leads to the vascularization of previously avascular tissues [5]. In recent years, combined efforts have unraveled many key molecular mechanisms of angiogenesis, first and foremost the VEGF and Notch signaling pathways [13, 16–19, 212]. This research led to the development and clinical approval of several pro- and anti-angiogenic drugs, mostly targeting VEGF receptors, for the treatment of pathologies like ischemia or cancer. The efficacy of these drugs, however, has been limited [5, 8].

In addition to the cell-signaling induced migration, ECs also respond to mechanical stimuli from the wall shear stress (WSS) evoked on the endothelium by blood flow. It has been shown *in vivo* that ECs migrate from regions of low WSS to regions of high WSS [28–30]. This remodeling process is essential to obtain a properly functioning hierarchical vascular network. Many endothelial mechanosensors and -transducers have been identified, but due to the complex interplay between them, it is difficult to decipher a specific signaling pathway. Therefore, the exact means of endothelial flow sensing remain elusive. Unraveling the underlying mechanisms of both EC migration following biochemical cues and EC migration following mechanical cues will pave the way for the identification of new therapeutic targets for many pathologies characterized by disrupted angiogenesis or vascular network patterning defects.

To further identify the signaling pathways regulating EC migration, preclinical imaging plays an important role as it allows for direct observation of the response of the endothelium to different external stimuli. The developing mouse retina is a useful

model system to simultaneously study the vasculature in all its remodeling phases, and thus permits the observation of EC migration induced by both VEGF (in the sprouting front) and WSS (in the remodeling plexus) at the same time (described in more detail in chapter 2 of this thesis). Despite the widespread use of the mouse retina as a model system in vascular biology, image analysis is mostly non-automated and often relies on the description of phenotypes concerning vascular morphology [39, 213, 214]. Automated machine learning methods for the segmentation of the vasculature have been developed, but they also mainly target vessel morphology [215–218]. Therefore, different methods are needed to reach the ultimate goal of identifying key players for EC migration in response to VEGF or flow. The challenge here is that vascular network patterning is a dynamic process that occurs over days or weeks [41], but imaging of the retina is typically done *ex vivo*, capturing only one specific time point. This makes it impossible to follow individual cells over time. These experimental limitations can be overcome by novel imaging and computational image analysis methods aimed at the quantification of EC migration in the developing mouse retina. This demand is two-fold: on the one hand, blood flow and WSS in the retina need to be quantified. On the other hand, EC migration needs to be quantified with high spatial and temporal resolution.

Several studies have recently been published in this regard. For example, to overcome the limitation that blood flow cannot be imaged directly, Bernabeu and colleagues developed a computational tool simulating the complex hemodynamic forces (WSS and flow velocity) in a segmented retina leaf [219]. They integrated this computational method in the image analysis tool PolNet, which quantifies EC polarization angles, with the intention of combining the simulations of flow with a quantification of the direction of EC migration [24, 31, 220]. EC polarization (in this case meaning the positioning of the Golgi apparatus with respect to the nucleus of a cell) is considered a proxy for the direction of EC migration [24]. PolNet is, therefore, a powerful image analysis tool but needs to be combined with other methods to extract dynamic information regarding EC migration from static retina images. Barbacena et al. recently reported another approach for quantitative analysis of EC polarisation [221]. They used a principal component analysis of several morphological features of the vasculature (e.g. vessel density and number of branching points) to identify a vascular transition zone between the sprouting front and the remodeling plexus. They found that in mature arteries in the remodeling plexus, EC polarisation points towards the optic nerve. In contrast, EC polarisation flips in the transition zone, such that it points towards the periphery of the retina in the sprouting front. This suggests opposing and competing forces for EC

migration resulting from the VEGF and WSS gradients. They could also show that the transition zone shifts if VEGF levels or blood flow are manipulated. However, their method does not lead to any explicit conclusions about directed EC migration or how it is affected by the manipulations.

Lineage-tracing experiments provide a complementary approach to the above-mentioned methods. For lineage-tracing, a subpopulation of ECs is labeled with a fluorescent marker at a specific time point. By collecting and imaging retinas at a later time point (or a series of later time points), the shift of the spatial distribution of the labeled EC population- resulting from migration, but also proliferation- can be observed. Recently, Lee et al. used lineage-tracing of ECs expressing GFP under a newly identified vein-specific promoter to show that venous ECs are the main EC type participating in angiogenesis and migration against flow, as well as the main contributor in AVM formation [222]. For the expansion of the vasculature in general, and arteriogenesis in particular, venous ECs actively migrate from veins to the sprouting front, as well as across the remodeling plexus into arteries. Their findings suggest that targeting the venous endothelium specifically might be a promising strategy for treatment of many vascular diseases. However, what is still lacking is a quantitative assessment of the EC population shift. This is invaluable because only the quantification of EC migration- and importantly, of EC migration defects induced by the controlled absence of certain proteins- will ultimately lead to the identification of the driving mechanisms of EC migration and vascular pathogenesis.

In this project, I have sought to fill this gap by introducing a novel 2D distribution image analysis method, which I developed together with colleagues. We took an analytical approach using a general coordinate system representing a map of the vasculature of a retina. By reading off the positions of GFP-positive ECs on this map at different time points after labeling, we could trace the 2D population distribution shift over time and space. Our method works to elucidate the role of certain proteins for EC migration even if the initial stochastic recombination was not specific to a certain vessel type; as we have recently shown in a collaborative project for the tyrosine-protein kinase Yes1 [223]. In the study presented in this thesis, I demonstrated the potential of the method by identifying EC migration defects after conditionally knocking out *Cell division control protein 42 homolog (Cdc42)* (which is upregulated in the absence of Yes1 [223]) and *Ras-related C3 botulinum toxin substrate 1 (Rac1)* in labeled ECs. Cdc42 and Rac1 belong to the protein family of Ras homologue GTPases (Rho GTPases) that are involved in the regulation of many dynamic cellular processes. They are known to play a role in both individual migration (of a single cell in contact with an extracellular matrix),

and for collective migration (groups of cells that maintain junctional integrity between each other during migration) by controlling the rearrangement of the actin cytoskeleton that is required for directed forward migration. Active Cdc42 and Rac1 localize at the leading front of the migrating cell, and regulate the formation of membrane protrusions [224]. In particular, Cdc42 is associated with the formation of filopodia [225]. *In vitro*, its role for EC migration [226, 227] and polarization [228] has been demonstrated. *In vivo*, its deletion results in embryonic lethality [229] or, if deleted after initial lumen formation, in vascular patterning defects both in the developing mouse retina [230] and the brain [231]. Rac1, on the other hand, is associated with the formation of lamellipodia. *In vivo*, its deletion also results in embryonic lethality [232].

Using the 2D distribution analysis, I could show that Cdc42 is essential for ECs to reach the artery. However, Cdc42-depleted ECs still seem to be able to migrate following VEGF signals by moving into the sprouting front. Furthermore, I could show that the deletion of Rac1 only caused minor migration defects. The main acceleration of migration was delayed compared to control ECs. Taken together, I show that the analysis method can quantify EC migration in static images of the remodeling retina and, importantly, also picks up migration defects in ECs with the loss-of-function of certain genes. This development opens up the way to further unravel pathomechanisms in vascular diseases, and identify targets for selective therapies.

Methods

In this chapter, I describe the computational image analysis method to extract quantitative information on EC migration from static images of the developing mouse retina, which I implemented supported by Wolfgang Giese (section 9.2). In order to understand the reasoning of this analysis, however, it is necessary to first understand the mouse and imaging work, which was performed by my colleagues André Rosa and Irene Hollfanger. I am limiting the description of their work in section 9.1 to as much detail as is necessary to explain the motivation of the project as basis for the image analysis.

9.1 Mouse work

All animal experiments were approved by the local authorities (LaGeSo, animal licence G0207/18, 14/11/2018). Taking a lineage tracing approach, three fluorescent reporter mouse lines were used for this project (figure 9.1A) [233–236]:

- control:
 $Gt(ROSA)26Sor^{tm4(ACTB-tdTomato,-EGFP)}Luo/J; Vegfr3CreER^{T2}$
- *Cdc42* inducible, endothelial cell specific knockout (iECKO):
 $Cdc42^{tm1}Brak; Gt(ROSA)26Sor^{tm4(ACTB-tdTomato,-EGFP)}Luo/J; Vegfr3CreER^{T2}$
- *Rac1* iECKO:
 $Rac1^{tm1}Brak; Gt(ROSA)26Sor^{tm4(ACTB-tdTomato,-EGFP)}Luo/J; Vegfr3CreER^{T2}$

All strains were based on an inducible Cre-loxP recombination system (which is described in detail elsewhere [233]) under a Vascular endothelial growth factor receptor

9. METHODS

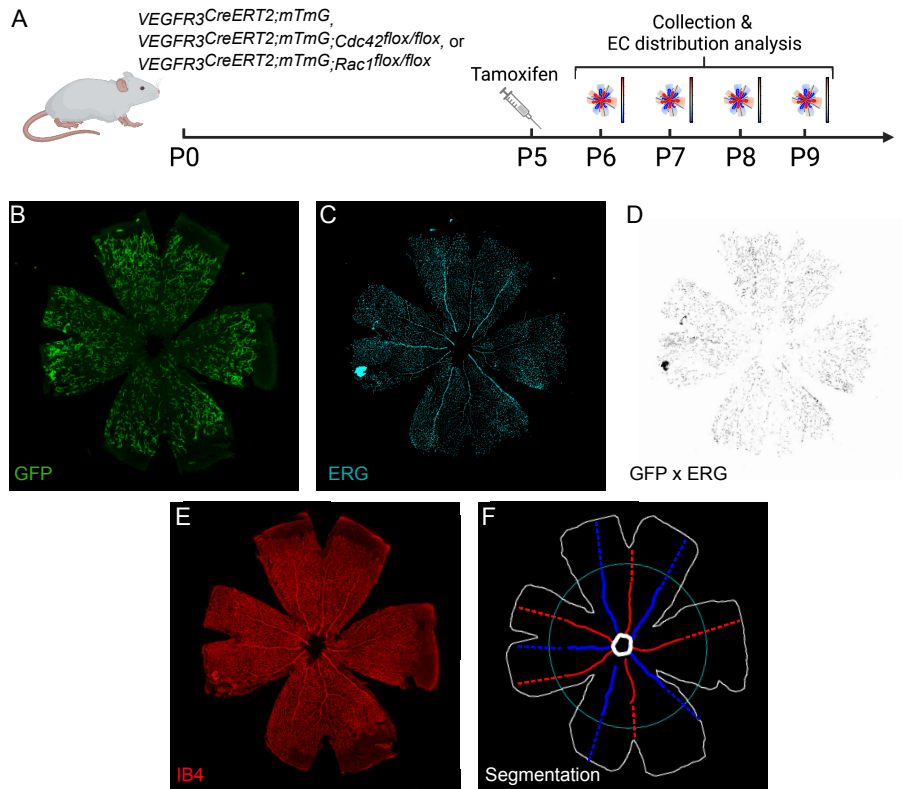


Figure 9.1: Mouse work for the EC distribution analysis. **A** Injection scheme. **B-F** Acquired image channels of an example retina. **B** GFP signal of labeled ECs. **C** ERG staining showing EC nuclei. **D** Image multiplication of GFP and ERG channels that was used for analysis in order to normalize for EC cell size. **E** IB4 staining showing the entire vasculature that was used for manual annotation. **F** Manual annotation of the retina that was based on the IB4 staining: optic nerve (thick white), mature arteries (red), mature veins (blue), line to separate sprouting front and remodeling plexus (turquoise). Straight-line extensions of mature vessels (dashed lines) were used for analysis in the sprouting front.

3 (*VEGFR3*) promoter. *VEGFR3* is expressed in ECs in mature veins, capillaries, and the sprouting front but not in mature arteries. Conceptually, the mTmG fluorescent reporter strain works as follows: mTmG is ubiquitous meaning that all cells express the red fluorescent protein mTomato. Upon Cre-recombination, cells express green fluorescent protein (GFP) instead of mTomato. For spatial control, Cre-recombination can only occur in cells expressing *VEGFR3* (i.e. all ECs except for those in mature arteries) as CreERT2 is encoded under a *VEGFR3* promoter. For temporal control, tamoxifen injection is required for cells to undergo Cre-recombination. Therefore, upon

low-dose tamoxifen injection, a randomly distributed fraction of VEGFR3 expressing cells express GFP instead of mTomato. As a result, ECs in veins, capillaries and the sprouting front are mosaically labeled with GFP. In the case of the knockout (KO) mouse strains, the labeled cells were also homozygous KOs of the Rho GTPases Cdc42 or Rac1, respectively. All other, non-recombined background cells, however, were wild-type and therefore the same in all three conditions.

Pups were injected with tamoxifen on postnatal day 5 (P5) labeling a randomly distributed fraction of ECs with GFP in mature veins, the remodeling plexus and the sprouting front but not in mature arteries. Eyes of the injected pups were collected and EC distribution analysis was performed in the retina at four different time points: P6, P7, P8, and P9 (figure 9.1A). Hence, the spatial distribution of GFP-positive ECs was determined one to four days after labeling. This way, information about spatial-temporal EC dynamics could be extracted from static images.

The retinas were dissected, flattened and fixed as described in [237]. To label blood vessel membranes, they were stained for Isolectin 4 (IB4, Invitrogen). To label EC nuclei, they were stained for Erythroblast transformation-specific (ETS)-related gene (ERG, Abcam). Then, they were imaged using a confocal fluorescence microscope (LSM700 or LSM780, Zeiss). Three channels were acquired: (1) GFP-signal of the ECs in which Cre-recombination occurred upon mosaic labeling at P5 (figure 9.1B), (2) ERG signal of all EC nuclei (figure 9.1C), and (3) IB4 signal of the entire vasculature (figure 9.1E). To normalize for EC cell size in the analysis, the GFP image was multiplied with the ERG image (figure 9.1D). For the analysis, main parts of the retina vasculature (optic nerve, mature arteries, mature veins, straight-line extensions of mature vessels, and a line separating sprouting front and remodeling plexus) were manually annotated based on the IB4 staining (figure 9.1F).

9.2 Computational method to extract the spatial distribution of ECs from microscopy images of the developing mouse retina

Overall, the quantitative analysis of the spatial distribution of ECs comprised three steps: (1) annotating different anatomical parts of each retina, (2) creating distance maps of each retina based on the annotations, and (3) reading off the position of GFP-positive ECs with respect to the optic nerve as well as with respect to arteries and veins from these maps. In the following, I will describe each step in more detail.

Manual annotation: Mature veins, mature arteries and the optic nerve were manu-

ally annotated based on the IB4 staining of each retina (figure 9.1F). Since mature vessels are missing in the sprouting front¹, it was decided to analyze the 2D distribution of ECs there separately from the remodeling plexus. Therefore, the annotation included an ellipsoid approximately representing the border between plexus and sprouting front. To be able to also quantify the spatial distribution of ECs with respect to arteries and veins in the sprouting front, I used straight-line extensions of mature arteries and veins in the plexus to separate the retina into areas that were more likely to feed into/from an artery or vein (dashed red and blue lines in figure 9.1F).

Creating distance maps: The annotation masks were used to create distance maps of each retina (figure 9.2).

Each map shows the distance in micrometers of each pixel in the retina image to the nearest positive pixel in the corresponding annotation mask. For example, the map based on the mask of the optic nerve showed the distance to the optic nerve at any location in the retina. Due to the reasons mentioned above, two sets of distance maps were created to separate the analysis of ECs in the remodeling plexus and of ECs in the sprouting front. To analyze the spatial distribution of ECs in the remodeling plexus, the following distance maps were created:

- distance to the optic nerve d_r (figure 9.2C, D)
- distance to the nearest artery d_{ARP} (figure 9.2E, F)
- distance to the nearest vein d_{VRP} (figure 9.2G, H)

To analyze ECs in the sprouting front (where mature vessels are missing), d_{ARP} and d_{VRP} were replaced by the following distance maps:

- distance to straight-line approximations of extended arteries d_{ASF} (figure 9.2I, J)
- distance to straight-line approximations of extended veins d_{VSF} (figure 9.2K, L)

To normalize for different retina sizes, I also generated a set of normalized distance maps according to the following equation:

$$\phi_{V \rightarrow ARP/SF} = \frac{d_{VRP/SF}}{d_{VRP/SF} + d_{ARP/SF}} \quad (9.1)$$

¹I use the term sprouting front for all regions in the retina that have not yet undergone remodeling even if no active sprouting is occurring anymore (which is the case for later time points).

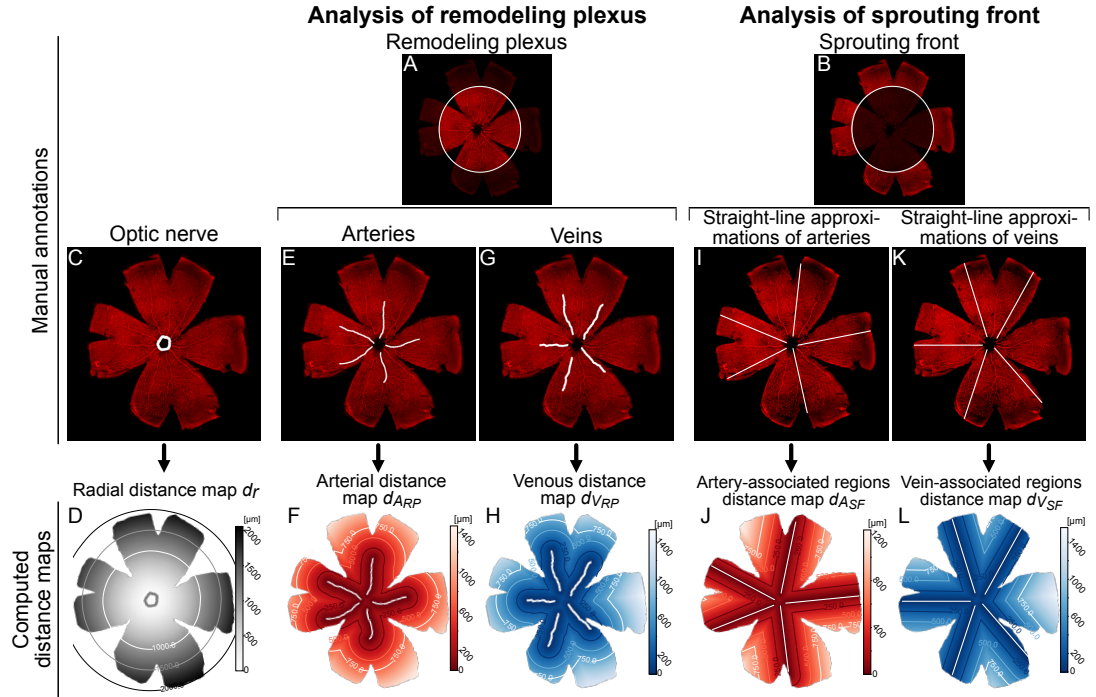


Figure 9.2: Distance maps of the retina based on manual annotations of the vessel anatomy. Different sets of distance maps were created for the analysis in the remodeling plexus (A) and the sprouting front (B). For both, the mask of the optic nerve (C) was used to create a map of the radial distance d_r (D). For analysis in the plexus, the arterial mask (E) and venous mask (G) were used to create distance maps of the arterial distance d_{ARP} (F) and the venous distance d_{VRP} (H). For the analysis of ECs in the sprouting front, straight-line approximations of arteries (I) and veins (K) were used to create maps of the distance to artery-associated regions d_{ASF} (J) and to vein-associated regions d_{VSF} (L).

As before, two maps were generated to separately analyze the EC distribution in the remodeling plexus and the sprouting front (figure 9.3). $\phi_{V \rightarrow ARP}$ was used for analysis in the remodeling plexus and denotes the relative distance of a given pixel between an actual vein and an actual artery in the retina (figure 9.3A). In the map, a pixel belonging to a vein has a value of 0 while a pixel belonging to an artery has a value of 1. $\phi_{V \rightarrow ASF}$ was used for analysis in the sprouting front and denotes the relative distance of a given pixel between regions in the retina that are more associated with veins and regions that are more associated with arteries (figure 9.3B).

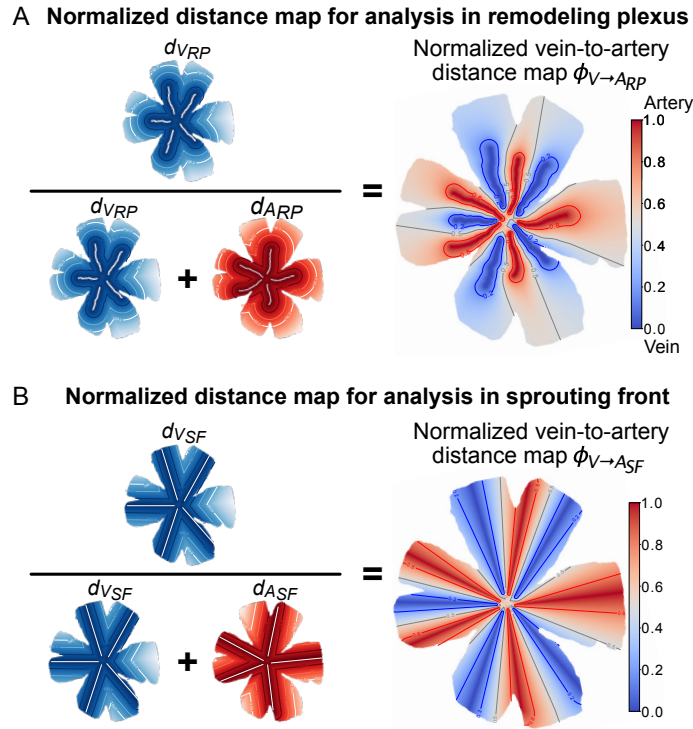


Figure 9.3: Distance maps of the retina that were created to normalize for retina size. **A** Distance map showing a normalized distance between veins and arteries used for analysis in the remodeling plexus. Pixels lying directly on top of a vein have a score of 0, pixels lying directly on top of an artery have a score of 1. **B** Distance map showing a normalized distance between regions that are more associated with veins and regions that are more associated with arteries used for analysis in the sprouting front.

Visualizing the spatial distribution of ECs: The positions of GFP-positive pixels on these distance maps correspond to the spatial distribution of the labeled subset of ECs. The data was summarized and plotted per time point (P6, P7, P8, P9) and condition (control, *Cdc42* iECKO, *Rac1* iECKO). Two different types of plots were generated (figure 9.4). The first is a contour plot, or 2D kernel density plot, of the 2D distribution of GFP-positive (i.e. labeled) pixels with respect to the relative vein-to-artery (V-A) position and the radial position. Therefore, $\phi_{V \rightarrow A_{RM/SF}}$ is plotted on the x -axis and d_r on the y -axis (figure 9.4A). The darker spectrum of the color gradient indicates a higher number of cells that were localized in this region. In addition, the same data are represented as 1D histograms at the top margin (spatial distribution of ECs between veins and arteries) and the left margin (spatial distribution of ECs with respect to the optic nerve). In these plots, the spatial distribution of GFP-labeled ECs of *all* retinas

9.2. Computational method to extract the spatial distribution of ECs from microscopy images of the developing mouse retina

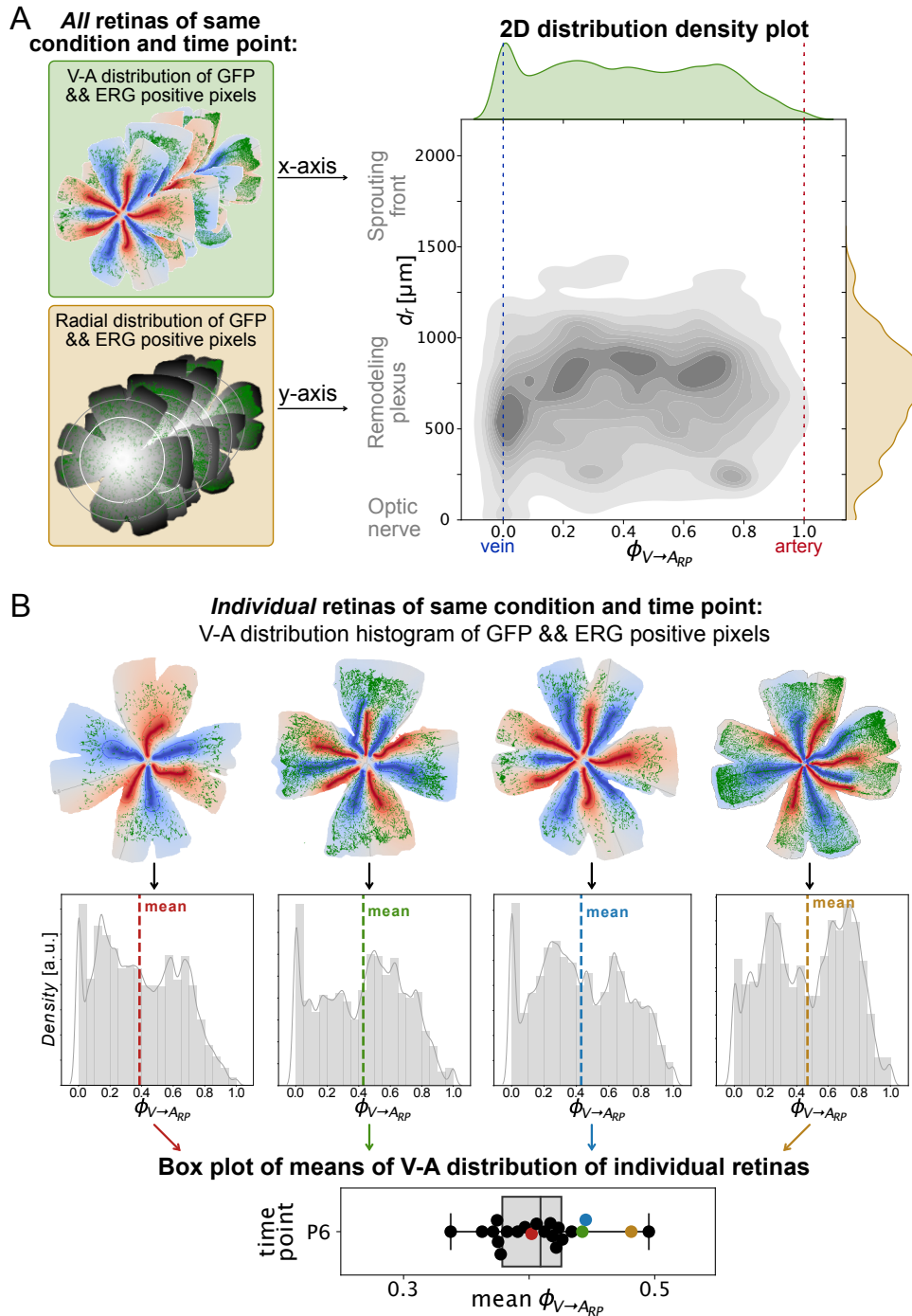


Figure 9.4: Visualization of the EC distributions. **A** Overview of 2D distribution density plot showing the spatial distribution of GFP-labeled ECs with respect to their position between veins and arteries (x-axis) and their distance to the optic nerve (y-axis). All retinas of the same time point and condition are consolidated in one plot. **B** Overview of boxplot of means of individual vein-to-artery (V-A) distribution histograms. Representing the data this way allowed for statistical testing of differences between different conditions and time points.

of the same time point and condition are summarized in one plot. However, testing for significant differences is difficult when pooling the data like this as conventional statistical tests fail for two reasons: (1) they assume a normal distribution of the data and (2) when comparing data sets with large numbers (like is the case here) even small differences will be picked up as significant. Therefore, it was decided to also plot the means of the spatial distribution of *single* retinas for each condition and time point in a boxplot (figure 9.4B). Representing the data this way had the advantage that different groups could be compared for statistically significant differences using a Welch's t-test. Compared to the student's t-test, the Welch's t-test is more reliable when comparing two populations with different variances or sample sizes.

9.3 Data preparation and software

Manual annotation: Retina image annotation (optic nerve, veins, arteries, straight-line approximations of mature vessels, sprouting front, and retina outline) was performed in Fiji [238] using a custom-written macro. *Data organization:* All image files were cataloged in an excel table including information like path to folder of masks and manual annotations, condition, time point, pixel size etc. This file was looped over for analysis. *Analysis software:* All analysis software was written in Python 3.8 using a kedro pipeline workflow [195, 239]. The scripts are available on GitHub (https://github.com/wgiese/EC_migration_retina). *Normalization for differential GFP expression:* Besides normalizing for different retina sizes and for EC cell size (as described above), I also normalized for differential GFP expression across retinas. To do that, I incorporated 10000 randomly drawn GFP-positive pixels from each retina into the analysis. This way, I could ensure that each retina contributed with the same weight irrespective of how much GFP was expressed. Retinas with less than 10000 GFP-positive pixels were excluded from analysis.

Results and Discussion

10.1 2D distribution analysis shows EC distribution shift from veins to arteries in the developing mouse retina

To better understand how ECs migrate during development of the mouse retina, I investigated the population distribution shift of stochastically GFP-labeled ECs over time and space, based on a lineage-tracing approach. Mosaic GFP-labeling of VEGFR3-expressing ECs always occurred at P5, and retinas were collected at four different time points (P6, P7, P8, and P9). Consistent with the expected expression pattern of VEGFR3, GFP-positive cells were found in veins, the remodeling plexus, and the sprouting front, with very few labeled cells in arteries at P6 (figure 10.1A)¹. In contrast, GFP-labeled cells were consistently found in arteries four days after injection (figure 10.1D). For the quantitative assessment of this population shift, I used the novel 2D distribution image analysis method as described in chapter 9; separately for the remodeling plexus and the sprouting front. An example for visualizing the results in a 2D kernel density plot is shown in figure 10.1E. The plots display the GFP distribution of all retinas of the same condition and time point in a map from veins to arteries (left to right) and from optic nerve to sprouting front (bottom to top). The same data are also presented as 1D histograms: the vein-to-artery (V-A) distribution $\phi_{V \rightarrow ARP/SF}$ on top of the plot (in the following called upper margin plot) and the radial distribution from optic nerve to sprouting front d_r on the right side of the plot (side margin plot). A more detailed description of the plots can be found in method section 9.2 and figure

¹This finding was irrespective of the injection time point confirming that VEGFR3 is barely expressed in ECs in arteries between P5 and P9. Data for injection at P8 and collection at P9 not shown for brevity.

9.4.

The results of the analysis of the remodeling plexus are shown in figure 10.1E-H. At P6, the GFP distribution shows a distinct peak in veins, a uniform spread across the remodeling plexus and no signal in arteries, as expected for VEGFR3 expression (figure 10.1E). At P8, the peak in veins is decreased and the distribution across the remodeling plexus is shifted towards arteries (figure 10.1G). At P9, the distribution

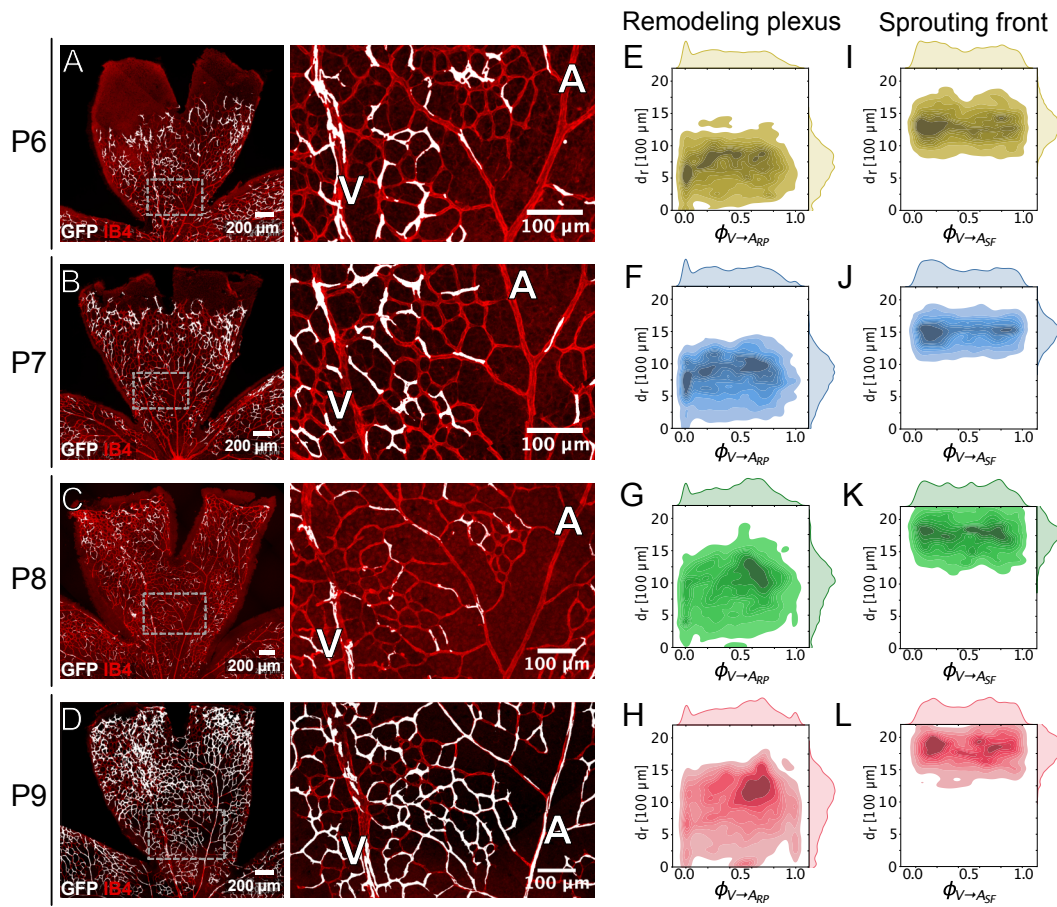


Figure 10.1: 2D distribution analysis of stochastically labeled ECs shows a population shift from veins to arteries and from optic nerve to retina periphery over time (adapted from [240]). **A-D** Microscopy images (*left*) and zoom-ins of dashed boxes (*right*) of the retina vasculature and a GFP-labeled subpopulation of ECs at P6, P7, P8 and P9. Labeling occurred at P5 in all cases. At P6, labeled cells are found in veins, remodeling plexus and sprouting front. At P9, labeled cells are also found in arteries. **E-H** 2D kernel density plots showing the distribution of labeled ECs at all time points in the remodeling plexus. **I-L** 2D kernel density plots showing the distribution of labeled ECs at all time points in the sprouting front. V: vein, A: artery.

shows a peak in arteries (figure 10.1H). Interestingly, at P9, the distribution in arteries also extends towards lower radial values closer to the optic nerve. When comparing the means of the V-A distributions of individual retinas, they also show a significant shift from veins to arteries over time (figure 10.4).

In the sprouting front, the population of labeled ECs does not significantly shift over time from veins to arteries (figure 10.1I-L).

In both the remodeling plexus and the sprouting front, the GFP distribution shifts from the area near the optic nerve towards the periphery of the retina over time (side margin plots in figure 10.1E-H and I-L). Looking at the radial distribution shift across the entire retina, it was significant from P6 to P8 ($p < 0.0001$) but then stagnated from P8 to P9 (see boxplot in figure B.1 in the appendix).

Looking at these data in isolation, it is not possible to explain how and why the EC distribution shifts over time. However, already published knowledge about the forces acting on ECs in the developing mouse retina can be taken into consideration in order to place the results into context. Simulations of hemodynamics in the retina have demonstrated blood flow from veins to arteries [220]. In addition, it is known that vascularization towards the periphery of the retina, meaning in the sprouting front, is mediated by VEGF signaling [38, 241]. In light of these previously published findings, the following interpretation of my results seems most plausible.

In the remodeling plexus, the EC distribution shift from veins to arteries over time suggests active migration of ECs along the plexus from low flow to high flow regions following shear stress cues. In fact, this flow-induced migration seems to continue in arteries towards the optic nerve. The absence of the distribution shift in the sprouting front might indicate the absence of any directed EC migration in this part of the retina. However, the used vessel reference system in the sprouting front, (i.e. the straight-line extensions of mature vessels in the plexus, see methods figures 9.2 and 9.3) might also not be sensitive enough to pick up directed movement such that no definite conclusions can be drawn from these results. The information is still valuable when compared to the distribution of cells with migration defects, as will become evident in section 10.2.

The radial EC distribution shift away from the optic nerve over time suggests active migration of ECs following VEGF signals sent from the poorly irrigated tissues at the periphery of the retina which has been reported previously [221]. However, it needs to be noted that the radial distribution from optic nerve to sprouting front does currently not account for retina growth over time, which leads me to the limitations of the method.

Even though the method does currently not account for retina growth over time, this would be important in order to draw definite conclusions about directed radial migration following VEGF signaling. This obstacle can be readily overcome by normalizing the radial coordinates for retina size. Still, this measure would not eliminate the inherent inaccuracies that are caused by tissue stretching during retina preparation. To minimize differences in tissue stretching, the same person should dissect and fix all retinas. Retina dissection also introduces a different issue as the empty space between the individual leaves influences the distance maps. Since I used a normalized distance between arteries and veins for the analysis, this did not affect the results. However, to look at real EC distances to mature vessels as well as their shift over time (to infer about migration velocities), it would be necessary to either project the 2D images back onto a 3D sphere or directly image the retinas in 3D using, for example, light sheet fluorescence microscopy [214]. Another, more fundamental limitation of the method is that the EC distribution can only be properly quantified with regard to a reference system, in this case the annotated retina parts (veins, arteries, optic nerve). Mature vessels are lacking in the sprouting front which means that the analysis does not allow explicit conclusions about directed migration between veins to arteries here. The straight-line extensions of mature vessels, which were added as a vascular reference system in the sprouting front, could not completely remedy this issue. Finally, the rough division of the retina into remodeling plexus and sprouting front using an ellipse is another limiting factor of the method. While this division is easily facilitated and sufficient for the intended purpose of this project, it might not be accurate enough for other applications. For example, applications targeting EC migration in the transition zone between plexus and sprouting front, which was recently shown to be an area of competing flow- and VEGF signaling [221], would require a more stringent segmentation of sprouting front and plexus.

In summary, these results show that the 2D distribution analysis method presented here is capable of extracting quantitative information about dynamic population shifts of ECs from static retina images. Comparing population distributions at several different time points after stochastic EC population labeling, a continuous shift from veins to arteries and from optic nerve to the periphery of the retina could be observed. This suggests that the method can pick up population shifts of ECs that were induced both by EC migration following flow/shear stress cues (vein to artery) and EC migration following VEGF gradients (optic nerve to periphery/sprouting front).

The 2D distribution analysis as presented in this thesis constitutes a useful addition

to already existing methods. Compared to the image analysis tool PolNet [220], it offers complementary information. While PolNet can be used to simulate hemodynamic forces and quantify EC polarization angles in retina images, the analytical approach presented here can be used to directly quantify EC migration. Combined, the two methods can therefore paint a fully dynamic picture of vascular development in response to blood flow and VEGF signaling from static images of the retina.

Barbacena et al. reported another retina image analysis method combining vessel morphology and EC polarisation (as a proxy for EC migration) [221]. They focused their analysis on sections of the vasculature around arteries in which VEGF-induced EC migration and flow-induced EC migration are opposed to each other, suggesting that both forces compete in a clearly defined transition zone between sprouting front and remodeling plexus. Due to the focus around arteries, their analysis showed a net EC polarization, also indicating a net EC migration, towards the periphery of the retina in the sprouting front, but towards the optic nerve in the plexus. In contrast, the analysis method presented in this thesis is not limited to arteries and can map EC migration across the entire vasculature. Hence, it also includes ECs in veins, where the two migration-driving forces align, and shows that there is a net movement of cells towards the periphery of the retina and away from the optic nerve not only in the sprouting front but also in the plexus. On a different note, Barbacena et al. segmented different parts of the retina (sprouting front, transition zone, remodeling plexus) based on a principal component analysis of vessel morphology which could improve my currently rather rough division of the retina into sprouting front and remodeling plexus using an ellipse.

In general, the biological results are in agreement with previously published work by Lee et al. based on lineage-tracing in the developing mouse retina. They labeled venous ECs specifically and also observed active migration from veins to arteries and against VEGF-gradients [222]. Also, Xu et al. showed movement of ECs from the sprouting front into arteries [242]. The novelty of the work presented here, however, lies in the quantitative computational analysis based on the analytical generation of a coordinate system of each retina to map the distributions of labeled cells. For the first time, it is possible to follow routes of EC migration in the developing mouse retina. Moreover, this method does not only allow a quantification of EC migration but also of the effect of the knockout of certain genes on EC migration, as will become evident in the following sections.

10.2 2D Distribution analysis reveals roles of Cdc42 and Rac1 for endothelial migration

Cdc42 and Rac1 are members of the Rho family of small GTPases, and are known to be involved in cellular migration processes through the regulation of filopodia formation (in the case of Cdc42) and lamellipodia formation (in the case of Rac1) [224, 225, 232]. To test if the distribution analysis can provide insights into the role of Cdc42 and Rac1 for EC migration, the same experiments and image analysis steps as before were performed- with the difference that the labeled EC population was also devoid of Cdc42 or Rac1, respectively. In these experiments, the overall vascular structure of the retinas was unaffected as background cells were wild-type and only labeled ECs were *Cdc42* or *Rac1* KOs. Importantly, this allowed to study possible migration defects of individual ECs in a healthy environment where parameters like hierarchical network patterning and blood flow were unaltered.

10.2.1 Cdc42 plays an essential role for endothelial migration under flow

Qualitatively, Cdc42-depleted ECs appear to move less from veins to arteries than control ECs as hardly any labeled cells populate arteries by P9, even in retinas with high recombination rates (figure 10.2D). This result is confirmed by the computational distribution analysis. Compared to control, the distribution of the Cdc42-depleted EC population looks different especially for later time points (figure 10.2E-L). In the remodeling plexus, the distribution shifts towards the center between veins and arteries up to P7 (10.2F, left side). However, no further shift towards arteries occurs at P8 and P9 (figure 10.2G and H, left side). Also, when comparing the means of the distributions of individual retinas between different time points in the remodeling plexus, no significant shift from veins to arteries can be observed (figure 10.4). In contrast, the upward shift of the distribution from the optic nerve towards the periphery of the retina is unaffected by the knockout (side margin plots in figure 10.2E-H and boxplot in figure B.1 in the appendix).

Interestingly, the results for the sprouting front also look different compared to control. In fact, the distribution shifts significantly towards veins for later time points (figure 10.2E-H, right side). The spread of the means between individual retinas is also reduced at P9 compared to P6, further indicating an accumulation of labeled cells in the venous deltas in the sprouting front over time (figure 10.4). This phenomenon could be explained by different mechanisms. First, this region is known to exhibit a

10.2. 2D Distribution analysis reveals roles of Cdc42 and Rac1 for endothelial migration

high local proliferation rate [230]. Hence, proliferation of labeled cells that fail to move towards arteries could account for the shift. Second, the net movement of non-labeled ECs from veins to arteries might be responsible for this apparent backward shift of labeled ECs. Finally, a third possibility is that Cdc42 is required for shear-mediated EC migration but dispensable for VEGF-mediated EC migration. Hence, cells could still move up along a vein towards the sprouting front but then get stuck there. The fact that the distribution of Cdc42-depleted ECs still shifts towards the periphery of the retina supports this hypothesis because it suggests intact active EC migration following VEGF signaling cues (side margin plots in figure 10.2E-H and boxplot in figure B.1 in the appendix). However, this finding could also be explained by immobile Cdc42-depleted ECs staying in the sprouting front but wild-type ECs that migrate from the

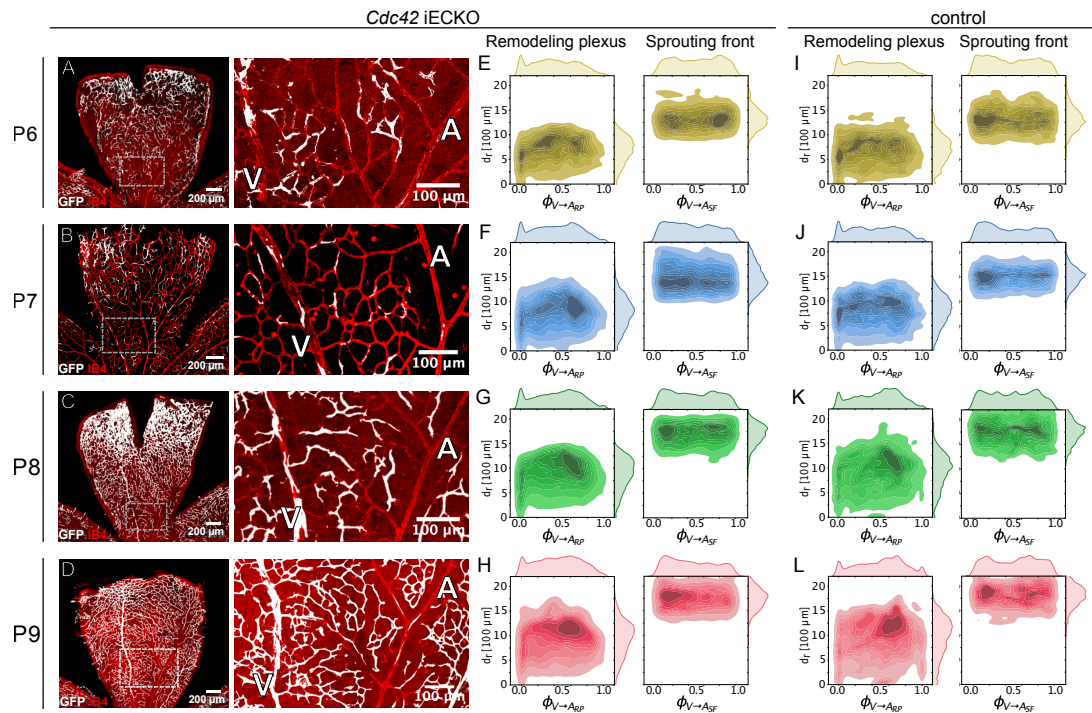


Figure 10.2: 2D distribution analysis of Cdc42-depleted ECs (adapted from [240]). **A-D** Microscopy images (*left*) and zoom-ins of dashed boxes (*right*) of the retina vasculature and GFP-labeled Cdc42-depleted ECs at P6, P7, P8 and P9. In contrast to control ECs, labeled Cdc42-depleted ECs do not populate arteries by P9. **E-H** 2D kernel density plots showing the distribution of labeled Cdc42-depleted ECs at all time points in the remodeling plexus (*left*) and the sprouting front (*right*). **I-L** 2D kernel density plots for the control condition for comparison (same data as in figure 10.1). V: vein, A: artery. iECKO: inducible, endothelial cell specific knockout.

sprouting front into arteries. The movement of tip cells into arteries has been described earlier [242] as has the fact that Cdc42-depleted ECs fail to adopt a tip cell phenotype [230].

In conclusion, Cdc42-depleted cells fail to move towards and into arteries but seem to still be able to move towards the periphery of the retina. The importance of Cdc42 for EC migration has been reported previously, both *in vitro* [226, 227] and *in vivo* [230, 231]. However, using the computational image analysis method presented in this thesis, it is possible to infer about affected migration routes of ECs in the developing mouse retina. The results indicate that Cdc42 might only be essential for flow-mediated EC migration but not for VEGF-mediated migration. Further *in vitro* and *in silico* experiments are needed to test this hypothesis.

10.2.2 Rac1-depleted cells show minor migration defects

I also investigated the role of the Rho GTPase Rac1 for EC migration by the same means as before. Qualitatively, the distribution of Rac1-depleted ECs did not differ considerably from control (figure 10.3A-D).

At P6, arteries were devoid of labeled ECs. At P9, they were populated by some labeled cells. However, the computational analysis picked up minor migration defects in the remodeling plexus. The distribution of *Rac1* KO ECs still showed a significant shift from veins to arteries but with slower initial progression (figure 10.4). Also, fewer cells ended up in the artery by P9 compared to control, and no downward shift in the artery towards the optic nerve could be observed (left side in figure 10.3H vs. left side in figure 10.3L). This initial shift delay could, for example, be explained if Rac1-depletion is more detrimental in low-shear (around the vein) than in high-shear (around the artery) conditions. However, the sprouting front is also a region of low shear stress, and the EC distribution shift there seemed unaffected by Rac1 depletion. It is possible that the straight-line extensions of vessels as vascular reference system in the sprouting front was not sensitive enough to pick up just minor differences in the EC distributions. Therefore, this hypothesis needs to be tested by further *in vitro* experiments. In contrast to the V-A distribution shift, the radial distribution shift from remodeling plexus to sprouting front was not delayed and even seemed accelerated from P8 to P9 compared to control (boxplot in figure B.1 in the appendix). This result indicates that Rac1 is not required for VEGF-mediated EC migration.

In conclusion, the analysis suggests that EC migration following VEGF signaling is not affected and EC migration following shear stress is only slightly impaired by Rac1

10.2. 2D Distribution analysis reveals roles of Cdc42 and Rac1 for endothelial migration

depletion. In order to investigate if EC migration is indeed only delayed, it would be necessary to observe if Rac1-depleted ECs arrive in arteries and migrate towards the optic nerve at later time points, i.e. five days or more after labeling.

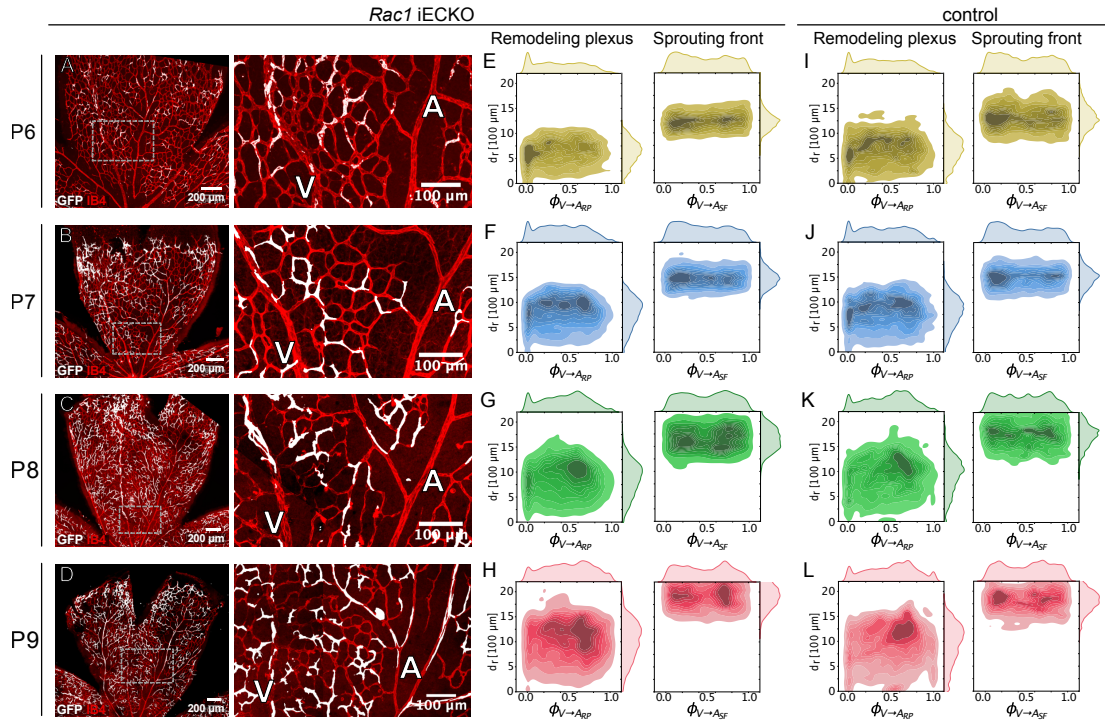


Figure 10.3: 2D distribution analysis of Rac1-depleted ECs (adapted from [240]). **A-D** Microscopy images (*left*) and zoom-ins of dashed boxes (*right*) of the retina vasculature and GFP-labeled Rac1-depleted ECs at P6, P7, P8 and P9. Compared to control ECs, labeled Rac1-depleted ECs populate arteries less by P9. **E-H** 2D kernel density plots showing the distribution of labeled Rac1-depleted ECs at all time points in the remodeling plexus (*left*) and the sprouting front (*right*). **I-L** 2D kernel estimation plots for the control condition for comparison (same data as in figure 10.1). V: vein, A: artery. iECKO: inducible, endothelial cell specific knockout.

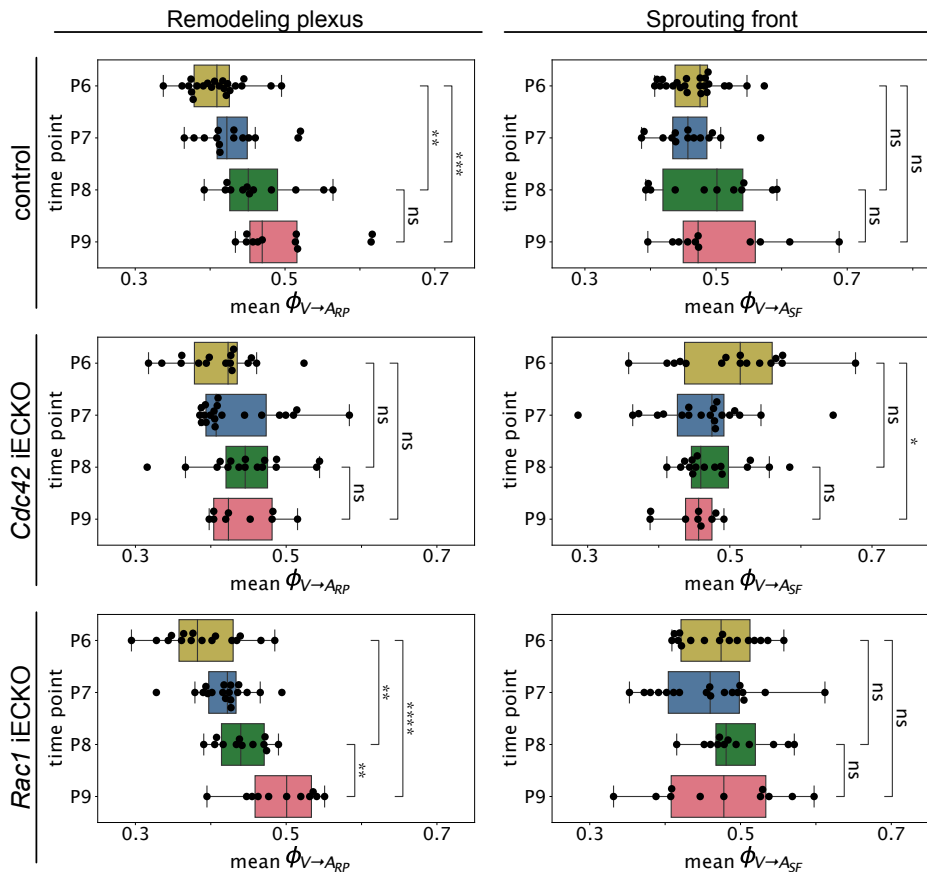


Figure 10.4: Boxplot of the mean V-A distribution of individual retinas for all three conditions (adapted from [240]). In the remodeling plexus, the mean V-A distribution shows a significant shift from veins to arteries in the control condition. For *Cdc42* iECKO, there is no shift. For *Rac1* iECKO, there is a significant shift but with slower initial onset compared to control (significance comparing P6 to P9 and P8 to P9 but not comparing P6 to P8). In the sprouting front, *Cdc42* iECKO showed a significant shift towards veins over time.

iECKO: inducible, endothelial cell specific knockout. ns: not significant, * $p < 0.05$, ** $p < 0.01$, *** $p < 0.001$, **** $p < 0.0001$.

Conclusions and Outlook

In this work, a new computational image analysis tool to extract EC dynamics from static images of the developing retina was developed. By generating a general coordinate system of a retina, I could map and quantify the 2D distribution shift of a randomly labeled, VEGFR3-expressing EC subpopulation with respect to the vasculature over time and space, and found that the EC distribution shifts from veins to arteries. Taking previously published data into consideration, these findings suggest that ECs actively migrate from veins to arteries across the remodeling plexus following shear stress cues. This result is also in agreement with previously reported qualitative observations. This analytical approach is universally applicable to trace and quantify the distribution of a population of labeled cells, even for non-selective initial stochastic recombination, and is insensitive to the recombination rate. In addition, I could show that the method is able to unravel EC migration defects induced by the knock-out of the Rho GTPases Cdc42 and Rac1, and that it can distinguish between defects in VEGF-mediated and shear-mediated migration.

In combination with other image analysis tools or simulations of hemodynamics, the reported method allows to study the dynamics of vascular growth and remodeling using static images of the retina. Therefore, this work paves the way for many exciting applications. For example, these results could be used as a foundation for computational modeling in which agents move on the vasculature of a segmented retina leaf. To better understand the connection between EC migration velocity and blood flow or VEGF signaling, one could tune parameters like the coupling strength of the agent movement to a flow-induced force field or a VEGF-induced force field until the modeling output matches the results of the 2D distribution analysis. To prove that there is, in fact, a directed movement of ECs, it would also be possible to compare the coupled agent

movement with a random walk along the segmented vessels.

Besides investigating migration-flow coupling in general, this method could also facilitate the identification of key proteins involved in EC mechanosensing. Similar to what I showed for the Rho GTPases Cdc42 and Rac1, it would be possible to knock-out any other gene and use the method to observe potential effects on EC migration. Naturally, one could also study external influences on EC migration, for example, by the administration of certain drugs. In fact, the analysis method is not limited to the retina, ECs, or even the vasculature, but could be easily transferred to other model systems or cell types, as long as there is an entity whose position can be quantified with respect to some kind of reference system.

In conclusion, this work comprises a significant contribution to the toolbox of methods to study the mechanisms of directed EC migration, ultimately aiming at the identification of pathomechanisms in vascular diseases and the development of strategies for selective therapies.

PART IV

Summary

In this thesis, I established two methods to advance quantitative *in vivo* imaging of vascular remodeling in different model systems. These methods aim to elucidate the relationship between hemodynamics and VEGF signaling on the one hand, and endothelial dynamics on the other hand. The two approaches address different aspects of this relationship and overcome current limitations in imaging the zebrafish trunk vasculature and the developing mouse retina. In this dissertation, I have presented the capabilities of the methods to achieve this goal.

In the first project, presented in part II, I established an OR-PAM system for functional imaging of the zebrafish trunk vasculature. It features high spatial resolution, high detection sensitivity, and the potential to quantify blood oxygenation and blood flow. Thus, it allows live *in vivo* imaging of hemodynamics in the zebrafish. The OR-PAM system also allows integration with other techniques for imaging the endothelium with single-cell resolution, such as multi-photon microscopy. Therefore, my work opens the way to directly observe the EC response to changes in hemodynamics and to determine possible hemodynamic thresholds that induce certain EC behaviors.

In the second project, presented in part III, I developed a computational image analysis method to quantify the spatial distribution shift of ECs with respect to a vascular reference system in a series of images of the developing mouse retina. This allowed me to extract dynamic information from static images. Since a dissected and fixed developing mouse retina of the correct time point represents the vasculature in all its remodeling stages, my image analysis method allowed the study of EC migration principles following both VEGF and flow signaling cues. In addition, I was able to quantify migration defects in ECs lacking certain proteins, making it a valuable tool for studying the molecular pathways that regulate EC migration. In particular, I showed that the Rho GTPase Cdc42 is required for EC migration and that deletion of Rac1 only induces minor migration defects.

Taken together, these projects represent a significant addition to the tools available to quantitatively study the role of endothelial dynamics in vascular growth and network patterning. In combination with other methods, my work may help to uncover the underlying mechanisms of endothelial dynamics and, more broadly, vascular remodeling in development and disease. It may also help to identify pathomechanisms of vascular disease and test treatment strategies for selective intervention.

Additional data for part II

A.1 OR-PAM with an FP sensor with a 5 μm spacer

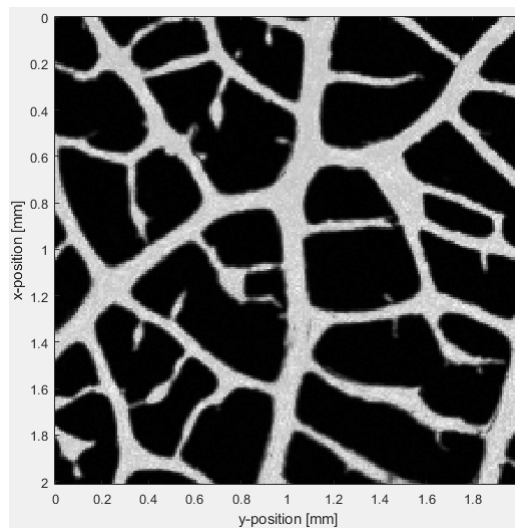


Figure A.1: OR-PAM image of a leaf skeleton phantom obtained with an FP sensor with a 5 μm spacer in raster-scanning mode. Even though the backing substrate was glass instead of COP, the sensor showed high acoustic sensitivity and has the potential to be integrated in a cranial window. Acquisition parameters: 532 nm excitation wavelength, <100 nJ pulse energy, 20 μm step size, 5 signals were averaged per pixel.

A.2 Development of a Raman laser for OR-PAM

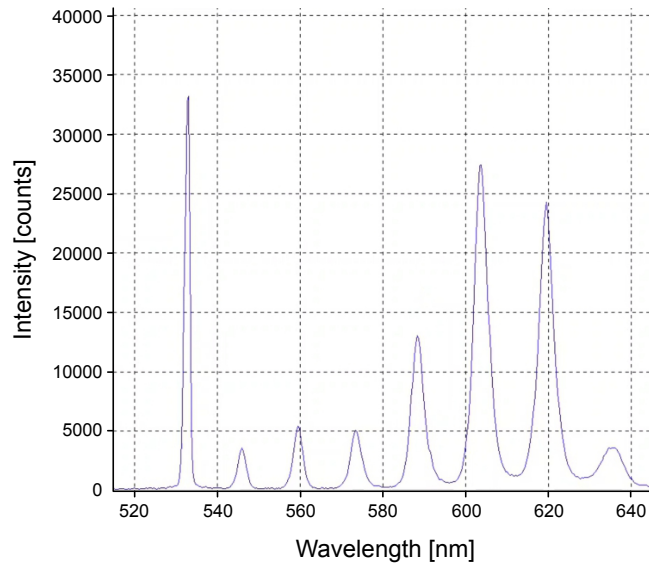


Figure A.2: Raman spectrum obtained after coupling the pulsed 532 nm excitation laser through a silicon dioxide optical fiber. The output was intensity filtered (ND 2.0) before entering the photospectrometer. The intensity of the lines could be varied by changing the polarization of the incoming light. The pulse energy of important Raman lines for spectroscopic OR-PAM was found to be sufficient for imaging. For the Raman line at 560 nm, the output power was 13.5 mW. As the used PRR was 20 kHz, this translated to a pulse energy of 700 nJ. For the Raman line at 573 nm, the power was 20 mW, which corresponds to a pulse energy of 1 μ J.

Additional data for part III

B.1 Radial distribution shift of ECs is barely affected by knockout of Cdc42 and Rac1

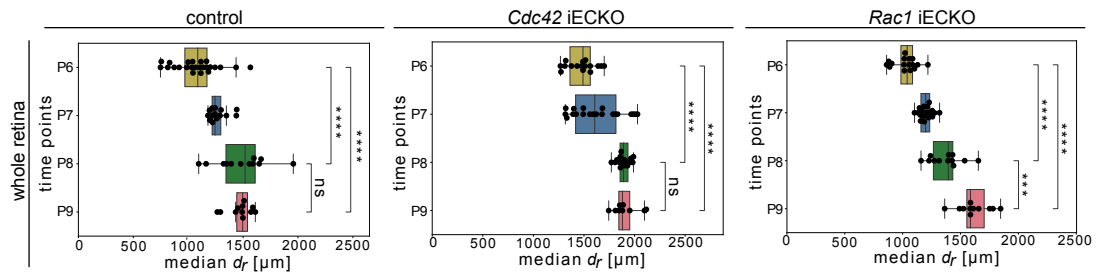


Figure B.1: Radial distribution shift of ECs is unaffected by knockout of Cdc42. Knockout of Rac1 slightly affected the radial distribution shift over time as it did not slow down from P8 to P9 but instead seemed to accelerate. iECKO: inducible, endothelial cell specific knockout. ns: not significant, *** $p < 0.001$, **** $p < 0.0001$.

References

- [1] Rita Monahan-Earley, Ann M Dvorak, and William C Aird. Evolutionary origins of the blood vascular system and endothelium. *Journal of Thrombosis and Haemostasis*, 11:46–66, 2013.
- [2] Konstantin Gaengel, Guillem Genové, Annika Armulik, and Christer Betsholtz. Endothelial-mural cell signaling in vascular development and angiogenesis. *Arteriosclerosis, Thrombosis, and Vascular Biology*, 29(5):630–638, 2009.
- [3] Michael Potente and Taija Mäkinen. Vascular heterogeneity and specialization in development and disease. *Nature Reviews Molecular Cell Biology*, 18(8):477–494, 2017.
- [4] Johnathon R Walls, Leigh Coultas, Janet Rossant, and R Mark Henkelman. Three-dimensional analysis of vascular development in the mouse embryo. *PLoS ONE*, 3(8):e2853, 2008.
- [5] Michael Potente, Holger Gerhardt, and Peter Carmeliet. Basic and therapeutic aspects of angiogenesis. *Cell*, 146(6):873–887, 2011.
- [6] Valentin Djonov, M Schmid, Stefan A Tschanz, and Peter H Burri. Intussusceptive angiogenesis: its role in embryonic vascular network formation. *Circulation Research*, 86(3):286–292, 2000.
- [7] Roberto Gianni-Barrera, Marianna Trani, Silvia Reginato, and Andrea Banfi. To sprout or to split? VEGF, Notch and vascular morphogenesis. *Biochemical Society Transactions*, 39(6):1644–1648, 2011.
- [8] Peter Carmeliet. Angiogenesis in life, disease and medicine. *Nature*, 438(7070):932–936, 2005.

REFERENCES

- [9] Bryan L Krock, Nicolas Skuli, and M Celeste Simon. Hypoxia-induced angiogenesis: good and evil. *Genes & Cancer*, 2(12):1117–1133, 2011.
- [10] Samantha N Greer, Julie L Metcalf, Yi Wang, and Michael Ohh. The updated biology of hypoxia-inducible factor. *The EMBO Journal*, 31(11):2448–2460, 2012.
- [11] Anna Szymborska and Holger Gerhardt. Hold me, but not too tight—endothelial cell–cell junctions in angiogenesis. *Cold Spring Harbor Perspectives in Biology*, 10(8):a029223, 2018.
- [12] Hellmut G Augustin, Gou Young Koh, Gavin Thurston, and Kari Alitalo. Control of vascular morphogenesis and homeostasis through the angiopoietin–Tie system. *Nature Reviews Molecular Cell Biology*, 10(3):165–177, 2009.
- [13] Holger Gerhardt, Matthew Golding, Marcus Fruttiger, Christiana Ruhrberg, Andrea Lundkvist, Alexandra Abramsson, Michael Jeltsch, Christopher Mitchell, Kari Alitalo, David Shima, and Christer Betsholtz. VEGF guides angiogenic sprouting utilizing endothelial tip cell filopodia. *The Journal of Cell Biology*, 161(6):1163–1177, 2003.
- [14] Lars Jakobsson, Claudio A Franco, Katie Bentley, Russell T Collins, Bas Ponsioen, Irene M Aspalter, Ian Rosewell, Marta Busse, Gavin Thurston, Alexander Medvinsky, Stefan Schulte-Merker, and Holger Gerhardt. Endothelial cells dynamically compete for the tip cell position during angiogenic sprouting. *Nature Cell Biology*, 12(10):943–953, 2010.
- [15] John C Pelton, Catherine E Wright, Michael Leitges, and Victoria L Bautch. Multiple endothelial cells constitute the tip of developing blood vessels and polarize to promote lumen formation. *Development*, 141(21):4121–4126, 2014.
- [16] Hanna M Eilken and Ralf H Adams. Dynamics of endothelial cell behavior in sprouting angiogenesis. *Current Opinion in Cell Biology*, 22(5):617–625, 2010.
- [17] Anna-Karin Olsson, Anna Dimberg, Johan Kreuger, and Lena Claesson-Welsh. VEGF receptor signalling? In control of vascular function. *Nature Reviews Molecular Cell Biology*, 7(5):359–371, 2006.
- [18] Mats Hellström, Li-Kun Phng, Jennifer J Hofmann, Elisabet Wallgard, Leigh Coultas, Per Lindblom, Jackelyn Alva, Ann-Katrin Nilsson, Linda Karlsson, Nicholas Gaiano, Keejung Yoon, Janet Rossant, M Luisa Iruela-Arispe, Mattias

-
- Kalén, Holger Gerhardt, and Christer Betsholtz. Dll4 signalling through Notch1 regulates formation of tip cells during angiogenesis. *Nature*, 445(7129):776–780, 2007.
- [19] Li-Kun Phng and Holger Gerhardt. Angiogenesis: a team effort coordinated by Notch. *Developmental Cell*, 16(2):196–208, 2009.
- [20] Charles Betz, Anna Lenard, Heinz-Georg Belting, and Markus Affolter. Cell behaviors and dynamics during angiogenesis. *Development*, 143(13):2249–2260, 2016.
- [21] Rakesh K Jain. Molecular regulation of vessel maturation. *Nature Medicine*, 9(6):685–693, 2003.
- [22] Ivan B Lobov, Sujata Rao, Thomas J Carroll, Jefferson E Vallance, Masataka Ito, Jennifer K Ondr, Savita Kurup, Donald A Glass, Millan S Patel, Weiguo Shu, Edward E Morrissey, Andrew P McMahon, Gerard Karsenty, and Richard A Lang. WNT7b mediates macrophage-induced programmed cell death in patterning of the vasculature. *Nature*, 437(7057):417–421, 2005.
- [23] Qi Chen, Luan Jiang, Chun Li, Dan Hu, Ji-wen Bu, David Cai, and Jiu-lin Du. Haemodynamics-driven developmental pruning of brain vasculature in zebrafish. *PLoS Biology*, 2012.
- [24] Claudio A Franco, Martin L Jones, Miguel O Bernabeu, Ilse Geudens, Thomas Mathivet, Andre Rosa, Felicia M Lopes, Aida P Lima, Anan Ragab, Russell T Collins, Li-Kun Phng, Peter V Coveney, and Holger Gerhardt. Dynamic endothelial cell rearrangements drive developmental vessel regression. *PLoS Biology*, 13(4):e1002125, 2015.
- [25] Ruslan Hlushchuk, Martin Ehrbar, Philipp Reichmuth, Niklas Heinemann, Beata Styp-Rekowska, Robert Escher, Oliver Baum, Philipp Lienemann, Andrew Makanya, Eli Keshet, and Valentin Djonov. Decrease in VEGF expression induces intussusceptive vascular pruning. *Arteriosclerosis, Thrombosis, and Vascular Biology*, 31(12):2836–2844, 2011.
- [26] Nicolas Baeyens and Martin A Schwartz. Biomechanics of vascular mechanosensation and remodeling. *Molecular Biology of The Cell*, 27(1):7–11, 2016.

REFERENCES

- [27] Nurul F Jufri, Abidali Mohamedali, Alberto Avolio, and Mark S Baker. Mechanical stretch: physiological and pathological implications for human vascular endothelial cells. *Vascular Cell*, 7(1):1–12, 2015.
- [28] Jennifer L Lucitti, Elizabeth AV Jones, Chengqun Huang, Ju Chen, Scott E Fraser, and Mary E Dickinson. Vascular remodeling of the mouse yolk sac requires hemodynamic force. *Development*, 2007.
- [29] Ivo Buschmann, Axel Pries, Beata Styp-Rekowska, Philipp Hillmeister, Laurent Loufrani, Daniel Henrion, Yu Shi, Andre Duelsner, Imo Hofer, Nora Gatzke, Haitao Wang, Kerstin Lehmann, Lena Ulm, Zully Ritter, Peter Hauff, Ruslan Hlushchuk, Valentin Djonov, Toon van Veen, and Ferdinand le Noble. Pulsatile shear and Gja5 modulate arterial identity and remodeling events during flow-driven arteriogenesis. *Development*, 137(13):2187–2196, 2010.
- [30] Kathrina L Marcelo, Lauren C Goldie, and Karen K Hirschi. Regulation of endothelial cell differentiation and specification. *Circulation Research*, 112(9):1272–1287, 2013.
- [31] Claudio A Franco, Martin L Jones, Miguel O Bernabeu, Anne-Clemence Vion, Pedro Barbacena, Jieqing Fan, Thomas Mathivet, Catarina G Fonseca, Anan Ragab, Terry P Yamaguchi, Peter V Coveney, Richard A Lang, and Holger Gerhardt. Non-canonical Wnt signalling modulates the endothelial shear stress flow sensor in vascular remodelling. *Elife*, 5:e07727, 2016.
- [32] Shom Goel, Dan G Duda, Lei Xu, Lance L Munn, Yves Boucher, Dai Fukumura, and Rakesh K Jain. Normalization of the vasculature for treatment of cancer and other diseases. *Physiological Reviews*, 91(3):1071–1121, 2011.
- [33] Rakesh K Jain. Normalization of tumor vasculature: an emerging concept in antiangiogenic therapy. *Science*, 307(5706):58–62, 2005.
- [34] Jennifer L Lucitti, Robert Sealock, Brian K Buckley, Hua Zhang, Lin Xiao, Andrew C Dudley, and James E Faber. Variants of rab GTPase-effector binding protein-2 cause variation in the collateral circulation and severity of stroke. *Stroke*, 47(12):3022–3031, 2016.
- [35] George Bowley, Elizabeth Kugler, Rob Wilkinson, Allan Lawrie, Freek van Eeden, Tim JA Chico, Paul C Evans, Emily S Noël, and Jovana Serbanovic-Canic.

- Zebrafish as a tractable model of human cardiovascular disease. *British Journal of Pharmacology*, 179(5):900–917, 2022.
- [36] Sumio Isogai, Masaharu Horiguchi, and Brant M Weinstein. The vascular anatomy of the developing zebrafish: an atlas of embryonic and early larval development. *Developmental Biology*, 230(2):278–301, 2001.
- [37] Kazuhide S Okuda and Benjamin M Hogan. Endothelial cell dynamics in vascular development: insights from live-imaging in zebrafish. *Frontiers in Physiology*, page 842, 2020.
- [38] Marcus Fruttiger. Development of the retinal vasculature. *Angiogenesis*, 10(2):77–88, 2007.
- [39] Andreas Stahl, Kip M Connor, Przemyslaw Sapielha, Jing Chen, Roberta J Dennison, Nathan M Krahl, Molly R Seaward, Keirnan L Willett, Christopher M Aderman, Karen I Guerin, Jing Hua, Chatarina Löfqvist, Ann Hellström, and Lois EH Smith. The mouse retina as an angiogenesis model. *Investigative Ophthalmology & Visual Science*, 51(6):2813–2826, 2010.
- [40] Senthil Selvam, Tejas Kumar, and Marcus Fruttiger. Retinal vasculature development in health and disease. *Progress in Retinal and Eye Research*, 63:1–19, 2018.
- [41] Ruslan Rust, Lisa Grönnert, Berre Dogançay, and Martin E Schwab. A revised view on growth and remodeling in the retinal vasculature. *Scientific Reports*, 9(1):1–9, 2019.
- [42] Ingeborg Stalmans, Yin-Shan Ng, Richard Rohan, Marcus Fruttiger, Ann Bouché, Ali Yuce, Hajime Fujisawa, Bart Hermans, Moshe Shani, Sandra Jansen, Dan Hicklin, David J Anderson, Tom Gardiner, Hans-Peter Hammes, Lieve Moons, Mieke Dewerchin, Désiré Collen, Peter Carmeliet, and Patricia A D’Amore. Arteriolar and venular patterning in retinas of mice selectively expressing VEGF isoforms. *The Journal of Clinical Investigation*, 109(3):327–336, 2002.
- [43] Rui Benedito, Cristina Roca, Inga Sörensen, Susanne Adams, Achim Gossler, Marcus Fruttiger, and Ralf H Adams. The notch ligands Dll4 and Jagged1 have opposing effects on angiogenesis. *Cell*, 137(6):1124–1135, 2009.

REFERENCES

- [44] Emma S Rennel, Steven J Harper, and David O Bates. Therapeutic potential of manipulating VEGF splice isoforms in oncology. *Future Oncology*, 5(5):703–712, 2009.
- [45] Sonja Loges, C Roncal, and Peter Carmeliet. Development of targeted angiogenic medicine. *Journal of Thrombosis and Haemostasis*, 7(1):21–33, 2009.
- [46] Alexander Graham Bell. On the production and reproduction of sound by light. *American Journal of Science (1880-1910)*, 20(118):305, 1880.
- [47] Lihong V Wang. Tutorial on photoacoustic microscopy and computed tomography. *IEEE Journal of Selected Topics in Quantum Electronics*, 14(1):171–179, 2008.
- [48] Mansik Jeon and Chulhong Kim. Multimodal photoacoustic tomography. *IEEE Transactions on Multimedia*, 15(5):975–982, 2013.
- [49] Eric M Strohm, Michael J Moore, and Michael C Kolios. Single cell photoacoustic microscopy: a review. *IEEE Journal of Selected Topics in Quantum Electronics*, 22(3):137–151, 2015.
- [50] Minghua Xu and Lihong V Wang. Photoacoustic imaging in biomedicine. *Review of Scientific Instruments*, 77(4):041101, 2006.
- [51] Seungwan Jeon, Jongbeom Kim, Donghyun Lee, Jin Woo Baik, and Chulhong Kim. Review on practical photoacoustic microscopy. *Photoacoustics*, 15:100141, 2019.
- [52] Howard L Fang, Donna M Meister, and Robert L Swofford. Photoacoustic spectroscopy of vibrational overtones in gas-phase methanol and methanol-d (CH₃OD). *The Journal of Physical Chemistry*, 88(3):405–409, 1984.
- [53] Jan Laufer, Ben Cox, Edward Zhang, and Paul Beard. Quantitative determination of chromophore concentrations from 2D photoacoustic images using a non-linear model-based inversion scheme. *Applied Optics*, 49(8):1219–1233, 2010.
- [54] Junjie Yao and Lihong V Wang. Sensitivity of photoacoustic microscopy. *Photoacoustics*, 2(2):87–101, 2014.
- [55] Johann Heinrich Lambert. *Photometria sive de mensura et gradibus luminis, colorum et umbrae*. Sumptibus Vidvae E. Klett, Typis CP Detleffsen, 1760.

-
- [56] August Beer. Determination of the absorption of red light in colored liquids. *Annalen der Physik und Chemie*, 86(5):78–88, 1852.
- [57] F Alan McDonald. Photoacoustic effect and the physics of waves. *American Journal of Physics*, 48(1):41–47, 1980.
- [58] Qian Chen, Wei Qin, Weizhi Qi, and Lei Xi. Progress of clinical translation of handheld and semi-handheld photoacoustic imaging. *Photoacoustics*, 22:100264, 2021.
- [59] Srirang Manohar and Maura Dantuma. Current and future trends in photoacoustic breast imaging. *Photoacoustics*, 16:100134, 2019.
- [60] Kornel P Kostli, Daniel Frauchiger, Joël J Niederhauser, Günther Paltauf, Heinz P Weber, and Martin Frenz. Optoacoustic imaging using a three-dimensional reconstruction algorithm. *IEEE Journal of Selected Topics in Quantum Electronics*, 7(6):918–923, 2001.
- [61] Minghua Xu and Lihong V Wang. Universal back-projection algorithm for photoacoustic computed tomography. *Physical Review E: Stat. Nonlin. Soft Matter Phys*, 71(1):016706, 2005.
- [62] Peter Burgholzer, Gebhard J Matt, Markus Haltmeier, and Günther Paltauf. Exact and approximative imaging methods for photoacoustic tomography using an arbitrary detection surface. *Physical Review E*, 75(4):046706, 2007.
- [63] Bradley E Treeby and Benjamin T Cox. k-wave: MATLAB toolbox for the simulation and reconstruction of photoacoustic wave fields. *Journal of Biomedical Optics*, 15(2):021314, 2010.
- [64] Xueding Wang, Yongjiang Pang, Geng Ku, George Stoica, and Lihong V Wang. Three-dimensional laser-induced photoacoustic tomography of mouse brain with the skin and skull intact. *Optics Letters*, 28(19):1739–1741, 2003.
- [65] Lei Li, Liren Zhu, Cheng Ma, Li Lin, Junjie Yao, Lidai Wang, Konstantin Maslov, Ruiying Zhang, Wanyi Chen, Junhui Shi, and Lihong V Wang. Single-impulse panoramic photoacoustic computed tomography of small-animal whole-body dynamics at high spatiotemporal resolution. *Nature Biomedical Engineering*, 1(5):0071, 2017.

REFERENCES

- [66] Sergey A Ermilov, Tuenchit Khamapirad, Andre Conjusteau, Morton H Leonard, Ron Lacewell, Ketan Mehta, Tom Miller, and Alexander A Oraevsky. Laser optoacoustic imaging system for detection of breast cancer. *Journal of Biomedical Optics*, 14(2):024007–024007, 2009.
- [67] Joel J Niederhauser, Michael Jaeger, Robert Lemor, Peter Weber, and Martin Frenz. Combined ultrasound and optoacoustic system for real-time high-contrast vascular imaging in vivo. *IEEE Transactions on Medical Imaging*, 24(4):436–440, 2005.
- [68] Sungjo Park, Changho Lee, Jeesu Kim, and Chulhong Kim. Acoustic resolution photoacoustic microscopy. *Biomedical Engineering Letters*, 4:213–222, 2014.
- [69] Junhui Shi, Yuqi Tang, and Junjie Yao. Advances in super-resolution photoacoustic imaging. *Quantitative Imaging in Medicine and Surgery*, 8(8):724, 2018.
- [70] Thomas Chaigne, Jérôme Gateau, Marc Allain, Ori Katz, Sylvain Gigan, Anne Sentenac, and Emmanuel Bossy. Super-resolution photoacoustic fluctuation imaging with multiple speckle illumination. *Optica*, 3(1):54–57, 2016.
- [71] Thomas Chaigne, Bastien Arnal, Sergey Vilov, Emmanuel Bossy, and Ori Katz. Super-resolution photoacoustic imaging via flow-induced absorption fluctuations. *Optica*, 4(11):1397–1404, 2017.
- [72] Jongbeom Kim, Jin Young Kim, Seungwan Jeon, Jin Woo Baik, Seong Hee Cho, and Chulhong Kim. Super-resolution localization photoacoustic microscopy using intrinsic red blood cells as contrast absorbers. *Light: Science & Applications*, 8(1):1–11, 2019.
- [73] Junjie Yao and Lihong V Wang. Photoacoustic microscopy. *Laser & Photonics Reviews*, 7(5):758–778, 2013.
- [74] Michaela Taylor-Williams, Graham Spicer, Gemma Bale, and Sarah E Bohndiek. Noninvasive hemoglobin sensing and imaging: optical tools for disease diagnosis. *Journal of Biomedical Optics*, 27(8):080901, 2022.
- [75] Seiji Ogawa, Tso-Ming Lee, Alan R Kay, and David W Tank. Brain magnetic resonance imaging with contrast dependent on blood oxygenation. *Proceedings of the National Academy of Sciences*, 87(24):9868–9872, 1990.

-
- [76] Gary H Glover. Overview of functional magnetic resonance imaging. *Neurosurgery Clinics*, 22(2):133–139, 2011.
- [77] Meir Nitzan, Ayal Romem, and Robert Koppel. Pulse oximetry: fundamentals and technology update. *Medical Devices: Evidence and Research*, pages 231–239, 2014.
- [78] Lidai Wang, Konstantin Maslov, and Lihong V Wang. Single-cell label-free photoacoustic flowoxigraphy in vivo. *Proceedings of the National Academy of Sciences*, 110(15):5759–5764, 2013.
- [79] Evgeny Zherebtsov, Viktor Dremin, Alexey Popov, Alexander Doronin, Daria Kurakina, Mikhail Kirillin, Igor Meglinski, and Alexander Bykov. Hyperspectral imaging of human skin aided by artificial neural networks. *Biomedical Optics Express*, 10(7):3545–3559, 2019.
- [80] Amrita Banerjee, Neha Bhattacharyya, Ria Ghosh, Soumendra Singh, Anirudha Adhikari, Susmita Mondal, Lopamudra Roy, Annie Bajaj, Nilanjana Ghosh, Aman Bhushan, Mahasweta Goswami, Ahmed SA Ahmed, Ziad Moussa, Pulak Mondal, Subhadipta Mukhopadhyay, Debasis Bhattacharyya, Arpita Chattopadhyay, Saleh A Ahmed, Asim Kumar Mallick, and Samir Kumar Pal. Non-invasive estimation of hemoglobin, bilirubin and oxygen saturation of neonates simultaneously using whole optical spectrum analysis at point of care. *Scientific Reports*, 13(1):2370, 2023.
- [81] Armin Schneider and Hubertus Feussner. *Biomedical Engineering in Gastrointestinal Surgery*. Academic Press, 2017.
- [82] Lin Wang, Jeffrey M Cochran, Tiffany Ko, Wesley B Baker, Kenneth Abramson, Lian He, David R Busch, Venki Kavuri, Rebecca L Linn, Samuel Parry, Arjun G Yodh, and Nadav Schwartz. Non-invasive monitoring of blood oxygenation in human placentas via concurrent diffuse optical spectroscopy and ultrasound imaging. *Nature Biomedical Engineering*, 6(9):1017–1030, 2022.
- [83] Shau Poh Chong, Conrad W Merkle, Conor Leahy, and Vivek J Srinivasan. Cerebral metabolic rate of oxygen (CMRO₂) assessed by combined Doppler and spectroscopic OCT. *Biomedical Optics Express*, 6(10):3941–3951, 2015.
- [84] Shau Poh Chong, Conrad W Merkle, Conor Leahy, Harsha Radhakrishnan, and Vivek J Srinivasan. Quantitative microvascular hemoglobin mapping using visible

REFERENCES

- light spectroscopic optical coherence tomography. *Biomedical Optics Express*, 6(4):1429–1450, 2015.
- [85] Michael Markl, Alex Frydrychowicz, Sebastian Kozerke, Mike Hope, and Oliver Wieben. 4D flow MRI. *Journal of Magnetic Resonance Imaging*, 36(5):1015–1036, 2012.
- [86] Gerwin P Schmidt, Maximilian F Reiser, and Andrea Baur-Melnyk. Whole-body MRI for the staging and follow-up of patients with metastasis. *European Journal of Radiology*, 70(3):393–400, 2009.
- [87] Pim J Van den Berg, Khalid Daoudi, and Wiendelt Steenbergen. Review of photoacoustic flow imaging: its current state and its promises. *Photoacoustics*, 3(3):89–99, 2015.
- [88] Christoph B Burckhardt. Speckle in ultrasound B-mode scans. *IEEE Transactions on Sonics and Ultrasonics*, 25(1):1–6, 1978.
- [89] Joseph M Schmitt, SH Xiang, and Kin Man Yung. Speckle in optical coherence tomography. *Journal of Biomedical Optics*, 4(1):95–105, 1999.
- [90] Eric M Strohm, Elizabeth SL Berndl, and Michael C Kolios. Probing red blood cell morphology using high-frequency photoacoustics. *Biophysical Journal*, 105(1):59–67, 2013.
- [91] Ruikang K Wang and Lin An. Doppler optical micro-angiography for volumetric imaging of vascular perfusion in vivo. *Optics Express*, 17(11):8926–8940, 2009.
- [92] Richard SC Cobbold. *Foundations of biomedical ultrasound*. Oxford University Press, 2006.
- [93] Lidai Wang, Konstantin Maslov, Junjie Yao, Bin Rao, and Lihong V Wang. Fast voice-coil scanning optical-resolution photoacoustic microscopy. *Optics Letters*, 36(2):139–141, 2011.
- [94] Jin Young Kim, Changho Lee, Kyungjin Park, Geunbae Lim, and Chulhong Kim. Fast optical-resolution photoacoustic microscopy using a 2-axis water-proofing mems scanner. *Scientific Reports*, 5(1):1–5, 2015.
- [95] Kyungjin Park, Jin Young Kim, Changho Lee, Seungwan Jeon, Geunbae Lim, and Chulhong Kim. Handheld photoacoustic microscopy probe. *Scientific Reports*, 7(1):1–15, 2017.

-
- [96] Yi Yuan, Sihua Yang, and Da Xing. Optical-resolution photoacoustic microscopy based on two-dimensional scanning galvanometer. *Applied Physics Letters*, 100(2):023702, 2012.
- [97] Thomas John Allen, Josh Spurrell, Martin O Berendt, Olumide Ogunlade, Shaif U Alam, Edward Z Zhang, David J Richardson, and Paul C Beard. Ultrafast laser-scanning optical resolution photoacoustic microscopy at up to 2 million A-lines per second. *Journal of Biomedical Optics*, 23(12):126502, 2018.
- [98] Jun Xia, Guo Li, Lidai Wang, Mohammadreza Nasiriavanaki, Konstantin Maslov, John A Engelbach, Joel R Garbow, and Lihong V Wang. Wide-field two-dimensional multifocal optical-resolution photoacoustic-computed microscopy. *Optics Letters*, 38(24):5236–5239, 2013.
- [99] Bangxin Lan, Wei Liu, Ya-chao Wang, Junhui Shi, Yang Li, Song Xu, Huaxin Sheng, Qifa Zhou, Jun Zou, Ulrike Hoffmann, Wei Yang, and Junjie Yao. High-speed widefield photoacoustic microscopy of small-animal hemodynamics. *Biomedical Optics Express*, 9(10):4689–4701, 2018.
- [100] Byullee Park, Hoyong Lee, Seungwan Jeon, Joongho Ahn, Hyung H Kim, and Chulhong Kim. Reflection-mode switchable subwavelength Bessel-beam and Gaussian-beam photoacoustic microscopy in vivo. *Journal of Biophotonics*, 12(2):e201800215, 2019.
- [101] Wonkyoung Kim, Changho Lee, Chulhong Kim, and Dong Sung Kim. Dual-mode reconfigurable focusing using the interface of aqueous and dielectric liquids. *Lab on a Chip*, 17(23):4031–4039, 2017.
- [102] Xiaoquan Yang, Bowen Jiang, Xianlin Song, Jianshuang Wei, and Qingming Luo. Fast axial-scanning photoacoustic microscopy using tunable acoustic gradient lens. *Optics Express*, 25(7):7349–7357, 2017.
- [103] Xiaoquan Yang, Xianlin Song, Bowen Jiang, and Qingming Luo. Multifocus optical-resolution photoacoustic microscope using ultrafast axial scanning of single laser pulse. *Optics Express*, 25(23):28192–28200, 2017.
- [104] Georg Wissmeyer, Miguel A Pleitez, Amir Rosenthal, and Vasilis Ntziachristos. Looking at sound: optoacoustics with all-optical ultrasound detection. *Light: Science & Applications*, 7(1):1–16, 2018.

REFERENCES

- [105] Song Hu and Lihong V Wang. Optical-resolution photoacoustic microscopy: auscultation of biological systems at the cellular level. *Biophysical Journal*, 105(4):841–847, 2013.
- [106] Paul Beard. Biomedical photoacoustic imaging. *Interface Focus*, 1(4):602–631, 2011.
- [107] Lihong V Wang and Junjie Yao. A practical guide to photoacoustic tomography in the life sciences. *Nature Methods*, 13(8):627–638, 2016.
- [108] Wei Liu and Junjie Yao. Photoacoustic microscopy: principles and biomedical applications. *Biomedical Engineering Letters*, 8:203–213, 2018.
- [109] Tri Vu, Daniel Razansky, and Junjie Yao. Listening to tissues with new light: recent technological advances in photoacoustic imaging. *Journal of Optics*, 21(10):103001, 2019.
- [110] Riqiang Lin, Jianhua Chen, Huina Wang, Meng Yan, Wei Zheng, and Liang Song. Longitudinal label-free optical-resolution photoacoustic microscopy of tumor angiogenesis in vivo. *Quantitative Imaging in Medicine and Surgery*, 5(1):23, 2015.
- [111] Zhiqiang Xu, Yinhao Pan, Ningbo Chen, Silue Zeng, Liangjian Liu, Rongkang Gao, Jianhui Zhang, Chihua Fang, Liang Song, and Chengbo Liu. Visualizing tumor angiogenesis and boundary with polygon-scanning multiscale photoacoustic microscopy. *Photoacoustics*, 26:100342, 2022.
- [112] Arie Krumholz, Lidai Wang, Junjie Yao, and Lihong V Wang. Functional photoacoustic microscopy of diabetic vasculature. *Journal of Biomedical Optics*, 17(6):060502–060502, 2012.
- [113] Hui-Chao Zhou, Ningbo Chen, Huangxuan Zhao, Tinghui Yin, Jianhui Zhang, Wei Zheng, Liang Song, Chengbo Liu, and Rongqin Zheng. Optical-resolution photoacoustic microscopy for monitoring vascular normalization during anti-angiogenic therapy. *Photoacoustics*, 15:100143, 2019.
- [114] Van Phuc Nguyen, Wei Qian, Yanxiu Li, Bing Liu, Michael Aaberg, Jessica Henry, Wei Zhang, Xueding Wang, and Yannis M Paulus. Chain-like gold nanoparticle clusters for multimodal photoacoustic microscopy and optical coherence tomography enhanced molecular imaging. *Nature Communications*, 12(1):34, 2021.

-
- [115] Paul Wrede, Oleksiy Degtyaruk, Sandeep Kumar Kalva, Xosé Luis Deán-Ben, Ugur Bozuyuk, Amirreza Aghakhani, Birgul Akolpoglu, Metin Sitti, and Daniel Razansky. Real-time 3D optoacoustic tracking of cell-sized magnetic microrobots circulating in the mouse brain vasculature. *Science Advances*, 8(19):eabm9132, 2022.
- [116] Da-Kang Yao, Konstantin Maslov, Kirk K Shung, Qifa Zhou, and Lihong V Wang. In vivo label-free photoacoustic microscopy of cell nuclei by excitation of DNA and RNA. *Optics Letters*, 35(24):4139–4141, 2010.
- [117] Da-Kang Yao, Ruimin Chen, Konstantin Maslov, Qifa Zhou, and Lihong V Wang. Optimal ultraviolet wavelength for in vivo photoacoustic imaging of cell nuclei. *Journal of Biomedical Optics*, 17(5):056004–056004, 2012.
- [118] Jacob Staley, Patrick Grogan, Abbas K Samadi, Huizhong Cui, Mark S Cohen, and Xinmai Yang. Growth of melanoma brain tumors monitored by photoacoustic microscopy. *Journal of Biomedical Optics*, 15(4):040510–040510, 2010.
- [119] Xiao Shu, Hao Li, Biqin Dong, Cheng Sun, and Hao F Zhang. Quantifying melanin concentration in retinal pigment epithelium using broadband photoacoustic microscopy. *Biomedical Optics Express*, 8(6):2851–2865, 2017.
- [120] Manoj K Dasa, Gianni Nteroli, Patrick Bowen, Giulia Messa, Yuyang Feng, Christian R Petersen, Stella Koutsikou, Magalie Bondu, Peter M Moselund, Adrian Podoleanu, Adrian Bradu, Christos Markos, and Ole Bang. All-fibre supercontinuum laser for in vivo multispectral photoacoustic microscopy of lipids in the extended near-infrared region. *Photoacoustics*, 18:100163, 2020.
- [121] Joo Yong Sim, Chang-Geun Ahn, Eun-Ju Jeong, and Bong Kyu Kim. In vivo microscopic photoacoustic spectroscopy for non-invasive glucose monitoring in-vulnerable to skin secretion products. *Scientific Reports*, 8(1):1059, 2018.
- [122] Zhun Xu, Changhui Li, and Lihong V Wang. Photoacoustic tomography of water in phantoms and tissue. *Journal of Biomedical Optics*, 15(3):036019–036019, 2010.
- [123] Jan Laufer, Clare Elwell, Dave Delpy, and Paul Beard. In vitro measurements of absolute blood oxygen saturation using pulsed near-infrared photoacoustic spectroscopy: accuracy and resolution. *Physics in Medicine & Biology*, 50(18):4409, 2005.

REFERENCES

- [124] Hao F Zhang, Konstantin Maslov, Mathangi Sivaramakrishnan, Gheorghe Stoica, and Lihong V Wang. Imaging of hemoglobin oxygen saturation variations in single vessels in vivo using photoacoustic microscopy. *Applied Physics Letters*, 90(5):053901, 2007.
- [125] Erich W Stein, Konstantin Maslov, and Lihong V Wang. Noninvasive, in vivo imaging of blood-oxygenation dynamics within the mouse brain using photoacoustic microscopy. *Journal of Biomedical Optics*, 14(2):020502–020502, 2009.
- [126] Junjie Yao, Lidai Wang, Joon-Mo Yang, Konstantin I Maslov, Terence TW Wong, Lei Li, Chih-Hsien Huang, Jun Zou, and Lihong V Wang. High-speed label-free functional photoacoustic microscopy of mouse brain in action. *Nature Methods*, 12(5):407–410, 2015.
- [127] Bo Ning, Matthew J Kennedy, Adam J Dixon, Naidi Sun, Rui Cao, Brian T Soetikno, Ruimin Chen, Qifa Zhou, K Kirk Shung, John A Hossack, and Song Hu. Simultaneous photoacoustic microscopy of microvascular anatomy, oxygen saturation, and blood flow. *Optics Letters*, 40(6):910–913, 2015.
- [128] Fei Cao, Zhihai Qiu, Huanhao Li, and Puxiang Lai. Photoacoustic imaging in oxygen detection. *Applied Sciences*, 7(12):1262, 2017.
- [129] Scott Prahl. Tabulated molar extinction coefficient for hemoglobin in water. <http://omlc.ogi.edu/spectra/hemoglobin/summary.html>, 1998. [Online; accessed 26-April-2023].
- [130] Mucong Li, Yuqi Tang, and Junjie Yao. Photoacoustic tomography of blood oxygenation: a mini review. *Photoacoustics*, 10:65–73, 2018.
- [131] Amos Danielli, Christopher P Favazza, Konstantin Maslov, and Lihong V Wang. Single-wavelength functional photoacoustic microscopy in biological tissue. *Optics Letters*, 36(5):769–771, 2011.
- [132] Zijian Guo, Song Hu, and Lihong V Wang. Calibration-free absolute quantification of optical absorption coefficients using acoustic spectra in 3D photoacoustic microscopy of biological tissue. *Optics Letters*, 35(12):2067–2069, 2010.
- [133] Zijian Guo, Christopher P Favazza, Alejandro Garcia-Uribe, and Lihong V Wang. Quantitative photoacoustic microscopy of optical absorption coefficients from acoustic spectra in the optical diffusive regime. *Journal of Biomedical Optics*, 17(6):066011, 2012.

-
- [134] Thomas Kirchner, Janek Gröhl, and Lena Maier-Hein. Context encoding enables machine learning-based quantitative photoacoustics. *Journal of Biomedical Optics*, 23(5):056008, 2018.
- [135] Stratis Tzoumas, Antonio Nunes, Ivan Olefir, Stefan Stangl, Panagiotis Symvoulidis, Sarah Glasl, Christine Bayer, Gabriele Multhoff, and Vasilis Ntzichristos. Eigenspectra optoacoustic tomography achieves quantitative blood oxygenation imaging deep in tissues. *Nature Communications*, 7(1):1–10, 2016.
- [136] Jun Xia, Amos Danielli, Yan Liu, Lidai Wang, Konstantin Maslov, and Lihong V Wang. Calibration-free quantification of absolute oxygen saturation based on the dynamics of photoacoustic signals. *Optics Letters*, 38(15):2800–2803, 2013.
- [137] Khalid Daoudi, Altaf Hussain, Erwin Hondebrink, and Wiendelt Steenbergen. Correcting photoacoustic signals for fluence variations using acousto-optic modulation. *Optics Express*, 20(13):14117–14129, 2012.
- [138] Hui Fang, Konstantin Maslov, and Lihong V Wang. Photoacoustic Doppler effect from flowing small light-absorbing particles. *Physical Review Letters*, 99(18):184501, 2007.
- [139] Ruiying Zhang, Junjie Yao, Konstantin I Maslov, and Lihong V Wang. Structured-illumination photoacoustic Doppler flowmetry of axial flow in homogeneous scattering media. *Applied Physics Letters*, 103(9):094101, 2013.
- [140] Junjie Yao, Rebecca C Gilson, Konstantin I Maslov, Lidai Wang, and Lihong V Wang. Calibration-free structured-illumination photoacoustic flowgraphy of transverse flow in scattering media. *Journal of Biomedical Optics*, 19(4):046007–046007, 2014.
- [141] Hui Fang and Lihong V Wang. M-mode photoacoustic particle flow imaging. *Optics Letters*, 34(5):671–673, 2009.
- [142] Sung-Liang Chen, Tao Ling, Sheng-Wen Huang, Hyung Won Baac, and L Jay Guo. Photoacoustic correlation spectroscopy and its application to low-speed flow measurement. *Optics Letters*, 35(8):1200–1202, 2010.
- [143] Junjie Yao, Konstantin I Maslov, Yunfei Shi, Larry A Taber, and Lihong V Wang. In vivo photoacoustic imaging of transverse blood flow by using Doppler broadening of bandwidth. *Optics Letters*, 35(9):1419–1421, 2010.

REFERENCES

- [144] Sung-Liang Chen, Zhixing Xie, Paul L Carson, Xueding Wang, and L Jay Guo. In vivo flow speed measurement of capillaries by photoacoustic correlation spectroscopy. *Optics Letters*, 36(20):4017–4019, 2011.
- [145] Jian Wei Tay, Jinyang Liang, and Lihong V Wang. Amplitude-masked photoacoustic wavefront shaping and application in flowmetry. *Optics Letters*, 39(19):5499–5502, 2014.
- [146] Pai-Chi Li, Sheng-Wen Huang, Chen-Wei Wei, Ya-Chin Chiou, Cheng-Dah Chen, and Chung-Ren Chris Wang. Photoacoustic flow measurements by use of laser-induced shape transitions of gold nanorods. *Optics Letters*, 30(24):3341–3343, 2005.
- [147] Chen-Wei Wei, Sheng-Wen Huang, Chung-Ren Chris Wang, and Pai-Chi Li. Photoacoustic flow measurements based on wash-in analysis of gold nanorods. *IEEE Transactions on Ultrasonics, Ferroelectrics, and Frequency Control*, 54(6):1131–1141, 2007.
- [148] Adi Sheinfeld and Avishay Eyal. Photoacoustic thermal diffusion flowmetry. *Biomedical Optics Express*, 3(4):800–813, 2012.
- [149] Lidai Wang, Junjie Yao, Konstantin I Maslov, Wenxin Xing, and Lihong V Wang. Ultrasound-heated photoacoustic flowmetry. *Journal of Biomedical Optics*, 18(11):117003–117003, 2013.
- [150] Chao Liu, Yizhi Liang, and Lidai Wang. Single-shot photoacoustic microscopy of hemoglobin concentration, oxygen saturation, and blood flow in sub-microseconds. *Photoacoustics*, 17:100156, 2020.
- [151] Chao Liu, Jiangbo Chen, Yachao Zhang, Jingyi Zhu, and Lidai Wang. Five-wavelength optical-resolution photoacoustic microscopy of blood and lymphatic vessels. *Advanced Photonics*, 3(1):016002, 2021.
- [152] Wei Song, Wenzhong Liu, and Hao F Zhang. Laser-scanning Doppler photoacoustic microscopy based on temporal correlation. *Applied Physics Letters*, 102(20):203501, 2013.
- [153] Fenghe Zhong, Youwei Bao, Ruimin Chen, Qifa Zhou, and Song Hu. High-speed wide-field multi-parametric photoacoustic microscopy. *Optics Letters*, 45(10):2756–2759, 2020.

-
- [154] Yiming Wang, Fenghe Zhong, Naidi Sun, Zhiqiang Xu, Jun Li, Quan Liu, Zhengying Li, Zhiyi Zuo, and Song Hu. High-speed multi-parametric photoacoustic microscopy of cerebral hemodynamic and metabolic responses to acute hemodilution. *Optics Letters*, 47(8):1988–1991, 2022.
- [155] James A Guggenheim, Jing Li, Thomas J Allen, Richard J Colchester, Sacha Noimark, Olumide Ogunlade, Ivan P Parkin, Ioannis Papakonstantinou, Adrien E Desjardins, Edward Z Zhang, and Paul C Beard. Ultrasensitive plano-concave optical microresonators for ultrasound sensing. *Nature Photonics*, 11(11):714–719, 2017.
- [156] Ting Feng, Qiaochu Li, Cheng Zhang, Guan Xu, L Jay Guo, Jie Yuan, and Xueding Wang. Characterizing cellular morphology by photoacoustic spectrum analysis with an ultra-broadband optical ultrasonic detector. *Optics Express*, 24(17):19853–19862, 2016.
- [157] Elias Blumenröther, Oliver Melchert, Jonas Kanngießer, Merve Wollweber, and Bernhard Roth. Single transparent piezoelectric detector for optoacoustic sensing—design and signal processing. *Sensors*, 19(9):2195, 2019.
- [158] Haoyang Chen, Sumit Agrawal, Ajay Dangi, Christopher Wible, Mohamed Osman, Lidya Abune, Huizhen Jia, Randall Rossi, Yong Wang, and Sri-Rajasekhar Kothapalli. Optical-resolution photoacoustic microscopy using transparent ultrasound transducer. *Sensors*, 19(24):5470, 2019.
- [159] Jeongwoo Park, Byullee Park, Taeyeong Kim, Donghyun Lee, Uijung Yong, Jinah Jang, Unyong Jeong, Hyung Ham Kim, and Chulhong Kim. Seamlessly integrated optical and acoustical imaging systems through transparent ultrasonic transducer. In *Photons Plus Ultrasound: Imaging and Sensing 2020*, volume 11240, pages 69–74. SPIE, 2020.
- [160] Cheng Fang, He Hu, and Jun Zou. A focused optically transparent PVDF transducer for photoacoustic microscopy. *IEEE Sensors Journal*, 20(5):2313–2319, 2019.
- [161] Ruimin Chen, Yun He, Junhui Shi, Christopher Yung, Jeeseong Hwang, Lihong V Wang, and Qifa Zhou. Transparent high-frequency ultrasonic transducer for photoacoustic microscopy application. *IEEE Transactions on Ultrasonics, Ferroelectrics, and Frequency Control*, 67(9):1848–1853, 2020.

REFERENCES

- [162] Saher M Maswadi, Bennett L Ibey, Caleb C Roth, Dmitri A Tsyboulski, Hope T Beier, Randolph D Glickman, and Alexander A Oraevsky. All-optical optoacoustic microscopy based on probe beam deflection technique. *Photoacoustics*, 4(3):91–101, 2016.
- [163] Xiaoyi Zhu, Zhiyu Huang, Guohe Wang, Wenzhao Li, Da Zou, and Changhui Li. Ultrasonic detection based on polarization-dependent optical reflection. *Optics Letters*, 42(3):439–441, 2017.
- [164] Amir Rosenthal, Daniel Razansky, and Vasilis Ntziachristos. High-sensitivity compact ultrasonic detector based on a pi-phase-shifted fiber Bragg grating. *Optics Letters*, 36(10):1833–1835, 2011.
- [165] Adam Maxwell, Sheng-Wen Huang, Tao Ling, Jin-Sung Kim, Shai Ashkenazi, and L Jay Guo. Polymer microring resonators for high-frequency ultrasound detection and imaging. *IEEE Journal of Selected Topics in Quantum Electronics*, 14(1):191–197, 2008.
- [166] Cheng Zhang, Sung-Liang Chen, Tao Ling, and L Jay Guo. Review of imprinted polymer microrings as ultrasound detectors: Design, fabrication, and characterization. *IEEE Sensors Journal*, 15(6):3241–3248, 2015.
- [167] Thomas J Allen, Olumide Ogunlade, Edward Zhang, and Paul C Beard. Large area laser scanning optical resolution photoacoustic microscopy using a fibre optic sensor. *Biomedical Optics Express*, 9(2):650–660, 2018.
- [168] Shai Ashkenazi, Yang Hou, Takashi Buma, and Matthew O’Donnell. Optoacoustic imaging using thin polymer etalon. *Applied Physics Letters*, 86(13):134102, 2005.
- [169] Stefan Preisser, Wolfgang Rohringer, Mengyang Liu, Christian Kollmann, Stefan Zotter, Balthasar Fischer, and Wolfgang Drexler. All-optical highly sensitive aknetic sensor for ultrasound detection and photoacoustic imaging. *Biomedical Optics Express*, 7(10):4171–4186, 2016.
- [170] Jens Buchmann, James Guggenheim, Edward Zhang, Chris Scharfenorth, Bastian Spannekrebs, Claus Villringer, and Jan Laufer. Characterization and modeling of Fabry–Perot ultrasound sensors with hard dielectric mirrors for photoacoustic imaging. *Applied Optics*, 56(17):5039–5046, 2017.

-
- [171] Guangyao Li, Zhendong Guo, and Sung-Liang Chen. Miniature all-optical probe for large synthetic aperture photoacoustic-ultrasound imaging. *Optics Express*, 25(21):25023–25035, 2017.
- [172] Rehman Ansari, Edward Z Zhang, Adrien E Desjardins, and Paul C Beard. All-optical forward-viewing photoacoustic probe for high-resolution 3D endoscopy. *Light: Science & Applications*, 7(1):75, 2018.
- [173] Bohua Chen, Yuwen Chen, and Cheng Ma. Photothermally tunable Fabry-Pérot fiber interferometer for photoacoustic mesoscopy. *Biomedical Optics Express*, 11(5):2607–2618, 2020.
- [174] Biqin Dong, Cheng Sun, and Hao F Zhang. Optical detection of ultrasound in photoacoustic imaging. *IEEE Transactions on Biomedical Engineering*, 64(1):4–15, 2016.
- [175] Edward Z Zhang, Jan Laufer, Boris Považay, Aneesh Alex, Bernd Hofer, Wolfgang Drexler, and Paul Beard. Multimodal simultaneous photoacoustic tomography, optical resolution microscopy, and OCT system. In *Photons Plus Ultrasound: Imaging and Sensing 2010*, volume 7564, pages 205–211. SPIE, 2010.
- [176] Edward Z Zhang, Boris Povazay, Jan Laufer, Aneesh Alex, Bernd Hofer, Barbara Pedley, Carl Glittenberg, Bradley Treeby, Ben Cox, Paul Beard, and Wolfgang Drexler. Multimodal photoacoustic and optical coherence tomography scanner using an all optical detection scheme for 3D morphological skin imaging. *Biomedical Optics Express*, 2(8):2202–2215, 2011.
- [177] Richard Haindl, Abigail J Deloria, Caterina Sturtzel, Harald Sattmann, Wolfgang Rohringer, Balthasar Fischer, Marco Andreana, Angelika Unterhuber, Thorsten Schwerte, Martin Distel, Wolfgang Drexler, Rainer Leitgeb, and Mengyang Liu. Functional optical coherence tomography and photoacoustic microscopy imaging for zebrafish larvae. *Biomedical Optics Express*, 11(4):2137–2151, 2020.
- [178] Sung-Liang Chen, Zhixing Xie, L Jay Guo, and Xueding Wang. A fiber-optic system for dual-modality photoacoustic microscopy and confocal fluorescence microscopy using miniature components. *Photoacoustics*, 1(2):30–35, 2013.
- [179] Biqin Dong, Hao Li, Zhen Zhang, Kevin Zhang, Siyu Chen, Cheng Sun, and Hao F Zhang. Isometric multimodal photoacoustic microscopy based on optically transparent micro-ring ultrasonic detection. *Optica*, 2(2):169–176, 2015.

REFERENCES

- [180] Edward Zhang, Jan Laufer, and Paul Beard. Backward-mode multiwavelength photoacoustic scanner using a planar Fabry-Perot polymer film ultrasound sensor for high-resolution three-dimensional imaging of biological tissues. *Applied Optics*, 47(4):561–577, 2008.
- [181] Amit P Jathoul, Jan Laufer, Olumide Ogunlade, Bradley Treeby, Ben Cox, Edward Zhang, Peter Johnson, Arnold R Pizzey, Brian Philip, Teresa Marafioti, Mark F Lythgoe, R Barbara Pedley, Martin A Pule, and Paul Beard. Deep in vivo photoacoustic imaging of mammalian tissues using a tyrosinase-based genetic reporter. *Nature Photonics*, 9(4):239–246, 2015.
- [182] Jan Laufer, Francesca Norris, Jon Cleary, Edward Zhang, Bradley Treeby, Ben Cox, Peter Johnson, Pete Scambler, Mark Lythgoe, and Paul Beard. In vivo photoacoustic imaging of mouse embryos. *Journal of Biomedical Optics*, 17(6):061220–061220, 2012.
- [183] Jan Laufer, Peter Johnson, Edward Zhang, Bradley Treeby, Ben Cox, Barbara Pedley, and Paul Beard. In vivo preclinical photoacoustic imaging of tumor vasculature development and therapy. *Journal of Biomedical Optics*, 17(5):056016–056016, 2012.
- [184] Jens Buchmann, Bernhard Kaplan, Samuel Powell, Steffen Prohaska, and Jan Laufer. Quantitative PA tomography of high resolution 3-D images: experimental validation in a tissue phantom. *Photoacoustics*, 17:100157, 2020.
- [185] Sibylle Gratt, Gerhild Wurzinger, Robert Nuster, and Guenther Paltauf. Free beam Fabry-Perot-interferometer as detector for photoacoustic tomography. In *European Conference on Biomedical Optics*, page 880002. Optica Publishing Group, 2013.
- [186] James A Guggenheim, Jing Li, Edward Z Zhang, and Paul C Beard. Frequency response and directivity of highly sensitive optical microresonator detectors for photoacoustic imaging. In *Photons Plus Ultrasound: Imaging and Sensing 2015*, volume 9323, pages 197–202. SPIE, 2015.
- [187] James A Guggenheim, Edward Z Zhang, and Paul C Beard. A method for measuring the directional response of ultrasound receivers in the range 0.3–80 MHz using a laser-generated ultrasound source. *IEEE Transactions on Ultrasonics, Ferroelectrics, and Frequency Control*, 64(12):1857–1863, 2017.

-
- [188] Dylan M Marques, James A Guggenheim, Rehman Ansari, Edward Z Zhang, Paul C Beard, and Peter RT Munro. Probing the optical readout characteristics of Fabry-Perot ultrasound sensors through realistic modelling. In *European Conference on Biomedical Optics*, page 11077_16. Optica Publishing Group, 2019.
- [189] Dylan M Marques, James A Guggenheim, Rehman Ansari, Edward Z Zhang, Paul C Beard, and Peter RT Munro. Modelling Fabry-Pérot etalons illuminated by focussed beams. *Optics Express*, 28(5):7691–7706, 2020.
- [190] Volker Wilkens. Characterization of an optical multilayer hydrophone with constant frequency response in the range from 1 to 75 MHz. *The Journal of the Acoustical Society of America*, 113(3):1431–1438, 2003.
- [191] Benjamin T Cox and Paul C Beard. The frequency-dependent directivity of a planar Fabry-Perot polymer film ultrasound sensor. *IEEE Transactions on Ultrasonics, Ferroelectrics, and Frequency Control*, 54(2):394–404, 2007.
- [192] Danny R Ramasawmy, Eleanor Martin, James A Guggenheim, Edward Z Zhang, Paul C Beard, Bradley E Treeby, and Ben T Cox. Analysis of the directivity of glass-Etalon Fabry-Pérot ultrasound sensors. *IEEE Transactions on Ultrasonics, Ferroelectrics, and Frequency Control*, 66(9):1504–1513, 2019.
- [193] Alexander Franzen. ComponentLibrary. <https://www.gwoptics.org/ComponentLibrary/>, 2009. [Online; accessed 26-April-2023].
- [194] Elisabeth Baumann, Ulrike Pohle, Edward Zhang, Thomas Allen, Claus Villringer, Silvio Pulwer, Holger Gerhardt, and Jan Laufer. A backward-mode optical-resolution photoacoustic microscope for 3D imaging using a planar Fabry-Pérot sensor. *Photoacoustics*, 24:100293, 2021.
- [195] Guido Van Rossum and Fred L. Drake. *Python 3 Reference Manual*. CreateSpace, Scotts Valley, CA, 2009.
- [196] Paul C Beard, Frederic Perennes, and Tim N Mills. Transduction mechanisms of the Fabry-Perot polymer film sensing concept for wideband ultrasound detection. *IEEE Transactions on Ultrasonics, Ferroelectrics, and Frequency Control*, 46(6):1575–1582, 1999.
- [197] Paul C Beard, Andrew M Hurrell, and Tim N Mills. Characterization of a polymer film optical fiber hydrophone for use in the range 1 to 20 MHz: A comparison with

REFERENCES

- PVDF needle and membrane hydrophones. *IEEE Transactions on Ultrasonics, Ferroelectrics, and Frequency Control*, 47(1):256–264, 2000.
- [198] Zeon. Safety Data Sheet for Zeonex 480R. https://www.zeonsmi.com/pdf/Zeonex_480R_Zeon_US_SDS_27Sept2019.pdf, 2019. [Online; accessed 28-April-2023].
- [199] Ulrike Pohle, Elisabeth Baumann, Silvio Pulwer, Claus Villringer, Edward Zhang, Holger Gerhardt, and Jan Laufer. Development of a backward-mode photoacoustic microscope using a Fabry-Pérot sensor. In *Photons Plus Ultrasound: Imaging and Sensing 2019*, volume 10878, pages 594–598. SPIE, 2019.
- [200] Peter Aleström, Livia D’Angelo, Paul J Midtlyng, Daniel F Schorderet, Stefan Schulte-Merker, Frederic Sohm, and Susan Warner. Zebrafish: Housing and husbandry recommendations. *Laboratory Animals*, 54(3):213–224, 2020.
- [201] Parsin Hajireza, Alexander Forbrich, and Roger Zemp. In-vivo functional optical-resolution photoacoustic microscopy with stimulated Raman scattering fiber-laser source. *Biomedical Optics Express*, 5(2):539–546, 2014.
- [202] Evan Evans and Yuan-Cheng Fung. Improved measurements of the erythrocyte geometry. *Microvascular Research*, 4(4):335–347, 1972.
- [203] Junjie Yao, Konstantin I Maslov, Yu Zhang, Younan Xia, and Lihong V Wang. Label-free oxygen-metabolic photoacoustic microscopy in vivo. *Journal of Biomedical Optics*, 16(7):076003, 2011.
- [204] Pu Wang, Teng Ma, Mikhail N Slipchenko, Shanshan Liang, Jie Hui, K Kirk Shung, Sukesh Roy, Michael Sturek, Qifa Zhou, Zhongping Chen, and Ji-Xin Cheng. High-speed intravascular photoacoustic imaging of lipid-laden atherosclerotic plaque enabled by a 2-kHz barium nitrite Raman laser. *Scientific Reports*, 4(1):1–7, 2014.
- [205] Rongkang Gao, Zhiqiang Xu, Yaguang Ren, Liang Song, and Chengbo Liu. Non-linear mechanisms in photoacoustics—powerful tools in photoacoustic imaging. *Photoacoustics*, 22:100243, 2021.
- [206] Paola Di Ninni, Fabrizio Martelli, and Giovanni Zaccanti. The use of india ink in tissue-simulating phantoms. *Optics Express*, 18(26):26854–26865, 2010.

-
- [207] Martina B Fonseca, Lu An, and Benjamin T Cox. Sulfates as chromophores for multiwavelength photoacoustic imaging phantoms. *Journal of Biomedical Optics*, 22(12):125007, 2017.
- [208] Wei Shi, Peng Shao, Parsin Hajireza, Alexander Forbrich, and Roger J Zemp. In vivo dynamic process imaging using real-time optical-resolution photoacoustic microscopy. *Journal of Biomedical Optics*, 18(2):026001, 2013.
- [209] Fenghe Zhong and Song Hu. Ultra-high-speed multi-parametric photoacoustic microscopy. *bioRxiv*, 2021.
- [210] Thomas A Pologruto, Bernardo L Sabatini, and Karel Svoboda. ScanImage: flexible software for operating laser scanning microscopes. *Biomedical Engineering Online*, 2(1):1–9, 2003.
- [211] Michael J Moore, Suzan El-Rass, Yongliang Xiao, Youdong Wang, Xiao-Yan Wen, and Michael C Kolios. Simultaneous ultra-high frequency photoacoustic microscopy and photoacoustic radiometry of zebrafish larvae in vivo. *Photoacoustics*, 12:14–21, 2018.
- [212] Lars Jakobsson, Katie Bentley, and Holger Gerhardt. VEGFRs and Notch: a dynamic collaboration in vascular patterning. *Biochemical Society Transactions*, 37(6):1233–1236, 2009.
- [213] Florian Milde, Stephanie Lauw, Petros Koumoutsakos, and M Luisa Iruela-Arispe. The mouse retina in 3D: quantification of vascular growth and remodeling. *Integrative Biology*, 5(12):1426–1438, 2013.
- [214] Claudia Prahst, Parham Ashrafzadeh, Thomas Mead, Ana Figueiredo, Karen Chang, Douglas Richardson, Lakshmi Venkaraman, Mark Richards, Ana Martins Russo, Kyle Harrington, Marie Ouarné, Andreia Pena, Dong Feng Chen, Lena Claesson-Welsh, Kin-Sang Cho, Claudio A Franco, and Katie Bentley. Mouse retinal cell behaviour in space and time using light sheet fluorescence microscopy. *Elife*, 9:e49779, 2020.
- [215] Javier Mazzaferri, Bruno Larrivé, Bertan Cakir, Przemyslaw Sapiha, and Santiago Costantino. A machine learning approach for automated assessment of retinal vasculature in the oxygen induced retinopathy model. *Scientific Reports*, 8(1):3916, 2018.

REFERENCES

- [216] Mohammad Haft-Javaherian, Linjing Fang, Victorine Muse, Chris B Schaffer, Nozomi Nishimura, and Mert R Sabuncu. Deep convolutional neural networks for segmenting 3D in vivo multiphoton images of vasculature in Alzheimer disease mouse models. *PLoS ONE*, 14(3):e0213539, 2019.
- [217] Giles Tetteh, Velizar Efremov, Nils D Forkert, Matthias Schneider, Jan Kirschke, Bruno Weber, Claus Zimmer, Marie Piraud, and Bjoern H Menze. Deepvessel-net: Vessel segmentation, centerline prediction, and bifurcation detection in 3-d angiographic volumes. *Frontiers in Neuroscience*, page 1285, 2020.
- [218] Xuelin Wang, Guofu Zhu, Shumin Wang, Jordan Rhen, Jinjiang Pang, and Zhengwu Zhang. Vessel tech: a high-accuracy pipeline for comprehensive mouse retinal vasculature characterization. *Angiogenesis*, 24:7–11, 2021.
- [219] Miguel O Bernabeu, Martin L Jones, Jens H Nielsen, Timm Krüger, Rupert W Nash, Derek Groen, Sebastian Schmieschek, James Hetherington, Holger Gerhardt, Claudio A Franco, and Peter V Coveney. Computer simulations reveal complex distribution of haemodynamic forces in a mouse retina model of angiogenesis. *Journal of The Royal Society Interface*, 11(99):20140543, 2014.
- [220] Miguel O Bernabeu, Martin L Jones, Rupert W Nash, Anna Pezzarossa, Peter V Coveney, Holger Gerhardt, and Claudio A Franco. PolNet: A tool to quantify network-level cell polarity and blood flow in vascular remodeling. *Biophysical Journal*, 114(9):2052–2058, 2018.
- [221] Pedro Barbacena, Maria Dominguez-Cejudo, Catarina G Fonseca, Manuel Gómez-González, Laura M Faure, Georgia Zarkada, Andreia Pena, Anna Pezzarossa, Daniela Ramalho, Ylenia Giarratano, Marie Ouarné, David Barata, Isabela C Fortunato, Lenka Henao Misikova, Ian Mauldin, Yulia Carvalho, Xavier Trepas, Pere Roca-Cusachs, Anne Eichmann, Miguel O Bernabeu, and Cláudio A Franco. Competition for endothelial cell polarity drives vascular morphogenesis in the mouse retina. *Developmental Cell*, 57(19):2321–2333, 2022.
- [222] Heon-Woo Lee, Yanying Xu, Liqun He, Woosung Choi, David Gonzalez, Suk-Won Jin, and Michael Simons. Role of venous endothelial cells in developmental and pathologic angiogenesis. *Circulation*, 144(16):1308–1322, 2021.
- [223] Yi Jin, Yindi Ding, Mark Richards, Mika Kaakinen, Wolfgang Giese, Elisabeth Baumann, Anna Szymborska, André Rosa, Sofia Nordling, Lilian Schimmel,

- Emir Bora Akmeriç, Andreia Pena, Emmanuel Nwadozi, Maria Jamalpour, Katrin Holstein, Miguel Sáinz-Jaspeado, Miguel O Bernabeu, Michael Welsh, Emma Gordon, Claudio A Franco, Dietmar Vestweber, Lauri Eklund, Holger Gerhardt, and Lena Claesson-Welsh. Tyrosine-protein kinase Yes controls endothelial junctional plasticity and barrier integrity by regulating VE-cadherin phosphorylation and endocytosis. *Nature Cardiovascular Research*, pages 1–18, 2022.
- [224] Benjamin Woods, Chun-Chen Kuo, Chi-Fang Wu, Trevin R Zyla, and Daniel J Lew. Polarity establishment requires localized activation of Cdc42. *Journal of Cell Biology*, 211(1):19–26, 2015.
- [225] Panos Kouklis, Maria Konstantoulaki, and Asrar B Malik. VE-cadherin-induced Cdc42 signaling regulates formation of membrane protrusions in endothelial cells. *Journal of Biological Chemistry*, 278(18):16230–16236, 2003.
- [226] Olivier Dormond, Alessandro Foletti, Cécile Paroz, and Curzio Rüegg. NSAIDs inhibit $\alpha V\beta 3$ integrin-mediated and Cdc42/Rac-dependent endothelial-cell spreading, migration and angiogenesis. *Nature Medicine*, 7(9):1041–1047, 2001.
- [227] Masahide Sakabe, Jieqing Fan, Yoshinobu Odaka, Ning Liu, Aishlin Hassan, Xin Duan, Paige Stump, Luke Byerly, Megan Donaldson, Jiukuan Hao, Marcus Fruttiger, Qing Richard Lu, Yi Zheng, Richard A Lang, and Mei Xin. YAP/TAZ-CDC42 signaling regulates vascular tip cell migration. *Proceedings of the National Academy of Sciences*, 114(41):10918–10923, 2017.
- [228] Sandrine Etienne-Manneville. Cdc42-the centre of polarity. *Journal of Cell Science*, 117(8):1291–1300, 2004.
- [229] David M Barry, Ke Xu, Stryder M Meadows, Yi Zheng, Pieter R Norden, George E Davis, and Ondine Cleaver. Cdc42 is required for cytoskeletal support of endothelial cell adhesion during blood vessel formation in mice. *Development*, 142(17):3058–3070, 2015.
- [230] Bàrbara Laviña, Marco Castro, Colin Niaudet, Bert Cruys, Alberto Álvarez-Aznar, Peter Carmeliet, Katie Bentley, Cord Brakebusch, Christer Betsholtz, and Konstantin Gaengel. Defective endothelial cell migration in the absence of Cdc42 leads to capillary-venous malformations. *Development*, 145(13):dev161182, 2018.

REFERENCES

- [231] Marco Castro, Bàrbara Laviña, Koji Ando, Alberto Álvarez-Aznar, Abdallah Abu Taha, Cord Brakebusch, Elisabetta Dejana, Christer Betsholtz, and Konstantin Gaengel. CDC42 deletion elicits cerebral vascular malformations via increased MEKK3-dependent KLF4 expression. *Circulation Research*, 124(8):1240–1252, 2019.
- [232] Wenfu Tan, Todd R Palmby, Julie Gavard, Panomwat Amornphimoltham, Yi Zheng, and J Silvio Gui. An essential role for Rac1 in endothelial cell function and vascular development. *The FASEB Journal*, 22(6):1829–1838, 2008.
- [233] Mandar Deepak Muzumdar, Bosiljka Tasic, Kazunari Miyamichi, Ling Li, and Liqun Luo. A global double-fluorescent cre reporter mouse. *Genesis*, 45(9):593–605, 2007.
- [234] Ines Martinez-Corral, Lukas Stanczuk, Maike Frye, Maria Helena Ulvmar, Rodrigo Diéguez-Hurtado, David Olmeda, Taija Makinen, and Sagrario Ortega. Vegfr3-CreER (T2) mouse, a new genetic tool for targeting the lymphatic system. *Angiogenesis*, 19:433–445, 2016.
- [235] Xunwei Wu, Fabio Quondamatteo, Tine Lefever, Aleksandra Czuchra, Hannelore Meyer, Anna Chrostek, Ralf Paus, Lutz Langbein, and Cord Brakebusch. Cdc42 controls progenitor cell differentiation and β -catenin turnover in skin. *Genes & Development*, 20(5):571–585, 2006.
- [236] Anna Chrostek, Xunwei Wu, Fabio Quondamatteo, Rong Hu, Anna Sanecka, Catherin Niemann, Lutz Langbein, Ingo Haase, and Cord Brakebusch. Rac1 is crucial for hair follicle integrity but is not essential for maintenance of the epidermis. *Molecular and Cellular Biology*, 26(18):6957–6970, 2006.
- [237] Filipa Neto, Alexandra Klaus-Bergmann, Yu Ting Ong, Silvanus Alt, Anne-Clemence Vion, Anna Szymborska, Joana R Carvalho, Irene Hollfinger, Eireen Bartels-Klein, Claudio A Franco, Michael Potente, and Holger Gerhardt. YAP and TAZ regulate adherens junction dynamics and endothelial cell distribution during vascular development. *Elife*, 7:e31037, 2018.
- [238] Johannes Schindelin, Ignacio Arganda-Carreras, Erwin Frise, Verena Kaynig, Mark Longair, Tobias Pietzsch, Stephan Preibisch, Curtis Rueden, Stephan Saalfeld, Benjamin Schmid, Jean-Yves Tinevez, Daniel J White, Volker Hartenstein, Kevin Eliceiri, Pavel Tomancak, and Albert Cardona. Fiji: an open-source platform for biological image analysis. *Nature Methods*, 9(7):676–682, 2012.

-
- [239] Sajid Alam, Nok Lam Chan, Gabriel Comym, Yetunde Dada, Ivan Danov, Deepyaman Datta, Tynan DeBold, Lim Hoang, Rashida Kanchwala, Andrew Mackay, Ahdra Merali, Antony Milne, Cvetanka Nechevska, Huong Nguyen, Nero Okwa, Joel Schwarzmam, and Merel Theisen. Kedro, 9 2022.
- [240] Wolfgang Giese*, Andre Rosa*, Elisabeth Baumann, Olya Oppenheim, Emir Bora Akmeriç, Santiago Andrade, Irene Hollfinger, Silvanus Alt, and Holger Gerhardt. Reconstructing stochastic cell population trajectories reveals regulators and heterogeneity of endothelial flow-migration coupling driving vascular remodelling. *bioRxiv*, pages 2023–05, 2023.
- [241] Jonathan Stone, Ahuva Itin, Tamar Alon, Jacob Pe’Er, Hadassah Gnessin, Tailoi Chan-Ling, and Eli Keshet. Development of retinal vasculature is mediated by hypoxia-induced vascular endothelial growth factor (VEGF) expression by neuroglia. *Journal of Neuroscience*, 15(7):4738–4747, 1995.
- [242] Cong Xu, Sana S Hasan, Inga Schmidt, Susana F Rocha, Mara E Pitulescu, Jeroen Bussmann, Dana Meyen, Erez Raz, Ralf H Adams, and Arndt F Siekmann. Arteries are formed by vein-derived endothelial tip cells. *Nature Communications*, 5(1):5758, 2014.

Eidesstattliche Versicherung

„Ich, Elisabeth Baumann, versichere an Eides statt durch meine eigenhändige Unterschrift, dass ich die vorgelegte Dissertation mit dem Thema: Connecting Endothelial Behavior and Hemodynamics – Method Development for Preclinical Optical Imaging of the Vasculature/Verknüpfung von Endothelverhalten und Hämodynamik – Methodenentwicklung für die präklinische optische Bildgebung des Blutgefäßsystems selbstständig und ohne nicht offengelegte Hilfe Dritter verfasst und keine anderen als die angegebenen Quellen und Hilfsmittel genutzt habe.

Alle Stellen, die wörtlich oder dem Sinne nach auf Publikationen oder Vorträgen anderer Autoren/innen beruhen, sind als solche in korrekter Zitierung kenntlich gemacht. Die Abschnitte zu Methodik (insbesondere praktische Arbeiten, Laborbestimmungen, statistische Aufarbeitung) und Resultaten (insbesondere Abbildungen, Graphiken und Tabellen) werden von mir verantwortet.

Ich versichere ferner, dass ich die in Zusammenarbeit mit anderen Personen generierten Daten, Datenauswertungen und Schlussfolgerungen korrekt gekennzeichnet und meinen eigenen Beitrag sowie die Beiträge anderer Personen korrekt kenntlich gemacht habe (siehe Anteilserklärung). Texte oder Textteile, die gemeinsam mit anderen erstellt oder verwendet wurden, habe ich korrekt kenntlich gemacht.

Meine Anteile an etwaigen Publikationen zu dieser Dissertation entsprechen denen, die in der untenstehenden gemeinsamen Erklärung mit dem/der Erstbetreuer/in, angegeben sind. Für sämtliche im Rahmen der Dissertation entstandenen Publikationen wurden die Richtlinien des ICMJE (International Committee of Medical Journal Editors; www.icmje.org) zur Autorenschaft eingehalten. Ich erkläre ferner, dass ich mich zur Einhaltung der Satzung der Charité – Universitätsmedizin Berlin zur Sicherung Guter Wissenschaftlicher Praxis verpflichte.

Weiterhin versichere ich, dass ich diese Dissertation weder in gleicher noch in ähnlicher Form bereits an einer anderen Fakultät eingereicht habe.

Die Bedeutung dieser eidesstattlichen Versicherung und die strafrechtlichen Folgen einer

B. EIDESSTATTLICHE VERSICHERUNG

unwahren eidesstattlichen Versicherung (§§156, 161 des Strafgesetzbuches) sind mir bekannt und bewusst.“

Datum

Unterschrift

Anteilserklärung an erfolgten Publikationen

Elisabeth Baumann hatte folgenden Anteil an den folgenden Publikationen:

Publikation 1: **Elisabeth Baumann**, Ulrike Pohle, Edward Zhang, Thomas Allen, Claus Villringer, Silvio Pulwer, Holger Gerhardt and Jan Laufer. A backward-mode optical-resolution photoacoustic microscope for 3D imaging using a planar Fabry-Pérot sensor. *Photoacoustics*, 24:100293, 2021.

Beitrag im Einzelnen: Elisabeth Baumann hat Experimente geplant, durchgeführt und ausgewertet, Software entwickelt und angepasst, Abbildungen erstellt, die erste Version des Manuskripts geschrieben und Revisionsarbeiten durchgeführt.

Publikation 2: Yi Jin, Yindi Ding, Mark Richards, Mika Kaakinen, Wolfgang Giese, **Elisabeth Baumann**, Anna Szymborska, André Rosa, Sofia Nordling, Lilian Schimmel, Emir Bora Akmeriç, Andreia Pena, Emmanuel Nwadozi, Maria Jamalpour, Katrin Holstein, Miguel Sáinz-Jaspeado, Miguel O. Bernabeu, Michael Welsh, Emma Gordon, Claudio A. Franco, Dietmar Vestweber, Lauri Eklund, Holger Gerhardt and Lena Claesson-Welsh. Tyrosine-protein kinase Yes controls endothelial junctional plasticity and barrier integrity by regulating VE-cadherin phosphorylation and endocytosis. *Nature Cardiovascular Research*, 1:1156–1173, 2022.

Beitrag im Einzelnen: Elisabeth Baumann analysierte *in vivo* Bilddaten und las das Manuskript Korrektur. Aus ihrer Analyse sind Abbildung 3c, 3d und 3f entstanden.

Weitere Ausführungen über Elisabeth Baumanns Beitrag und den Beitrag anderer Personen zu den relevanten Projekten befinden sich auf Seite 25 f. bzw. 83 f. dieser Dissertation.

Unterschrift, Datum und Stempel des erstbetreuenden Hochschullehrers

Unterschrift der Doktorandin

List of Publications

Peer-reviewed journal publications relevant for the work presented in the dissertation

1. **Elisabeth Baumann**, Ulrike Pohle, Edward Zhang, Thomas Allen, Claus Villringer, Silvio Pulwer, Holger Gerhardt, and Jan Laufer. A backward-mode optical-resolution photoacoustic microscope for 3D imaging using a planar Fabry-Pérot sensor. *Photoacoustics*, 24:100293, 2021.
2. Yi Jin, Yindi Ding, Mark Richards, Mika Kaakinen, Wolfgang Giese, **Elisabeth Baumann**, Anna Szymborska, André Rosa, Sofia Nordling, Lilian Schimmel, Emir Bora Akmeriç, Andreia Pena, Emmanuel Nwadozi, Maria Jamalpour, Katrin Holstein, Miguel Sáinz-Jaspeado, Miguel O. Bernabeu, Michael Welsh, Emma Gordon, Claudio A. Franco, Dietmar Vestweber, Lauri Eklund, Holger Gerhardt, and Lena Claesson-Welsh. Tyrosine-protein kinase Yes controls endothelial junctional plasticity and barrier integrity by regulating VE-cadherin phosphorylation and endocytosis. *Nature Cardiovascular Research*, 1:1156–1173, 2022.

Relevant preprints

1. Wolfgang Giese*, André Rosa*, **Elisabeth Baumann**, Olya Oppenheim, Emir Bora Akmeriç, Santiago Andrade, Irene Hollfinger, Silvanus Alt, and Holger Gerhardt. Reconstructing stochastic cell population trajectories reveals regulators and heterogeneity of endothelial flow-migration coupling driving vascular remodelling. *bioRxiv*, 2023.

Other publications

1. Lise Finotto, Basiel Cole, Wolfgang Giese, **Elisabeth Baumann**, Annelies Claeys, Maxime Vanmechelen, Brecht Decraene, Marleen Derweduwe, Nikolina Dubroja Lakic, Gautam Shankar, Madhu Nagathihalli Kantharaju, Jan Albrecht, Ilse Geudens, Fabio Stanchi, Keith Ligon, Bram Boeckx, Diether Lambrechts, Kyle Harrington, Ludo Van Den Bosch, Steven De Vleeschouwer, Frederik De Smet, and Holger Gerhardt. Single-cell profiling and zebrafish avatars reveal LGALS1 as immunomodulating target in glioblastoma. *Submitted Manuscript*, 2023.

Conference contributions

1. **Elisabeth Baumann**, Ulrike Pohle, Thomas Allen, Holger Gerhardt, and Jan Laufer. A backward-mode optical-resolution photoacoustic microscope for functional 3D imaging. *DPG Frühjahrstagung SKM 2023*, Dresden, Germany.
2. **Elisabeth Baumann**, Ulrike Pohle, Thomas Allen, Edward Zhang, Holger Gerhardt, and Jan Laufer. Backward-mode optical-resolution photoacoustic microscope for functional imaging using a planar Fabry-Pérot ultrasound sensor. *SPIE Photonics West 2020*, San Francisco, USA.
3. Ulrike Pohle, **Elisabeth Baumann**, Silvio Pulwer, Claus Villringer, Edward Zhang, Holger Gerhardt, and Jan Laufer. Development of a backward-mode photoacoustic microscope using a Fabry-Pérot sensor. In *Photons Plus Ultrasound: Imaging and Sensing 2019*, volume 10878, pages 594–598. SPIE, 2019.
4. **Elisabeth Baumann**, Lucy A. E. Matthews, Anthony Traboulsee, Jacqueline Palace, and Shannon Kolind. Does white matter, grey matter or lesion multi-component relaxation differ between neuromyelitis optica and multiple sclerosis brain? *International Society for Magnetic Resonance in Medicine (ISMRM) 22nd Scientific Meeting and Exhibition 2014*, Milan, Italy.

Acknowledgements

To my thesis supervisor Holger Gerhardt, for giving me this opportunity to grow as a scientist and hopefully also as a person. Like any PhD journey, this one was a roller coaster ride but I felt like I always had your trust to be curious, to do what I thought was right, and most importantly, just be myself. Thank you for promoting such a safe atmosphere in the lab. Thank you also for sharing great writing playlists with me (although I do admit that I hope I will not need them again anytime soon).

To my co-supervisor Jan Laufer. Thank you for welcoming me into your group in Halle and for always supporting me and my science. It was great to have such an approachable supervisor who allowed me to develop my personal playground at the MDC, but who was also always there with advice and the occasional Südkreuz delivery when needed.

To the MDC PhD graduate program, and to Benjamin Judkewitz, Stephan Preibisch and Raluca Niesner for the annual review of my project and the valuable outside perspective to keep it on track.

To the Medical Physics group at MLU Halle. Especially to Ulrike, for keeping up the good spirit when nothing seemed to work and for providing me shelter (and porridge!) every now and then. Thanks to Werner, for knowing everything, for having such an uplifting personality and for taking on the Raman project together with Albrecht. My gratitude of course also goes to the extended members of the Halle group, Claus, Silvio and Jens, for the good collaboration, great time in San Francisco and best evenings in Berlin.

To my collaborators at UCL, Thomas Allen and Edward Zhang, without whom much of this work would not have been accomplished.

To André and Wolfgang, for the constant support in- and outside of the lab. I wish I could list all the little situations and endless meetings we shared. Instead, I have to leave it at this: That day in Warnitz and night at SO36 are still some of my most cherished Berlin memories.

B. ACKNOWLEDGEMENTS

To Irene (who we dearly missed during said events!), for managing the lab like nobody else could, for giving it her all with the retinas, and for always having an open ear.

To Russ, for making the lab more of a place I like to come to (no sarcasm here, whether you want to hear it or not), for his incredible general knowledge (ask him anything about biology or at pub quiz) and for immensely helpful writing feedback (that's all I have to say but I like to overuse parentheses and, for the purpose of breaking the reading flow, commas).

To Alex, for the emotional support and discussions about many things concerning work and private life. I am so grateful you let me be vulnerable and were there to listen, give advice and reflect if needed.

To Katja and Eireen, who are the heart and soul of the lab with Irene, have ridiculous talent at the bench and brighten each day with a smile.

To Anna, Elena, Veronique, Silvanus, Baptiste and Tanja. Thank you for being such an inspiring and fun bunch of people! I especially thank Anna for giving me confidence in myself and my work - much more than she realizes, I think.

To Guido and Julia (plus Matthias of course) for all things Harry Potter, DPG conferences, Bubble Tea Tuesdays, draft feedback and so much more! I am very lucky to have colleagues that became friends like you.

To everyone at iVBL, past and present. Thank you for letting me be a part of this group of wonderful people. You guys have enriched my life in ways that I will certainly only fully understand once I don't have you around all the time anymore. I am ending this life chapter with many unforgettable moments and friendships which I am immensely grateful for.

To the most supportive friends you could ask for, in particular:

To Britta, my writing partner in crime. For the shared frustration, sadness and joy. For the cursing and the dancing and the laughing. I cannot begin to express what it meant to live through this final stretch with you. And I cannot wait for all those Acroyoga sessions as doctors to come (imagine cartwheel emoji here)!

To Tabea S and Benny. Thank you for always making me feel at home, for feeding me back in lockdown no. 1 (and actually never stopping to do so), for at least a million other things, and for simply being such great friends. Those home office sessions and balcony breakfasts were absolutely vital to keep me sane enough to make it to the finish line.

To Tabea K, for finishing the journey before us, cheering us on and telling us where to look out for obstacles (and how important massages are). And of course for date banana bread, slimy talks and Tequila happiness.

To Ruby, for being there and understanding completely when I was lost. And for taking me to Mexico and inviting me to become part of your family at just the right time, so I could slowly find back to being myself.

To Ash, for being there from literally day one and staying for the long haul. Your kindness, sincerity and honesty have amazed me ever since we met in that hotel room during interview week.

To Sigga, Esther, Eleonore, Niels and Michael, for a magical time and some of the silliest dances in Herräng that came exactly when I needed energy for the final push.

To Konsti, for being the rock when it was necessary and for being able to let go when it was necessary, too.

To my sister Bente. Especially because, apparently, she wasn't properly acknowledged in my Master's thesis. So, slightly belated, here goes all the credit she deserves. Thank you for being such an amazing human being.

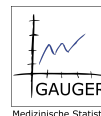
To Fabi, for making the last months of this journey infinitely more amazing through more things than I could ever list on this mundane piece of paper. All of them were definitely worth more than the extra month or two it took to write this thesis because, well, you are the best.

Zu guter (und bester) Letzt geht der Dank an meine Familie. Insbesondere Mutti, Papa, Oma und alle, die jetzt nicht mehr dabei sein können. Nur durch euch und eure bedingungslose Unterstützung bin ich heute da, wo ich bin und die, die ich bin. Das haben wir doch eigentlich ganz gut hinbekommen :)

Curriculum Vitae

Mein Lebenslauf wird aus datenschutzrechtlichen Gründen in der elektronischen Version meiner Arbeit nicht veröffentlicht.

Statistics Certificate



Dr. Ulrich Gauger
Pappelallee 72 • 10437 Berlin
Fon 030/4459882 • Mobil 0160/97936812
ulrich.gauger@gmail.com

Dr. Ulrich Gauger • Pappelallee 72 • 10437 Berlin

statistikhilfe.de
medizin-statistik.de

02. Juni 2023

Bestätigung für Elisabeth Baumann, geb. am [REDACTED]

Hiermit bescheinige ich, dass Frau Elisabeth Baumann bei mir eine statistische Beratung zu ihrem Promotionsvorhaben:

Connecting Endothelial and Hemodynamics – Method Development for Preclinical Optical Imaging of the Vasculature

zu folgenden Terminen wahrgenommen hat:

Termin 1: 19. Mai 2023

Mir erscheinen die verwendeten statistischen Methoden der Problemstellung angepasst.

Berlin, den 02. Juni 2023



Dr. Ulrich Gauger,
akkreditierter Statistiker am Promotionsbüro der Charité Berlin.